PU-AAC-2016-MC-0001

OCEANUS MISSION CONCEPT STUDY

MISSION TO EXPLORE SATURN AND URANUS

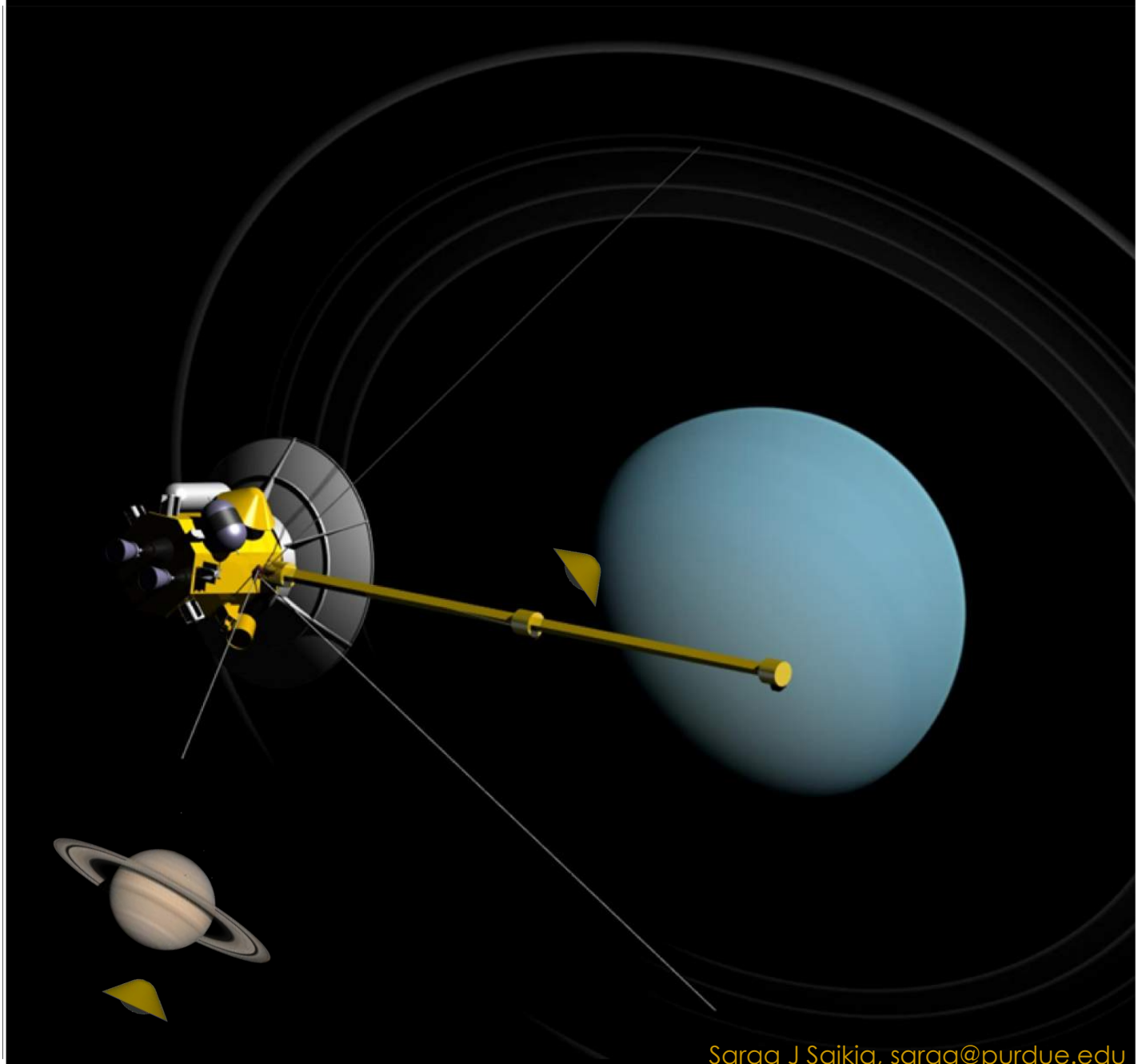

Sarag J Saikia, sarag@purdue.edu

May-June 2016

Purdue University
School of Aeronautics and Astronautics
West Lafayette, IN 47901

PURDUE UNIVERSITY

This page intentionally left blank.

Study Participants

Dr. Sarag Saikia
Study Lead and Facilitator

Justin Mansell, *Principal Investigator*

Nithin Kolencherry, *Project Manager*

Kyle Hughes, *Mission Architect*

Jacob Elliott, *Science Lead*

Alec Mudek, *Mission Design Lead*

James Millane, *Mission Design*

Archit Arora, *Mission Design*

Gregory Smith, *Mission Design, Propulsion*

Paul Witsberger, *Mission Design, ACS*

Jennifer Pouplin, *Telecom, CDH, Science*

Kody Coleman, *Telecom, CDH, Science*

Luis P. Podesta, *Lead Systems Engineer*

Stephen Fulton, *Systems Engineer*

Ye Lu, *Systems Engineer, EDL*

Takaya Ukai, *Systems Engineer, Cost*

Benjamin Libben, *EDL, Structures*

Eiji Shibata, *EDL, Thermal*

Ben Tackett, *EDL, Structures, Risk*

Ho Soon Chye, *Power, ACS, Propulsion*

Nicholas Hobar, *Science, Thermal*

Foreword

An experimental graduate design course, "Conceptual Space Mission Design" was offered at Purdue University in May–June 2016 as a *two weeks'* intensive team exercise, where students performed a rapid conceptual planetary science mission design. The exercise was inspired by NASA's Planetary Science Summer School run by the Jet Propulsion Laboratory every summer. Students participated in a series of "intensive" concurrent design sessions in an "active learning" environment, where the mission design and instrument suite were finalized. Students thereby learnt the interconnectedness of mission elements, performed the necessary trade-offs to stay within the cost cap. The students developed all the necessary tools to conduct the mission concept study.

In August 2015 at the NASA Outer Planets Assessment Meeting, Dr. James Green, the Director of the Planetary Science Division of NASA's Science Mission Directorate announced the plan to conduct NASA's Ice Giants Mission Studies. JPL is currently leading the Ice Giant Mission Studies work. In support of the NASA's plan, the students were inspired to conduct an early mission concept study to explore the ice giant planets within the cost cap of NASA's Flagship missions.

In May 2015, a unique Saturn-Uranus trajectory option was discovered at Purdue University which enables exceptional multi-spacecraft-multi-probe mission opportunities. The work was as a result of collaborative work between Purdue University and NASA Ames Research Center. The students in the course used the exclusive Saturn-Uranus trajectory—first presented at the August 2015 NASA Outer Planets Assessment Group Meeting—to develop the mission concept. Such a mission concept opportunity enables delivery of an atmospheric probe into Saturn's atmosphere for the first time, at the same time, deliver a second entry probe and an orbiter at Uranus. The result of the study is "OCEANUS: A Mission Concept to Explore Saturn and Uranus."

The mission concept study was presented to a panel of scientists and engineering at NASA Jet Propulsion Lab, NASA Centers, and Industry. The feedback provided by the panel were very helpful in the preparation of the final report. I thank our colleagues at JPL: Charles Budney, James Cutts, Kim Reh, Young Lee, John Elliott, Anastassios Petropoulos, Nitin Arora, and Jon Sims for valuable insight and support during the study. Finally, I will be glad if the OCEANUS study provides some insight in the design of mission concepts to explore the ice giant planets as well as in the design of multi-spacecraft-multi-planet missions.

As a reader, should you find any error, please notify me at sarag@purdue and jmansell@purdue.edu.

Dr. Sarag J Saikia
School of Aeronautics and Astronautics, Purdue University
West Lafayette, Indiana
August 16, 2016

Acknowledgments

The work of this study was enhanced by the generous advice of numerous researchers, colleagues, and students both within and beyond Purdue University. The science team wishes to thank Briony Horgan and David Minton at Purdue University as well as Andrew Howarth at the University of Calgary, Canada, for their helpful comments regarding remote sensing and science operations. Also at Purdue University, the study team thanks James Longuski whose expertise guided and inspired the work of this study. At the Jet Propulsion Laboratory, the authors would like to thank Kim Reh, John Elliot, Jon Sims, Young Lee, Anastassios Petropoulos, James Cutts, Robert Shishko, Humphrey Price, and Charles Budney for their comments, advice, and inspiration for this study. At Aerojet Rocketdyne the authors gratefully acknowledge the expertise of Joe Cassady whose generous advice aided the trajectory design of the study. Finally, the team wishes to thank all those whose names may have been missed as well as the interested and insightful audience who attended the presentations of our work.

Table of Contents

List of Tables

Selected List of Figures

Acronyms and Abbreviations

ΔV	Delta-velocity
ACS	Attitude Control System
ASP	Atmospheric Structure Package
AU	Astronomical Unit
BWG	Beam Waveguide
C&DH	Command and Data Handling
CBE	Current Best Estimate
CER	Cost Estimating Relationship
CML	Concept Maturity Level
DCT	Design Control Table
DM	Deflection Maneuver
DOFF	Degrees Off Boresight
DOR	Directional One-Way Ranging
DSN	Deep Space Network
EDL	Entry, Descent, and Landing
EGA	Earth Gravity Assist
EISRP	Equivalent Isotropic Radiated Power
eMMRTG	Enhanced Multi-mission Radioisotope Thermoelectric Generator
EPE	Energetic Particles Experiment
FEM	Finite Element Method
FOV	Field of View
FY	Fiscal Year
GRAM	Global Reference Atmospheric Model
HAD	Helium Abundance Detector
HEEET	Heatshield for Extreme Entry Environment Technology
HEF	High Efficiency
HGA	High Gain Antenna
IMU	Inertial Measurement Unit
LGA	Low Gain Antenna
MAG	Magnetometer
MEV	Maximum Expected Value
MGA	Medium Gain Antenna
MIR	Mid-infrared Radiometer
MLI	Multi-layer Insulation
MMH	Monomethyl Hydrazine
MON-3	Nitrogen Tetroxide
MS	Mass Spectrometer
NAC	Narrow Angle Camera
NEP	Nephelometer
NEXT	NASA Evolutionary Xenon Thruster
NIR	Near-infrared
NNR	Neural Network Regression
NPR	NASA Procedural Requirement
OPI	Outer Planet Imager
OSR	Optical Solar Reflector
PCDU	Power Conditioning and Distribution Unit
PCEC	Project Cost Estimating Capability
PICA	Phenolic Impregnated Carbon Ablators
PWA	Plasma Waves Analyzer
RAAN	Right Ascension of Ascending Node
RCS	Reaction Control System
R_E	Mean Radius of Earth
RF	Radio Frequency
RHU	Radioisotope Heating Unit
RTG	Radioisotope Thermoelectric Generator
R_U	Mean Radius of Uranus
SDRAM	Synchronous Dynamic Random Access Memory
SEP	Solar Electric Propulsion
SFR	Solar Flux Radiometer
SLS	Space Launch System
SNT	System Noise Temperature
SPI	Suprathermal Particle Imager
SRU	Stellar Reference Unit
STM	Science Traceability Matrix
TOF	Time of Flight
TPS	Thermal Protection System
TRL	Technology Readiness Level
TWTA	Travelling Wave Tube Amplifier
UHF	Ultra High Frequency
UOI	Uranus Orbit Insertion
USO	Ultra Stable Oscillator
UV	Ultra Violet
UVS	Ultra Violet Spectrograph
VNIS	Visible and Near-infrared Imaging Spectrometer
WAC	Wide Angle Camera
WBS	Work Breakdown Structure

Executive Summary

The ice giants, Uranus and Neptune, represent a distinct type of planet that may be common beyond our own Solar System (Guillot and Gautier, 2007; Morton et al., 2016). Within the Solar System, they are distinguished from their gas giant cousins, Jupiter and Saturn, mainly by their composition, size, and distance from the Sun. These factors hold many implications regarding their origin and evolution. Indeed, understanding the structures and processes that characterize the ice giants provides an important window into the conditions of the early Solar System that can help refine our understanding of planetary formation as a whole.

Despite tremendous scientific value, exploration of Uranus and Neptune by spacecraft has been limited to the *Voyager 2* flybys in 1986 and 1989, respectively. Mission concepts to send a dedicated orbiter to one of these planets are complicated by large flight times and small delivered payloads. Missions since *Voyager* have therefore opted to explore more accessible targets in the Solar System. However, development of a suite of new technologies, including aerocapture and the Space Launch System (SLS), may enable a highly capable orbiter and one or more atmospheric probes to be delivered to one of the ice giants within a reasonable time frame.

Given their strong scientific interest and the advent of these new technologies, the 2013-2022 *Visions and Voyages* Planetary Science Decadal Survey lists ice giant exploration as a top priority (National Research Council, 2011). In addition, the survey also advocates for continued exploration of the gas giants, with many objectives focused around *in situ* studies of Saturn's atmosphere.

The purpose of this study was to investigate the key trades and develop a preferred design point for a Uranus orbiter and atmospheric probe with the potential for an additional atmospheric probe delivered to Saturn. Uranus was selected over Neptune due to lower flight times, larger delivered mass, broader scientific interest, as well as the opportunity for a Saturn-Uranus trajectory. The mission is intended to fit within the cost constraints of NASA's Flagship program (<$2B FY15$) and launch between the years 2023 and 2037. Both the SLS Block 1B and the Atlas V551 launch vehicles were considered. Low-thrust trajectories using solar electric propulsion (SEP) and aerocapture strategies at Uranus were also investigated. In general, the requirements were kept consistent with NASA's ongoing ice giant mission studies led by the Jet Propulsion Laboratory.

The preferred design has been dubbed OCEANUS, short for Observatory Capture Exploring the Atmospheric Nature of Uranus and Saturn, and also named in honor of the eldest son of the Greek gods Gaia and Ouranos. The conceptual spacecraft is launched on a Saturn-Uranus trajectory in July of 2028 using the SLS Block 1B. The trajectory provides a gravity assist at Saturn in January of 2032, prior to which an atmospheric probe is deployed on an entry trajectory. A similar probe is also deployed on an entry trajectory at Uranus prior to orbit insertion by chemical rockets in early 2040.

OCEANUS' nominal mission then includes a 2-year science tour of Uranus and its satellites with opportunities for an extended mission. The orbiter includes an array of nine remote sensing and *in situ* instruments. Electric power is provided by 5 enhanced radioisotope thermoelectric generators (eMMRTG) and a 4-meter diameter fixed high-gain antenna (HGA) is the primary means of telecommunication with the Deep Space Network (DSN). The overall cost of the mission without launch costs is estimated to be $1.92 billion in 2015 US dollars. A rendering of the spacecraft configuration is shown below.

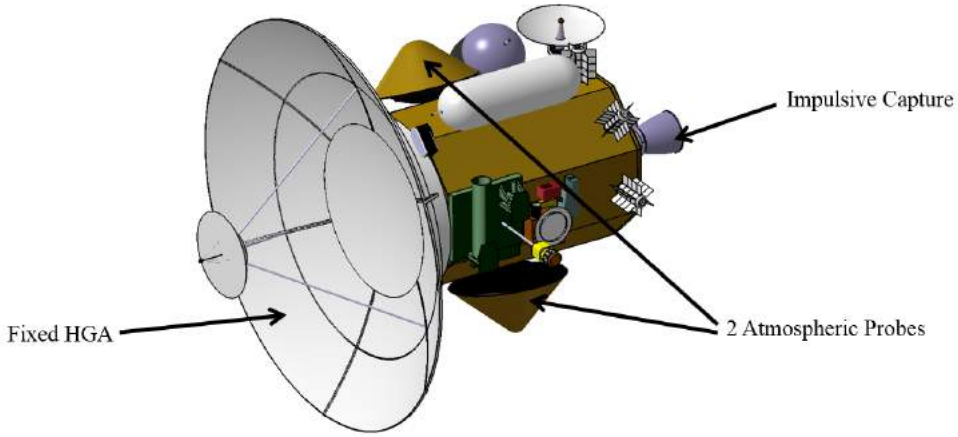

Configuration of the OCEANUS spacecraft.

The OCEANUS concept provides a robust platform for achieving a broad range of high-priority science objectives at both Saturn and Uranus and fits within the constraints of a typical Flagship class mission. The strategy of an impulsive capture at Uranus was found to be superior to aerocapture and the large ΔV provided by the SLS made low-thrust SEP trajectories unnecessary. Thus, the mission can be completed with minimal development of new technologies. Should cost overruns or schedule slips still threaten the mission, the combination of two atmospheric probes and overlapping instrument objectives provides a straightforward means of descoping low-priority instruments.

Section 1 presents a literature survey that outlines the specific scientific investigations that are of interest to outer planets research. Section 2 provides an overview of the OCEANUS mission as well as the major trade studies involved in the concept generation. Sections 3-5 discuss the technical details of OCEANUS, including instruments, subsystems, trajectory, and communications. Additional technical details regarding systems and trade analyses are relegated to the appendices. Finally, Sections 6 and 7 provide the risk and cost analyses of OCEANUS.

1 Outer Planets Science

1.1 Ice Giant Exploration

The ice giants, Uranus and Neptune, are so named due to their relatively high abundance of heavy elements that would have condensed into ices during the early formation of the Solar System. Their composition distinguishes them from the gas giants, Jupiter and Saturn. While Jupiter and Saturn are more than 90% hydrogen and helium by mass, their abundance in the ice giants is less than 20% (Guillot and Gautier, 2007). This difference in bulk composition when compared to the gas giants is thought to reflect the different environment in which the ice giants formed. For instance, the enriched C/H ratio but apparently depleted N/H ratio of Uranus and Neptune suggests that these planets formed at location in the protoplanetary nebula where CO but not N_2 had condensed into ice (Ali-Dib et al., 2014). Constraining the bulk composition and isotopic ratios of giant planets therefore provides insight into the conditions and variability of the early Solar System.

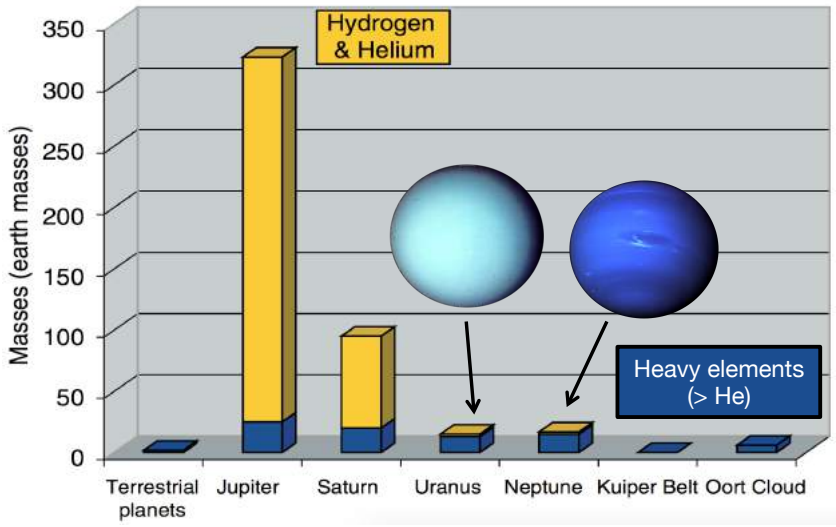

Figure 1.1: Bulk composition of celestial bodies in the Solar System (adapted from Guillot and Gautier, 2007). Of the four giant planets, two distinct categories arise. Jupiter and Saturn are composed mainly of hydrogen and helium, while Uranus and Neptune possesses a relatively low abundance of these elements.

The ice giants are also distinct from the gas giants in ways beyond their composition. Different atmospheric constituents not only reflect different bulk composition, but the influence of different condensation, chemistry, and transport processes (Atreya, 1986). For instance, the low abundance of hydrogen on the ice giants means that it is constrained to a thin outer envelope rather than transitioning to a mantle of metallic hydrogen below mega-bar pressures as it does on Jupiter and Saturn. The inferred density profiles of Uranus and Neptune indicate that their interiors are instead

dominated by an ionic fluid of uncertain composition (Guillot, 2005). This finding holds major implications for the origin of ice giant magnetic fields and their internal heat flux. Whereas the magnetic fields of Jupiter and Saturn are essentially dipolar and aligned with the rotation axes, the magnetic fields of Uranus and Neptune are much more complex, having strong quadrupole moments and both being significantly tilted and offset (Russell and Dougherty, 2010).

Even among the Solar System's ice giants there are differences, particularly when their internal heat flux is considered. Similar to Jupiter and Saturn, Neptune emits significantly more power than it receives from the Sun. Uranus, on the other hand, produces very little of its own heat, a matter that may be indicative of inhomogeneities in its interior that inhibit convection (Guillot and Gautier, 2007). Uranus also has the striking property of rotating about an axis that is inclined by nearly 98 degrees to its orbital plane. The role that this plays in atmospheric circulation and magnetic reconfiguration is poorly understood and the planet's extreme seasonal forcing provides a crucial test to our understanding of planetary atmospheres and magnetospheres.

Given their unique compositions, structures, and processes, the ice giants clearly represent a distinct type of planet. However, interest in the ice giants is more general than simply understanding our own Solar System. Figure 1.2 presents the sizes of confirmed extrasolar planets as of May 2016 (Morton et al., 2016). The data shows that a large proportion of planets fall within the size range of Uranus and Neptune, meaning that ice giants may be surprisingly common around other stars. A detailed study of Uranus and Neptune may therefore allow these planets to serve as ground truth for understanding the conditions present on extrasolar ice giants.

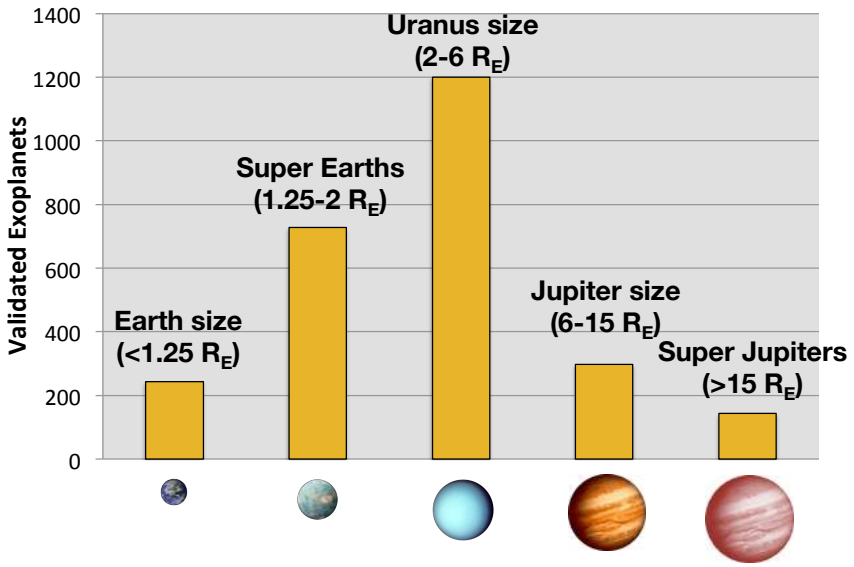

Figure 1.2: Size categories of confirmed extrasolar planets to date. Planets in the size range of Uranus and Neptune make up the most populous category, meaning that ice giants may be a common type of planet. Data from Morton et al., 2016.

The uniqueness of the ice giants in the Solar System and their implications to understanding extrasolar planets has made ice giant exploration a top priority in the current Planetary Science Decadal Survey (National Research Council, 2011). The gap that they represent in our knowledge of the Solar System is recognized internationally as well (Arridge et al., 2014; Masters et al., 2014). To date, studies of the ice giants have been limited to ground and space-based telescopes in addition to the brief *Voyager 2* flybys of Uranus and Neptune in 1986 and 1989, respectively. A New Frontiers or Flagship-class mission to one of the ice giants could dramatically enhance our understanding of these planets by providing a means to study the interior, atmosphere, magnetosphere, rings, and satellites at unprecedented resolution and obtain measurements that are otherwise inaccessible from Earth. Such observations could be expected to yield new insights into the formation of the Solar System and the role that giant planets play in creating a habitable environment for Earth and potentially other Earth-like planets.

1.2 Uranus Science

Of the two ice giants in our Solar System, Uranus is more practical to visit and the most challenging to our understanding of giant planet formation and evolution (Arridge et al., 2014). It was therefore selected to be the primary body of study for this mission concept. The planetary science decadal survey recommends a hierarchy of scientific objectives for the ice giants that can be organized into 4 major themes: Atmosphere, Magnetosphere, Interior, and Satellites (National Research Council, 2011). Much work has been accomplished by NASA's Ice Giants Science Definition Team to define and prioritize specific investigations in each of these areas, including the creation of a draft science traceability matrix (Ice Giants Science Definition Team, 2016). Based on their work, as well as the white papers of other authors, the following sections outline the major questions and investigations that the OCEANUS concept seeks to address.

1.2.1 Atmosphere

Understanding the composition and dynamics of Uranus' atmosphere is of fundamental importance to constraining models of planetary formation and evolution. Microwave spectra and the radio occultations by the *Voyager 2* spacecraft indicate that the uppermost cloud decks are composed of methane ice with underlying clouds of H_2S, NH_4SH, and eventually H_2O (Lindal et al., 1987; de Pater et al., 1989; de Pater et al., 1991). Of these layers, methane is the best understood since it condenses in the high, well-observed portion of the atmosphere around 1.2 bar (Lunine, 1993). Below the methane cloud decks, atmospheric composition and abundances are poorly constrained. Penetration of an atmospheric entry probe to depths ~10 bar would enable the measurement of bulk CH_4 and H_2S abundances, as well as the abundances of noble gases and key isotopic ratios needed to constrain models of ice giant formation (National Research Council, 2011). *In situ* measurements of the upward and downward radiometric flux from an entry probe would also refine our understanding of Uranus' internal heat as well as reveal the location and thickness of cloud layers.

The *Voyager 2* radio and UV occultations also provided information about the vertical temperature profile of Uranus' atmosphere, showing the thermosphere to reach temperatures upwards of 850 K. Such a high temperature cannot be explained by solar heating alone but may result from inefficient cooling by hydrocarbons (Trafton et al., 1999) or heating from currents in the ionosphere (Arridge et al., 2014). Figure 1.3 summarizes the vertical thermal structure and cloud layers of the Uranian atmosphere based on the NASA Ames model (Agrawal et al., 2014) derived from the *Voyager 2* occultation and subsequent re-analysis by Sromovsky et al. (2011).

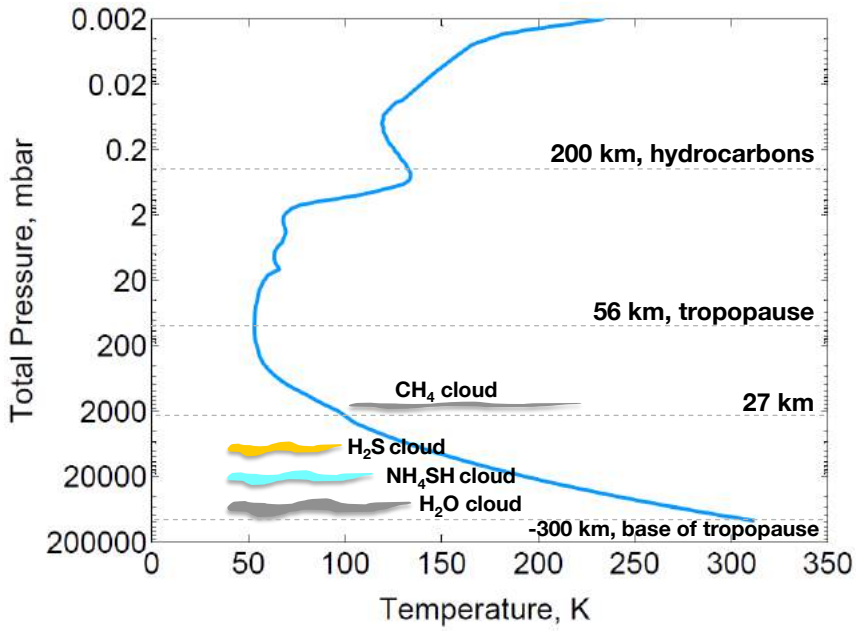

Figure 1.3: Vertical temperature and composition profile of the Uranian atmosphere based on the NASA Ames engineering model (Agrawal et al., 2014). Low solar irradiance and negligible internal heat create a troposphere cold enough to see the condensation of methane and H_2S ices. Oscillations in the stratospheric temperature are attributed to local radiative heating from hydrocarbon hazes.

Oscillations in the stratospheric temperature between pressures of 20 and 0.2 mbar are attributed to the presence of hydrocarbon hazes that contribute localized radiative heating. The presence of these hazes may also play a role in cloud formation, as it has been suggested that condensed hydrocarbons may sediment down into the troposphere and serve as cloud condensation nuclei (Arridge et al., 2014). The distribution of stratospheric hazes could therefore explain why clouds form predominantly at certain latitudes. However, the role and distribution of these hazes remains poorly constrained.

Unraveling the mystery of Uranus' hot thermosphere and understanding the role of hydrocarbon hazes is best accomplished with UV, visible, and infrared orbital imaging. Limb-sounding in the mid-infrared at wavelengths of 7.7 μm and longer provide opportunities to sense the vertical temperature profile from ~1 nbar to ~2 bars

atmospheric pressure (Orton et al., 2014). Also contained in this range are the rotational spectra of a number of photolysis hydrocarbon products that may serve as an important remote sensing tool for observing the conditions and variability of the upper atmosphere (Burgdorf et al., 2006). Complimentary imaging at UV wavelengths could further constrain the properties of aerosols and hydrocarbon hazes. Airglow and auroral imaging at various wavelengths can also provide insight into the chemistry of the upper atmosphere as well as the effects of magnetosphere-ionosphere-atmospheric coupling.

Though Uranus' atmosphere appears essentially featureless when compared to the other giant planets of the Solar System, observations at infrared wavelengths reveal circulation patterns, wave structures, and methane depletion at the poles (Lunine et al., 1993; Sromovsky et al., 2014; Sromovsky et al., 2015). Derivation of the zonal wind profile reveals the presence of a broad retrograde equatorial jet (Lunine, 1993) and both bright and dark spots have been observed to appear and evolve on the order of months and years (Hammel et al., 2009; Sromovsky et al., 2012). The core implication of these observations is that Uranus' atmosphere is much more dynamic than once thought, and one of the principal mechanisms is believed to be forcing from Uranus' extreme seasons (Arridge et al., 2014).

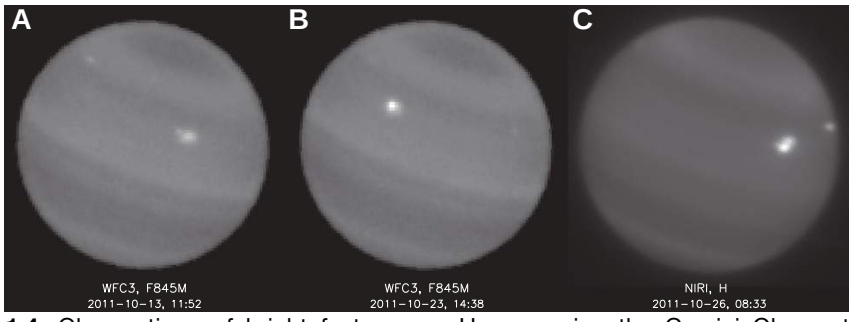

Figure 1.4: Observations of bright features on Uranus using the Gemini Observatory near-infrared camera in 2011 show variable brightness and drift rates (Sromovsky et al., 2012). The features may be the result of clouds associated with vortex circulations.

Characterizing Uranus' global wind patterns and variability in composition would allow for a better understanding of the energy sources and transport mechanisms that govern the dynamics of giant planet atmospheres. Wind profiles can be inferred from high-resolution imaging at visible and infrared wavelengths to track the drift of cloud structures and chemical tracers. Continued observation of cloud morphology over time scales of hours, days, and months can provide insights into storm formation and dissipation. Spectral and broadband IR imaging can reveal the temperature field of the troposphere and the circulation of the upper atmosphere. Complimentary imaging of the visible albedo at a range of solar phase and incidence angles can help constrain the energy balance of the atmosphere (Hofstadter et al., 2010). Comparisons to the *Voyager 2* flyby and ground-based observations would characterize the role of seasonal forcing. Finally, extending knowledge of the vertical temperature, composition, and wind profile below 2 bar could be accomplished *in situ* using an atmospheric entry probe.

1.2.2 Magnetosphere

Little was known about the characteristics of the Uranus magnetosphere prior to the *Voyager 2* encounter in January 1986. The flyby revealed that the magnetic field was highly tilted (59°) and offset (~1/3 R_U) relative to the planet's axis of rotation. This unusual geometry is depicted in Figure 1.5. Measurements from the flyby constrained the location of the magnetopause to a distance of 18 R_U along the planet-Sun line and showed a roughly cylindrical magnetotail becoming twisted into a helical corkscrew by Uranus' 17.2h rotation (Ness et al., 1986). Unfortunately, the limited geometry and large distance of the *Voyager 2* encounter has allowed for only a crude estimation of the magnetic field and current models remain severely under constrained (Russell and Dougherty, 2010).

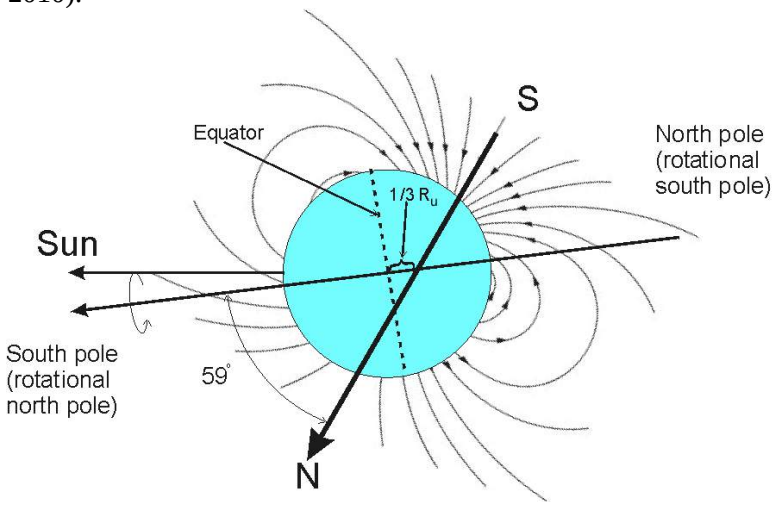

Figure 1.5: Geometry of the highly tilted and asymmetrical Uranian magnetic field. Though the Voyager 2 flyby provided a qualitative picture of the magnetic field configuration, the limited geometry of the flyby has left more precise models poorly constrained.

Voyager's ultraviolet spectrometer (UVS) instrument also detected the presence of weak hydrogen aurorae and airglow on the planet (Broadfoot et al., 1986). These emissions can provide additional high-latitude constraints on the magnetic field and continued analysis of the *Voyager 2* dataset has suggested that auroral precipitation results from the excitation of magnetotail-side plasma by strong whistler-mode radio waves (Floyd, 2009). A major source of this plasma may be the extended hydrogen corona discovered using the stellar occultations observed by the *Voyager 2* UVS instrument (Broadfoot et al., 1986; Bridge et al., 1986). However, the near-alignment of Uranus' rotation axis with the direction of the solar wind during the *Voyager 2* flyby also resulted in the efficient radial convection of plasma that transported solar wind particles deep into the magnetosphere (Bridge et al., 1986). Since this particular alignment only holds near the solstices, many questions arise about the stability and evolution of Uranus' radiation belts throughout its orbit.

Further *in situ* particle and field measurements are critical to answering questions about the sources, characteristics, and dynamics of Uranus' magnetospheric plasma. The

unique geometry of Uranus' magnetic field also provides a new laboratory to test our understanding of otherwise known transport and energization processes. Comparisons to observations conducted during the *Voyager 2* flyby will be aided by the fact that spacecraft launched in the late 2020s will reach Uranus between its 2028 northern summer solstice and its 2049 southern spring equinox. The effect of equinox geometry on Uranus' magnetospheric configuration and stability is entirely unknown (Rymer et al., 2010).

Simple mapping of the magnetic field by an orbiter using a magnetometer comparable to the MAG instrument on *Cassini* could constrain the high-order moments of the magnetic field. Continued observation would also allow us to better understand how the field reconfigures over the diurnal cycle and investigate its evolution on the order of months and years. Imaging of auroral morphology at ultraviolet, visible, and near-infrared wavelengths provides a further means of constraining the magnetic field as well as exploring its interaction with the solar wind (Lamy et al., 2012). This can provide insights into the processes involved in energetic particle trapping, including the various energization mechanisms such as wave-particle interactions and moon sweeping (Rymer et al., 2010). Complimentary measurements of ions, electrons, and electric fields over a wide dynamic range would help characterize the structure, stability, and dynamics of Uranus' radiation environment (Arridge et al., 2014). Lastly, spectral and broadband airglow imaging can explore the effects of magnetosphere-ionosphere-atmospheric coupling.

1.2.3 Interior Structure

Constraining the interior structure of ice giants holds important implications for our overall understanding of Solar System and planetary formation. For example, constraining the mass and composition of Uranus' rocky core could help distinguish between two major formation models. Namely, if a primordial rocky core formed first and subsequently accreted gas or whether it formed directly from instabilities in the protoplanetary disk (Guillot, 2005; Arridge et al., 2016). Though it is generally believed that the ice giants formed near their present locations, the theory that they formed closer to the sun and migrated outwards provides an appealing explanation for their present orbits (Tsiganis et al., 2005). Regardless, investigating the characteristics of the Uranian interior can provide a window through which to study the composition and thermochemistry of the solar nebula during the early stages of planetary formation. Relevant insights could inform the search for extrasolar planets and reveal the role that giant planets play in creating a habitable inner solar system through processes such as large impacts (National Research Council, 2011).

Much of what is known about the interiors of giant planets comes from our understanding of high-pressure physics. Unfortunately, the pressure and temperature regimes of giant planet interiors are such that accurate equations of state are extremely difficult to obtain. The complex composition of the ice giants also prevents convenient simplifications, such as the assumption of a dominantly hydrogen interior that is appropriate for studying Jupiter or Saturn (Guillot, 2005). Nonetheless, current models of

Uranus' interior predict a rocky core with an overlying mantle of ices and an envelope of hydrogen, helium, and ices (Guillot and Gautier, 2010). Figure 1.6 illustrates this structure. Icy material in the mantle is thought to consist primarily of ionic water, which may transition to superionic water after a layer of diamond or helium sedimentation (Arridge et al., 2014). These models are informed almost chiefly by composition, density, and magnetic field data collected during the *Voyager 2* flyby in 1986. Yet, the limited nature of the data set has left these models under-constrained.

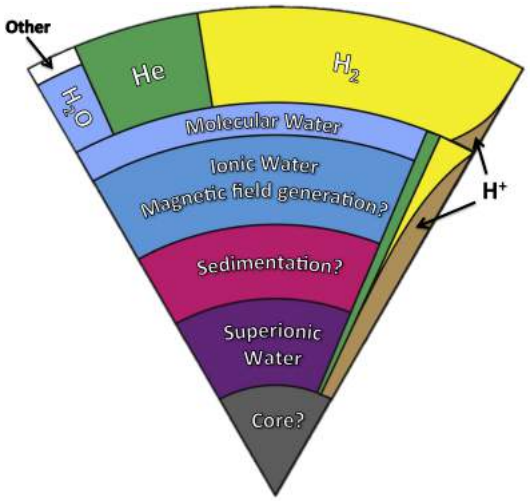

Figure 1.6: Theoretical model of Uranus' interior (adapted from Arridge et al., 2014). An envelope of mostly hydrogen and helium surrounds a mantle of mainly ionic and superionic water.

Two aspects of Uranus' interior in particular have proved difficult to reconcile. The large offset of Uranus' magnetic field suggests that the dynamo region lies relatively close to the surface. The most probable origin is a relatively thin layer of convecting ionic water or metallic hydrogen that lies at a radius of 0.6-0.7 R_U (Stanley and Bloxham, 2006). However, this is at odds with the measured gravitational moments and the anomalously low self-luminosity of Uranus, which both seem to suggest a heterogeneous interior that would largely inhibit convection (Guillot, 2005). One possibility is that convective motions in the interior are decoupled from the rotation of the planet, allowing the dynamo to wander between locally convective regions as fluctuations in composition and thermal gradients permit (Nellis, 2015). Another explanation is that Uranus' interior is convective but suffered an early loss of heat, perhaps from a catastrophic collision that may have also created the planet's extreme axial tilt (Arridge et al., 2014). Ultimately, constraining the structure and evolution of Uranus' interior will require new data that goes beyond the capabilities afforded by *Voyager 2*.

Measurements needed to infer the characteristics of Uranus' interior largely overlap with those of other investigations. For instance, orbital mapping of the magnetic field can be used to assess the structure of the dynamo region. Elemental abundances and temperature profiles measured by a >5 bar entry probe could improve the constraints on interior models and yield insights into processes such as of core erosion. Complimentary measurements from orbit of the bond albedo could shed light on the mystery of Uranus' low internal heat flux. Detailed mapping of surface winds and measurements of oblateness using radio occultations could also provide insight into the rotation of the planetary interior. Lastly, Doppler tracking of the orbiter to radii ~1.5 R_U as well as long-term observations of Uranus' rings could refine the J_2 and J_4 gravitational terms to study the rotation, densities, and mass distributions of the interior (Hubbard et al., 2010).

1.2.4 Satellites and Rings

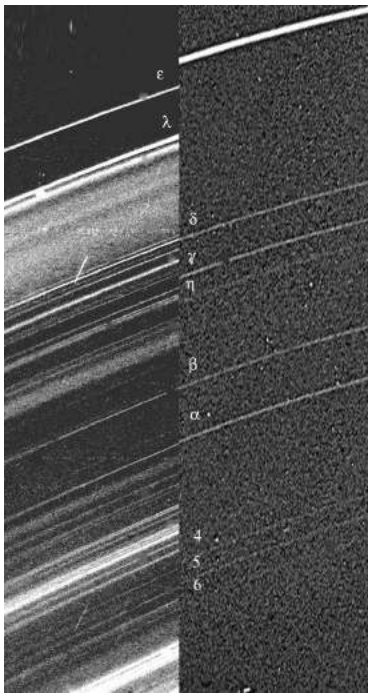

Figure 1.7: Images of forward (left) and back-scattered (right) light from Uranus' rings taken by Voyager 2 show a collection of narrow dense rings interspersed with dusty rings.

Like the other giant planets of the Solar System, Uranus is accompanied by rings and a rich system of moons that orbit roughly in the plane of the planet's rotation. While not as visually impressive as the rings of Saturn, Uranus' rings are more complex than the diffuse rings of Jupiter and Neptune. They also possess several unique features. In contrast to Saturn's broad, dense rings, the Uranian rings are composed of a series of narrow rings interspersed with a network of dust structures. Figure 1.7 compares images of the rings taken by *Voyager 2* from two different phase angles, showing the combination of narrow and dusty rings. The orbits of these rings are more eccentric than Saturn and the outer-most rings have undergone measurable changes in orbit since the *Voyager* flyby, indicating instabilities in ring-moon coupling (French et al., 1986; de Pater et al., 2007). The mechanisms of such rapid evolution are far from understood, but insights are likely to be applicable to the study of other ring systems such as the proto-planetary disk or rings detected on extrasolar planets (Santos et al., 2015).

The composition of Uranus' rings are likewise poorly known, in part because of the lack of a near-infrared spectrometer on the *Voyager 2* spacecraft. Radio occultations from the flyby indicated that particle sizes in the main rings ranged from 10 cm to 10 m with a surprising lack of cm-sized particles. The low albedo of the rings also suggests that at least the surfaces of ring particles are very different compared to Saturn and must include a non water-ice component (Arridge et al., 2014). Several mechanisms have been proposed for the origin of the rings, including meteoroid bombardment and destruction of moons by tidal forces, (Colwell, 1994; Leinhardt et al., 2012). Characterizing the composition and particle size distributions of Uranus' rings therefore provides a means to constrain competing theories of their formation. Differences in composition and the dust distribution within and between the rings can also provide information about material transport and interactions within the inner ring-moon system.

Uranus' satellites provide a further natural laboratory for studying the origin, composition, and dynamics of the ring-moon system. The Uranian inner moons represent the densest known satellite system, with 13 objects catalogued on orbits between 49,770 km and 97,700 km from the planet's center. Similar to Saturn, these tightly packed inner moons may play an important role in supplying and shepherding the rings (Arridge et al., 2014). The inner ring-moon system also shows instabilities with measurable

perturbations in orbits since the *Voyager 2* flyby. Dynamical simulations suggest that the inner moons are subject to collisions on the order of 10^6 years, providing yet another means of ring formation (Showalter and Lissauer, 2006). Understanding the collisional processes and the role that the inner moons play in maintaining the rings will allow an assessment of the long-term stability of Uranus' ring-moon system. Relevant insights will also aid our understanding of the effects of ring-moon disruption and re-accretion, with important applications to planetary formation models.

In addition to the inner satellites, Uranus is orbited by five large "classical" moons that were known prior to the *Voyager* encounter. These moons are depicted in Figure 1.8. Imaging by *Voyager 2* showed their surfaces to be surprisingly varied, with different albedos (all lower than comparable moons of Saturn), crater densities, and striking geological features such as ridges and grooves (Arridge et al., 2014). The surfaces of these moons may be modified by a number of endogenic processes. For example, ridges and troughs on Miranda may be the result of internal upwelling (Pappalardo et al., 1997) while both Miranda and Ariel exhibit evidence of thick cryovolcanic flows (Kargel, 1995). Exogenic processes such as sputtering or catastrophic impacts followed by re-accretion may also play a role in sculpting the surfaces of the large moons. The moons Miranda, Ariel, Umbriel, and Titania all orbit within the confines of Uranus' magnetosphere, exposing them to radiological weathering that has likely altered their surface compositions (Rymer et al., 2010; Arridge et al., 2014).

Figure 1.8: Comparison of the large classical satellites of Uranus. Imaging by Voyager 2 revealed surprising differences in crater density, albedo, and surface features, including evidence of cyrovolcanism on Miranda and Ariel.

The internal structure and composition of the large moons is also of great interest. Interior models by Hussmann et al. (2006) have revealed the possibility of subsurface oceans on Titania and Oberon. Exploring these possibilities with an orbiter provides a comparison to other icy moons with theorized subsurface oceans such as Europa, Ganymede, and Enceladus. Moreover, understanding the interior structure and composition of Uranus' satellites could provide clues to their origin and test the great collision hypothesis of Uranus' axial tilt. The present orbit of the moons about this tilted axis also provides an opportunity to study the effects of unique insolation patterns that are not found elsewhere in the Solar System.

The lack of a near-infrared instrument on *Voyager 2* has left many unanswered questions regarding the composition of the Uranian satellites and rings as well as their interactions with the magnetosphere and each other. Including such an instrument on an orbiter is therefore a high priority. The surface compositions of major satellites could be determined during flybys using spectral imaging in the range 0.8 μm to 5 μm (Arridge et al., 2014). Spectral mapping with a near-infrared spectrometer combined with high-resolution imagery as well as UV imaging and plasma measurements of tenuous atmospheres could reveal the extent, role, and dynamics of both endogenic and exogenic processes in shaping the surfaces of the moons. Such investigations would also lead to tighter constraints on the bulk composition of the moons and therefore a better understanding of their interior structure and origin. Observations of the magnetic field in the vicinity of large satellites during flybys could also reveal the presence of fluid layers in the interior.

A near-infrared spectrometer would also allow for remote determination of the compositions of the rings both by direct and occultation observations. Complimentary imaging at high-resolution would help unravel the dynamics and stability of both the narrow and dusty rings. This could include searching for periodic structures such as spokes, gravity wakes, and spiral density waves in the rings, as well as imbedded moons. Observations of previously unmapped stratospheric species such as CO, CO_2, and HCN in the near and mid-infrared could provide insights into the interaction of the ring-moon system with Uranus' neutral atmosphere (Arridge et al., 2014). *In situ* characterization of dust grains using an instrument similar to *Cassini*'s Cosmic Dust Analyzer could constrain particle sizes, composition, charge-state, and dynamics of dust. This would enable a better understanding of material transport, distribution, and processes within the ring-moon system. Combined with radio and *in situ* plasma measurements, this would provide a means of understanding the physics of dusty plasmas, including the interactions between the ring-moon system and Uranus' magnetosphere, with obvious applications to models of protoplanetary disks.

1.2.5 Science Traceability Matrix

The science traceability matrix (STM) for a Uranus orbiter and atmospheric probe is presented in Table 1.1. Specific investigations and measurement objectives are grouped into the four themes. The matrix also includes notional instruments to meet each measurement objective. The instruments are described in detail in Section 3. Finally, each measurement objective includes one or more functional requirements that are needed to successfully implement the investigation. Many of the investigations, measurements, and functional requirements in the matrix have been informed by the draft science traceability matrix compiled by the Ice Giants Science Definition Team (2016) for NASA's Ice Giants Studies.

Table 1.1: Science traceability matrix for a Uranus orbiter and entry probe

Goal	Investigation	Measurement Objective	Instruments	Functional Requirements
Determine the atmospheric zonal winds, composition, and structure at high spatial resolution, as well as the temporal evolution of atmospheric dynamics.	Characterize the energy sources, temperature, and density of the upper atmosphere.	Spectral emissions and temperatures of constituent species in UV/visible/IR and their variation with latitude, longitude, and altitude.	UVS, VNIS, MIR, OPI	Limb viewing for stratospheric emissions. Good coverage of all latitudes and longitudes.
		Maps and movies of thermal emission and cloud features at multiple wavelengths to observe the action of atmospheric waves.	OPI, VNIS, MIR	<15 km resolution and minute-by-minute imaging of cloud structures over the course of several hours.
	Characterize variations in zonal and meridonal circulation, including searching for features that may be characteristic of extreme axial tilt.	Zonal and 2D windfields at multiple wavelengths, including IR for thermal winds.	OPI, VNIS, MIR	<100 km resolution and measurements over a variety of time scales.
		Doppler tracking of atmospheric probe horizontal motion during descent to determine vertical wind structure.	USO	Doppler tracking of probe.
		Monitor storm formation and dissipation through high-resolution imaging at multiple visible and IR wavelengths.	OPI	<15 km resolution and minute-by-minute imaging of cloud structures over the course of several hours and months.
	Constrain the bulk composition and characterize how the composition varies with depth.	In-situ sampling of atmospheric constituents.	MS, HAD, NEP	Probe penetration to 10 bar (methane, ammonia, hydrogen sulfide) or 40 bar (ammonium hydrosulfide).
		Nadir observations of spectral features to map cloud deck constituents.	VNIS	Nadir viewing with <100 km resolution.
		Measure depth of cloud layers using in-situ measurements of solar flux during descent.	SFR	Atmospheric probe.

(Continued on the next 2 pages)

Goal	Investigation	Measurement Objective	Instruments	Functional Requirements
Understand the basic structure and processes of Uranus' magnetosphere.	Identify the sources, sinks, transport mechanisms, and energization processes of the unusual magnetosphere and study magnetosphere-ionosphere-atmosphere coupling.	Measure negative ions, thermal plasma energy and composition, magnetic fields, charged dust, plasma waves, energetic particles, auroral/airglow imaging in UV/VIS/IR.	All	Good coverage of all latitudes/longitudes at different altitudes.
	Study the temporal variability of Uranus' magnetosphere over hours, days, and seasons (through comparison with *Voyager* data) to understand how the offset rotating magnetosphere interacts with the solar wind over time.	Global-scale mapping of the magnetic field and continued observation over mission life.	MAG	Good coverage of all latitudes/longitudes at different altitudes.
		Measure ions, currents, B-field, and plasma waves in the vicinity of the magnetopause/sheath.	MAG, SPI, EPE, PWA	Apoapsis >23 Ru on the sun-facing side.
		UV and IR emission, auroral morphology, plasma and plasma waves, ionospheric electron density, and electrostatic discharge.	UVS, VNIS, MIR, OPI, SPI, PWA	Limb, nadir, and slew observations of aurora.
	Use the inner ionosphere/magnetosphere as a laboratory to study the behavior of dusty plasmas and planetary formation processes.	Remote sensing of spokes and periodic structures in faint rings as well as searching for collisions and shepherd moons.	OPI	Orbit near the rings at high solar phase angles.
		In-situ measurements of dust and charged particles within the ring system.	CDE, SPI	Orbit within the inner ring system.
	Explore the interaction of satellites with the magnetosphere and characterize the extent and effects of weathering.	Remote sensing of satellite surfaces at visible and IR wavelengths to determine composition.	OPI, VNIS, MIR	Flyby of one or more satellites.
		In-situ measurements of dust and charged particles in the vicinity of satellites.	CDE, SPI	Flyby of one or more satellites.
Constrain the structure and characteristics of the interior.	Infer the high-order structure and evolution of the Uranus' mantle and interior dynamo.	Imrpove estimates of Uranus' mass and orbital perturbation terms through spacecraft tracking and remote sensing of the rings.	OPI, USO	Tracking of the spacecraft to ~1.5 Ru (J2 and J4 terms) or tracking of the spacecraft to ~1.2 Ru (J6 term). Sub km resolution of the rings.
		Global-scale mapping of the magnetic field and continued observation over mission life.	MAG	Good coverage of all latitudes/longitudes at different altitudes.
	Measure planetary oblateness.	Radio occultations at multiple latitudes.	USO	Occultations at multiple latitudes.
	Explore the balance between internal and external heat and extend knowledge of the temperature profile into the fully convective region of the atmosphere (>300 bar).	Visible observations of bond albedo and IR observations of temperature sensitive molecules at all latitudes and longitudes and over varying time scales.	OPI, VNIS, MIR	Good coverage of all latitudes and longitudes at varying solar phase angles and multiple time scales.
		Radio and IR occultations.	VNIS, MIR	Ground tracking of occultations.
		In-situ measurements of vertical temperature and pressure profiles.	ASP	Atmospheric probe.

Goal	Investigation	Measurement Objective	Instruments	Functional Requirements
Understand the origin, interactions, and evolution of the ring system and satellites.	Study collisional processes and their role in the ring-moon system.	Characterization of crater populations with high-resolution imagery.	OPI	Flyby of one or more satellites with sub-km resolution.
		Constrain particle size and packing density within the rings through imaging as well as UV, IR, and radio occultations.	OPI, UVS, VNIS, USO	Sub km resolution of rings at high phase angles. Multiple ring occultations.
		Search for collisions and ripples in the rings.	OPI	Sub-km resolution imaging at high phase angles.
	Determine the composition, origin, and variability of satellite atmospheres.	In-situ measurements of dust and charged particles in the vicinity of satellites.	CDE, SPI	Flyby of one or more satellites.
		Radio and IR occultations.	VNIS, USO	Occultations of satellites.
		UV/visible/IR spectra of atmospheric constituents. Search for plumes/geysers.	UVS, OPI, VNIS, MIR	Limb viewing during one or more flybys.
	Study the role of exogenic processes in shaping the satellites and rings	Surface composition at visibile and IR wavelengths to analyze surface sputtering.	OPI, VNIS	Nadir observations during flyby of one or more satellites.
		Measure 3D dust distribution, characteristics.	CDE	Eccentric orbit.
		Imaging of periodic structures in dust rings to measure response to solar radiation pressure.	OPI	Sub-km resolution imaging of rings at high and multiple phase angles.
		In-situ measurements of dust and charged particles in the vicinity of satellites.	CDE, SPI	Flyby of one or more satellites.
	Study the role of endogenic processes and infer the subsurface structure of satellites.	Locate fluid layers via conductive properties (induced magnetic fields).	MAG	Flyby of one or more satellites.
		Characterize composition and topography of geologic structures at multiple wavelengths.	UVS, OPI, VNIS, MIR	Flyby of one or more satellites, sub km resolution.
		Analyze orbital perturbations during flybys.	USO	Flyby of one or more satellites.
	Search for undiscovered satellites and rings.	Wide-angle imaging during approach and near apoapsis. Narrow-angle imaging of rings to search for embedded moons.	OPI	Imaging during approach, sub km resolution imaging of rings at multiple phase angles.

1.3 Saturn Science

The ground rules of this concept study required that the mission employ an interplanetary trajectory that utilized a Saturn flyby en-route to Uranus. This rule was chosen in order to investigate the science opportunities afforded by a close encounter with Saturn. Despite extensive study by *Pioneer 11, Cassini-Huygens* and both *Voyager* spacecraft, exploration of Saturn and its ring-moon system remains a key objective in the Planetary Science Decadal Survey (National Research Council, 2011). Of particular interest is an *in situ* study of Saturn's deep atmosphere, since no mission has yet deployed an atmospheric probe at Saturn.

In-situ atmospheric measurements provide a number of quantities that cannot be obtained through remote observations. In the context of Saturn, the most crucial is the helium abundance. Helium is difficult to detect remotely due to its zero dipolar moment and the weakness of its spectral lines. Furthermore, measurements of the helium abundance from spectra generated in the high atmosphere bear little information about deeper levels of the atmosphere. Constraining helium's contribution to Saturn's overall bulk composition not only informs planetary formation models, but its ratio relative to hydrogen also provides a window into the structure and processes of the interior. Estimates from previous missions have placed Saturn's helium mass fraction to a large range between 7-17% with 28% being the protostellar value (Guillot et al., 2009). Explanations for this "missing helium" have long centered on the hypothesis that hydrogen and helium separate at megabar pressures, thereby hiding a disproportionate amount of helium in the interior (Guillot, 2005). Hydrogen-helium de-mixing has also been proposed as a solution for Saturn's high self-luminosity, which under simple models suggests an age of only 2-3 billion years (Püstow et al., 2016).

Better equations of state and tighter constraints on the hydrogen-helium ratio are needed to confirm the existence, location, and implications of hydrogen-helium de-mixing. A helium abundance detector of the kind flown on *Galileo* could provide an accurate estimate of the hydrogen-helium ratio at depths below the clouds. *In-situ* measurements by an atmospheric probe of the other noble gases, isotope abundances, and condensable species would provide further insights into the vertical atmospheric/interior structure and planetary origin. Relevant species such as NH_3, H_2S, and NH_4SH can all be measured using a mass spectrometer with suitable dynamic range from depths less than 10 bar (Guillot, 2009). Cloud depths and the radiation balance of Saturn's atmosphere could be further refined by an upward and downward facing radiometer onboard the probe. Finally, Doppler tracking of the probe during descent could reveal the vertical wind structure at depths below the upper cloud layers, thereby complimenting the extensive mapping of 2D windfields by *Cassini*. Table 1.2 summarizes the investigations, measurements, and instruments for a Saturn entry probe deployed during a flyby while en-route to Uranus.

Table 1.2: Science traceability matrix for a Saturn atmospheric probe.

Investigation	Measurement Objective	Instruments
Characterize atmospheric composition and vertical structure.	Solar flux measurements to locate cloud layers.	SFR
	In-situ sampling of atmospheric species, including helium abundance and aerosols.	MS, HAD, NEP
	Vertical pressure and temperature profiles.	ASP
	Doppler tracking of probe to determine vertical wind structure.	USO
Characterize atmospheric radiation balance.	Vertical pressure and temperature profiles.	ASP
	Measure net solar flux.	SFR

2 High-Level Concept and Selection

2.1 Study Request and Concept Maturity Level

The purpose of this study was to investigate the key trades involved in the exploration of the Solar System's ice giants and identify a preferred design appropriate for NASA's Flagship mission program. The resulting mission concept is presented at concept maturity level (CML) 4 as defined in Table 2.1. The study was also conducted according to the following ground rules:

- The mission shall answer key questions about the ice giants as outlined in the *Visions and Voyages* Planetary Science Decadal Survey.
- The mission shall cost less than $2B (FY15$), not including the launch vehicle and launch service costs.
- The mission shall include a Saturn flyby in order to satisfy Saturn science objectives.
- The mission shall be launched no earlier than the year 2023 and no later than 2037.
- The missions shall use either the SLS Block 1B or Atlas V551 launch vehicles.

Table 2.1: Concept maturity level definitions and attributes

Concept Maturity Level	Definition	Attributes
CML 6	Final Implementation	Requirements trace and schedule to subsystem level, grassroots cost, V&V approach for key areas.
CML 5	Initial Implementation	Detailed science traceability, defined relationships and dependencies: partnering, heritage, technology, key risks and mitigations, system make/buy.
CML 4	Preferred Design Point	Point design to subsystem level mass, power, performance, cost, risk.
CML 3	Trade Space	Architectures and objectives trade space evaluated for cost, risk, performance.
CML 2	Initial Feasibility	Physics works, ballpark mass & cost.
CML 1	Cocktail Napkin	Defined objectives and approaches, basic architecture concept.

2.2 Overview of Preferred Design

OCEANUS consists of a 3-axis stabilized orbiter and two atmospheric entry probes. The system launches on the SLS Block 1B with an additional Star 48B booster. The SLS will launch the OCEANUS orbiter and probes onto an interplanetary trajectory. Shortly after launch, the Star 48B booster will burn to set the final trajectory for the Saturn flyby and final Uranus encounter. After the booster burn the spacecraft will begin a four-month checkout and commissioning phase wherein each subsystem onboard the spacecraft is calibrated and tested. Once this phase is complete the spacecraft will go into a standby mode for the remainder of the cruise to Saturn.

On approach to Saturn, the orbiter will be again checked for correct operation and begin a phase of practice maneuvers to ensure that all control systems are functioning properly. After these maneuvers the orbiter will perform a series of instrument calibration operations up to when the Saturn entry probe is released. The probe would be launched 130 days before its descent. During this travel time the probe will be in a stand-by state to conserve battery power. Shortly after the probe is released the orbiter will perform a deflection maneuver to target a flyby of Saturn and cruise to Uranus. During the probe's 130-day cruise, the orbiter will be tracking it, as well as performing science operations as it approaches Saturn. During the probe's descent into the atmosphere of Saturn, the orbiter receives data via its high gain antenna.

After the probe's descent and data relay back to Earth, the orbiter will continue collecting science data on Saturn. After all the data is collected and returned from Saturn, the orbiter will, return to its stand-by mode and cruise to Uranus to begin the final phase of the mission.

The concept of operations for the approach to Uranus are similar to that of Saturn's. After the probe enters and completes its mission, the orbiter will need to reorient and prepare for its insertion burn. The impulsive burn to enter the 20-day science orbit around Uranus will be observable from Earth. Once the obiter has entered its science orbit, it conducts another systems check before beginning its primary 2-year science mission. The orbiter is anticipated to have several moon flybys during or after its primary mission. After it has completed its mission, the orbiter will have to conduct a de-orbit burn to lower itself into the Uranus Atmosphere, where it will be destroyed for planetary protection.

2.3 Key Trades

The OCEANUS concept is largely built upon the study team's assessment of a number of key architecture trades. Of these trades there were two major areas of focus: the capture method for insertion into Uranus orbit and the interplanetary propulsion system. Other important trades encompassed the nature and destination of the atmospheric probes, communication, and whether to position the science orbit inside or outside of Uranus' rings. The major trades explored in the OCEANUS study are discussed below. Full analyses of system and subsystem level trades are provided in the appendices.

2.3.1 Orbital capture method

Two methods of orbital capture were studied: aerocapture and conventional impulsive capture using liquid rocket engines. Aerocapture is an orbit insertion strategy wherein an incoming spacecraft performs aerodynamic braking in a planetary atmosphere until its orbital energy is reduced such that it is captured into orbit. Aerocapture was assessed at being at a technology readiness level (TRL) 6 and would enhance OCEANUS by providing a faster flight time, and possibly a higher delivered mass. The merits of each system are presented in Figure 2.1, along with a representation of their orbital maneuvers. A detailed analysis of aerocapture is included in Appendix A of this report. Aerocapture systems were assessed as part of the Neptune Aerocapture Systems Study (2006). Ultimately, the high risk and the large uncertainties involved in a Uranus aerocapture led the OCEANUS study team to favor a more traditional impulsive capture.

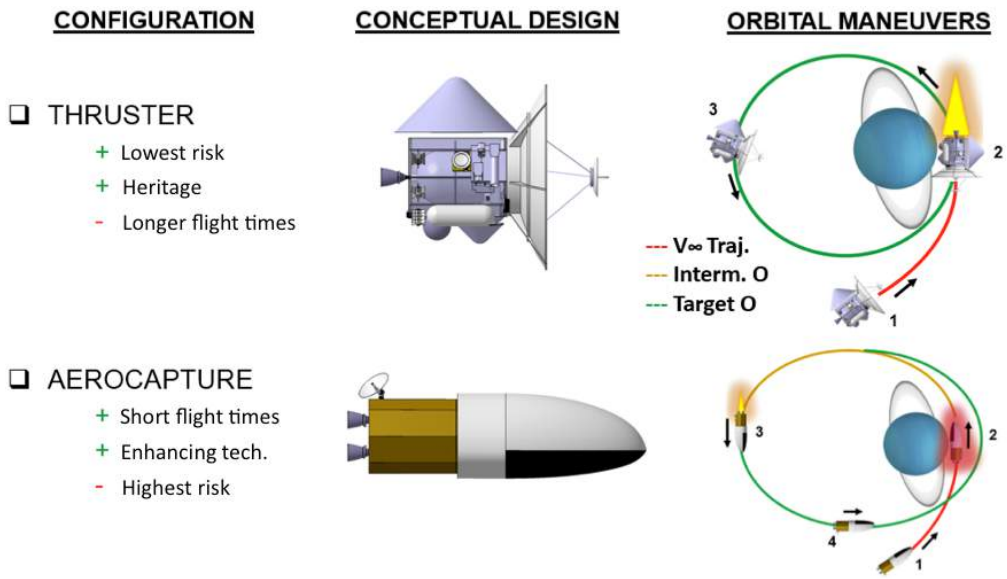

Figure 2.1: Comparison of Uranus Obit Insertion (UOI) Strategies

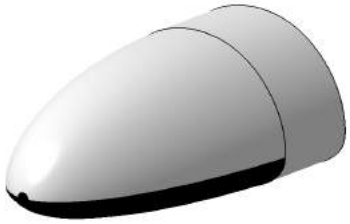

Figure 2.2: Aerocapture Shell

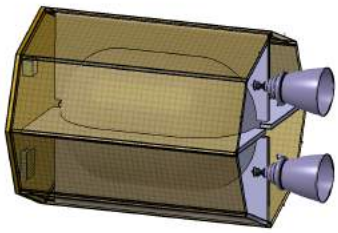

Figure 2.3: Impulsive Capture Rockets

2.3.2 Interplanetary Propulsion

Two methods of interplanetary propulsion were studied: solar electric propulsion (SEP) and conventional impulsive burns using a combination of liquid rocket engines and the Star 48B booster. Solar electric propulsion is a high I_{sp}, low-thrust method of spacecraft propulsion. A key development is the NASA Evolutionary Xenon Thruster (NEXT), which aims to use a 6.9 kW engine to accelerate Xenon ions and provide an I_{sp} of over 4000 s (Schmidt, Patterson, and Benson, 2008). A separable solar-powered stage with 4-6 of these thrusters could provide lower flight times and higher delivered mass at Uranus. It is especially beneficial when used in combination with the Atlas V551 launch vehicle. However, estimated development costs and the superior performance of the SLS compared to the Atlas V with an SEP stage led the study team to disregard SEP for OCEANUS. A detailed analysis of the two methods are addressed in detail in Section 5 and in Appendix E.

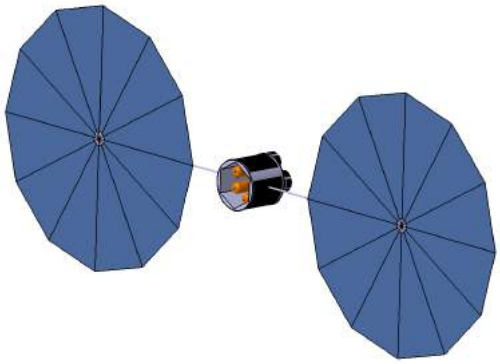

Figure 2.4: Solar Electric Propulsion stage

Figure 2.5: Star 48B Booster

2.3.3 Other Trades

The merits of several other trades and emerging technologies were assessed in this study. These smaller trade studies included atmospheric balloon probes, both as a stand-alone vehicle and as a communications relay for a deep (> 10 bar pressure) atmospheric

descent probe. Also explored were the benefits of numerous small scout probes for testing the upper atmosphere of Uranus prior to aerocapture of the main spacecraft. Unfortunately, all of these options were found to add unnecessary complexity to the mission concept and were fraught with various technical challenges.

Meanwhile, an important trade for the telecommunications system was the selection of a fixed high-gain antenna over a deployable version or a novel optical communication system. Optical communication systems utilize a visible or infrared laser to transmit data across free-space at data rates far in excess of what is possible using traditional radio and microwave instruments. An optical system would allow for more data-intensive science operations. A laser communication system was successfully demonstrated onboard the *Lunar Atmosphere Dust and Environment Explorer* (LADEE) spacecraft in 2013 and variants capable of transmitting over interplanetary distances are currently estimated at around TRL 6 (Elphic et al., 2014; Cornwell, 2016). Unfortunately, laser communications are especially vulnerable to atmospheric disturbances, meaning that a large high-gain radio-frequency antenna would still be required on the orbiter to receive data from the entry probes. Given that an appropriately sized high-gain antenna provided both ample data rates and fit within the 5 m payload fairing of the SLS Block 1B, the team elected to equip OCEANUS with a fixed 4 m high-gain antenna.

Lastly, the team assessed the risks and benefits of capturing the spacecraft into an orbit that passed inside of Uranus' rings. Passing inside the rings would provide two main benefits. First, the lower periapse would reduce the ΔV of the capture compared to a capture performed entirely outside the rings. Second, tracking the spacecraft through a low ($<1.5\ R_U$) periapse would allow for refinement of Uranus' zonal higher-order dynamics terms, thus aiding studies of its interior. However, a trajectory that passes inside of the rings may expose the spacecraft to the risk of impact with ring material. Since the distribution of ring material is at present poorly understood, it was elected to postpone any investigations passing inside the rings until the end of the 2-year primary mission.

2.3.4 Preliminary Flight System Configurations

From the proposed mission architectures, corresponding flight system configurations were assessed for feasibility to identify additional requirements for the high level system. An example would be the necessity of a gimballed medium gain antenna when using SEP systems to be able to communicate with DSN during the continuous low-thrust phase of the mission. For aerocapture, the need for compact placement inside the aeroshell necessitates either a deployable antenna or optical laser communication. The preliminary flight systems for the major system-level trades are shown in Figure 2.6.

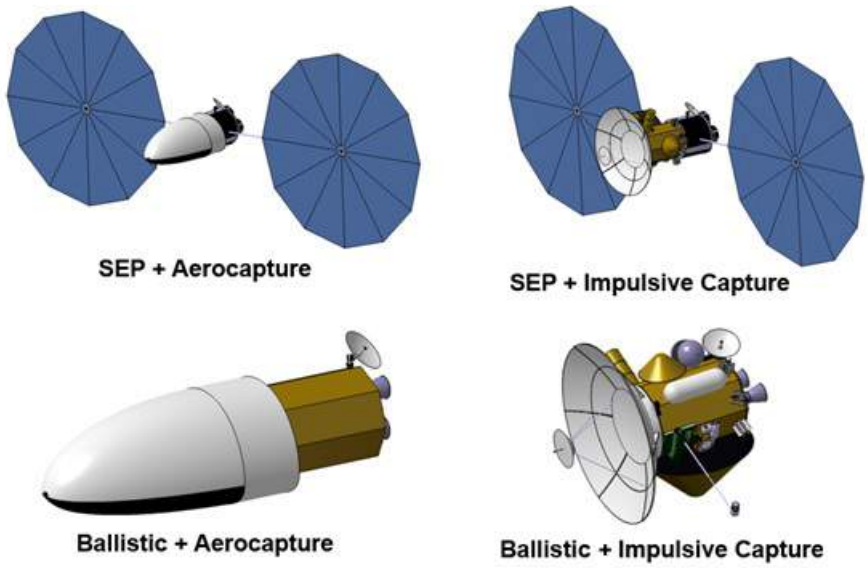

Figure 2.6: Flight system configurations

2.3.5 Trade Study Table

The essential trade elements and options of the OCEANUS concept study are summarized along with the final selections in Table 2.2.

Table 2.2: Trade study tree

TRADE ELEMENT	DECISION DRIVER	OPTIONS			
Launch Vehicle	Mass Delivered and TOF	Atlas V 551	SLS Block 1B	**SLS Block 1B with Star 48 B Booster**	
Mission Trajectory	Mass Delivered, TOF and Cost	**Ballistic**		Low Thrust SEP	
Uranus Capture	Cost and Risk	**Impulsive**	Aerocapture	Inside Rings	**Outside Rings**
Probes Number and Destination	Science and Cost	**1 Saturn, 1 Uranus**	2 Uranus	1 Uranus	
Additional Probes	Cost and Trajectory	**None**	Scout Probe	Duration Balloon	
Descent Depth	Science and Telecommunications	40 bars	20 bars	**10 bars**	
Primary Antenna	Science and Trajectory	**Fixed HGA**	Deployable HGA	Optical	

***Final Selected Design Option**

2.4 Enhancing and Enabling Technologies

The OCEANUS preferred design leverages several enhancing and enabling technologies. Mission enhancing technologies are those that improve a mission critical aspect such as science return, deliverable mass, power consumption, and so on. Mission enabling technologies are critical technologies that must be developed in order for the mission concept to be considered feasible. The OCEANUS mission includes one enhancing technology and requires two enabling technologies as outlined.

2.4.1 Enhanced Multi-Mission Radioisotope Thermoelectric Generator

Radioisotope thermoelectric generators (RTGs) are a common method for powering interplanetary spacecraft. They convert heat from a radioactive isotope into electric energy. The enhanced multi-mission radioisotope generator (eMMRTG) represents the next generation of this technology and is included as an enhancing technology on OCEANUS. The eMMRTG is expected to be TRL 9 by the earliest launch opportunity considered in this study (2023), since it is planned to be flown on Mars 2020. For this mission, five eMMRTG's were allocated for power generation. The eMMRTG would enhance the mission by providing a higher power-to-weight ratio than current state-of-the-art RTG's. Figure 2.7 shows a cutaway of the eMMRTG.

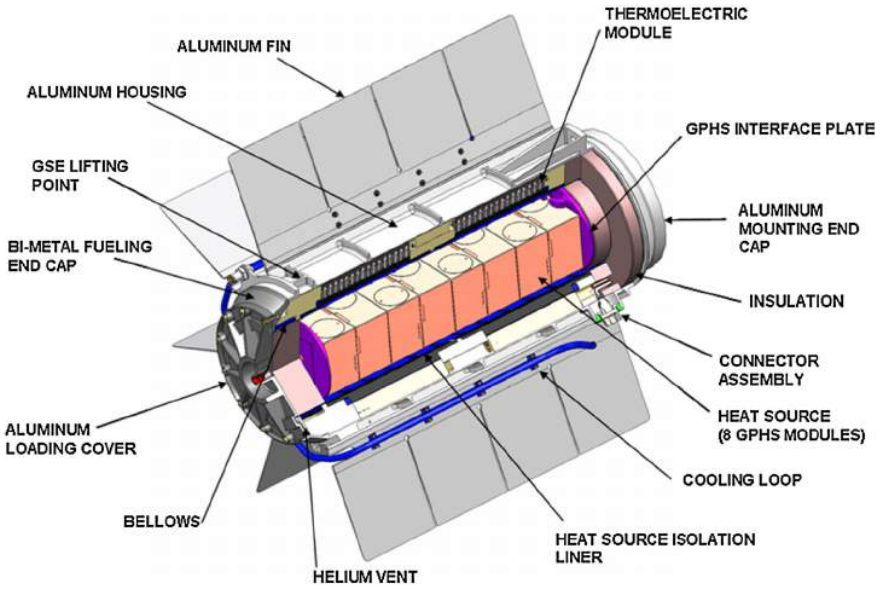

Figure 2.7: eMMRTG cutaway showing the assembly (Hammel and Bennett, 2009)

2.4.2 Patch Antennas

Path antennas are widely used in modern electronics and have begun to be used for space applications in the form of medium gain antennas for small satellites (Antenna Development Corporation, 2009). Variants appropriate for a planetary mission are currently estimated at TRL 5. An important characteristic of patch antennas is their low profile, which allows them to be easily mounted on a flat surface. Patch antennas are used on both of the OCEANUS atmospheric probes and enhance the mission by providing a wide antenna diameter while still remaining low in mass. This allows communication to be sustained through greater depths during the descent of the Saturn and Uranus probes. Figure 2.8 shows an example patch antenna for a small satellite.

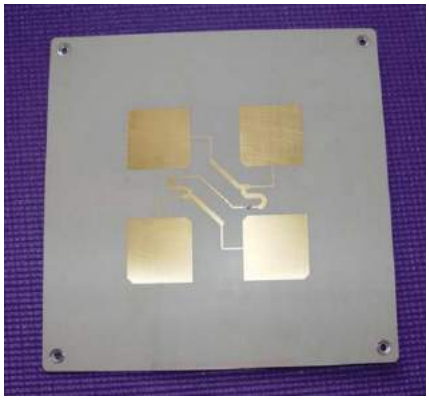

Figure 2.8: Space-rated patch antenna (Antenna Development Corporation, 2009)

2.4.3 Heat Shield for Extreme Entry Environment Technology (HEEET)

HEEET is an emerging 3D woven thermal protection system developed at NASA Ames Research Center and intended to replace the ablative carbon phenolic used in some heritage entry vehicles such as the Galileo probe (Ellerby et al., 2015). The material consists of a high-density carbon fiber weave situated on top of a second layer of lower density blended yarn. Currently estimated at TRL 4, it is capable of withstanding heat fluxes of up to 8 kW/cm^2 and pressures of up to 5.0 atm. The performance characteristics of HEEET make it an enabling technology for both the Saturn and Uranus probes.

3 Science Payload

3.1 Instrument Payload Description

The OCEANUS orbiter is equipped with an array of 9 science instruments to fulfill the remote sensing and *in situ* measurement objectives outlined in the mission science traceability matrix. Each of the atmospheric probes also carry an identical suite of *in situ* experiments to perform investigations not achievable from an orbital platform. The notional instruments that comprise the OCEANUS science payload are described below. In addition to the listed instruments, both probes and the orbiter include an ultra-stable oscillator (USO). The USO is described in detail in Section 4.

3.1.1 Orbiter Payload

Table 3.1: Outer Planet Imager characteristics

Item	Value	Units
Type of instrument	Wide angle camera (WAC)/Narrow angle camera (NAC)	-
Mass	59.6	kg
Power	45.6	W
Dimensions	95 x 75 x 33	cm x cm x cm
Instrument field of view	3.5/0.35	degrees
Uncompressed average science data rate	5	kbps

The main objectives of the Outer Planet Imager (OPI) are to observe giant planet atmospheric structures and processes as well as perform high-resolution imaging of satellite surfaces. The temporal evolution of the Uranian atmosphere is intended to be resolved throughout the 20 day science orbit at multiple spatial scales. Thus, the Outer Planet Imager consists of a wide angle camera (WAC) and narrow angle camera (NAC). The OPI is based on the *Cassini* Imaging Science Subsystem (Porco et al., 2005). The WAC has a 3.5 degree field of view (FOV), and the NAC has a 0.35 degree FOV. The detector for each camera is a 1024 x 1024 CCD array fed by one of 12 spectral filters on a moveable wheel. Each instrument produces 1.05 Mbit images with 8× compression. The worst resolution attained is ~90 km/px by the WAC at apogee. The highest resolution attained is ~0.2 km/px by the NAC at perigee. A total of 907 images per orbit are expected from the WAC and 226 expected from the NAC (Ice Giants Decadal Study, 2010).

Table 3.2: Magnetometer characteristics

Item	Value	Units
Type of instrument	Magnetometer	-
Mass	8.8	kg
Power	12.6	W
Dimensions	8 x 5 x 5/13 x 10 x 9	cm x cm x cm
Instrument field of view	360	degrees
Uncompressed average science data rate	2	kbps
Sample rate	1 – 20	Hz
Range	0.1 – 2000	nT

The scientific objectives of the OCEANUS magnetometer (MAG) are to understand the planets' and moons' magnetosphere structure and origin. This is accomplished by taking continuous measurements of the magnetic field during flight. The instrument divided into two sets placed along a 10 m boom in order to avoid interference from the spacecraft's magnetic fields. MAG includes a vector helium magnetometer placed at the end of the boom for scalar measurements and a 3-axis fluxgate magnetometer placed halfway along the boom for vector measurements. During interplanetary flight, when the spacecraft is far away from any planet's magnetic field, samples will be taken at 1 Hz. When approaching the magnetopause and once inside the magnetosphere the instrument will sample at 20 Hz. Each sample is 30 bits with 2× compression. The instrument will produce roughly 6.48 Mbits of data per day, given an average of 2.5 samples/s. The MAG is based on the magnetometer aboard *Cassini* (Dougherty et al., 2004).

Table 3.3: Visible/near-IR Spectrometer characteristics

Item	Value	Units
Type of instrument	Vis/NIR spectrometer	-
Mass	10.5	kg
Power	7.1	W
Dimensions	50 x 41 x 30	cm x cm x cm
Instrument field of view	5.7 x 0.037/5.7 x 0.15	degrees
Uncompressed average science data rate	7.8	kbps

The science objectives of the Visible/near-IR Spectrometer (VNIS) are to measure the composition and structure of the Uranian and Saturnian atmospheres. Other objectives include the examination of satellites and rings. This instrument is based on the Ralph instrument on *New Horizons* (Reuter et al., 2008). VNIS includes five filters: panchromatic (400 – 975 nm), red (540 – 700 nm), blue (400 – 550 nm), near-IR (780 – 975 nm), and methane (860 – 910 nm). Each sample is 3.36 x 10^7 bits with 8× compression. VNIS is expected to return 53 image cubes per orbit (Ice Giants Decadal Study, 2010).

Table 3.4: UV Spectrograph characteristics

Item	Value	Units
Type of instrument	UV spectrograph	-
Mass	4.4	kg
Power	4.3	W
Dimensions	44 x 24 x 22/13 x 6 x 9	cm x cm x cm
Instrument field of view	6	degrees
Uncompressed average science data rate	0.272	kbps

The science objectives of the Ultra-violet Spectrograph (UVS) are to perform occultation and airglow measurements of Uranus' atmosphere and satellites. The UVS detector is a 1024 x 32 pixel CCD and is based on the Alice instrument aboard *New Horizons* (Stern et al., 2008). It consists of a telescope feeding into a Rowland-circle spectrograph. Each measurement is 32.9 kbits with 8× compression. The UVS has a FOV of 6 degrees and can achieve a resolution of >20 km/px when closer than ~8 R_U. Each orbit is expected to produce approximately 138 images (Ice Giants Decadal Study, 2010).

Table 3.5: Mid-Infrared Radiometer characteristics

Item	Value	Units
Type of instrument	Radiometer	-
Mass	9	kg
Power	18	W
Dimensions	95 x 75 x 33	cm x cm x cm
Instrument field of view	4.3	degrees
Uncompressed average science data rate	2	kbps
Number of channels	9	-

The scientific objectives of the Mid-Infrared Radiometer (MIR) are to measure the atmospheric thermal structure in vertical slices. MIR uses nine channels, ranging from 0.3 to 400 µm. Each channel examines reflected solar and emitted radiation as well as molecular bands beyond the range of VNIS. Each filter consists of a 256 x 256 pixel array and produces an image 1.3 x 10^5 bits in size with 8× compression. A total of 311 observations are expected each orbit (Ice Giants Decadal Study, 2010). This instrument is based on the Mars Climate Sounder instrument aboard the *Mars Reconnaissance Orbiter* (McCleese et al., 2007).

Table 3.6: Suprathermal Particle Imager characteristics

Item	Value	Units
Type of instrument	Suprathermal particle imager	-
Mass	3.3	kg
Power	3	W
Dimensions	6 x 6 x 3	cm x cm x cm
Instrument field of view	360 x 6	degrees
Uncompressed average science data rate	2	kbps
Ion Energy Range	0.1 – 30,000	eV
Ion Mass Range	1 - 70	amu

The science objectives of the Suprathermal Particle Imager (SPI) are to measure ion energy, angle, and composition. This will help characterize the structure and dynamics of Uranus' magnetosphere, including its interaction with the upper atmosphere. The SPI will measure particles ranging in mass from 1 – 70 amu and detect energies from 0.1 – 30,000 eV using a toroidal electrostatic analyzer and a time of flight analyzer. The SPI is expected to produce 250 Mbit of data per orbit with 3× compression (Ice Giants Decadal Study, 2010). SPI is based on the Suprathermal and Thermal Ion Composition instrument aboard *Maven* (McFadden et al., 2015).

Table 3.7: Energetic Particles Experiment characteristics

Item	Value	Units
Type of instrument	Energetic particle detector	-
Mass (total)	19.2	kg
Power (total)	9.3	W
Dimensions (each)	23.3 x 16.9 x 12.8	cm x cm x cm
Uncompressed average science data rate	1	kbps
Range	1 – 20,000	keV

The scientific objectives of the Energetic Particles Experiment (EPE) are similar to those of the SPI, but for higher energy particles. This instrument will detect particles in the 1 – 20,000 keV range in order to characterize Uranus' radiation belts and energization processes. The EPE consist of 3 instruments located around the orbiter bus and each includes a microchannel plate to perform time of flight measurements of incoming ions. Solid-state detectors measure the total energy of the ions. The EPE will operate continuously and will produce approximately 275 Mb of data per orbit. The EPE is based on the Jupiter Energetic-particle Detector Instrument aboard *Juno* (Mauk et al., 2013).

Table 3.8: Cosmic Dust Experiment characteristics

Item	Value	Units
Type of instrument	Dust analyzer	-
Mass	17.1	kg
Power	12	W
Dimensions	14 x 10 x 11	cm x cm x cm
Instrument field of view	45	degrees
Uncompressed average science data rate	0.524	kbps

The science objectives of the Cosmic Dust Experiment (CDE) are to measure the mass, chemical composition and dynamical properties of microscopic dust grains. This will better constrain the extent and density of Uranus' ring system as well as its interactions with the magnetosphere. The CDE consists of a charge detector, an impact ionization detector, and a chemical analyzer. The CDE will take continuous measurements with 3× compression. During the cruise phase the CDE will produce 50 bps of data. During ring passes it will produce 4192 bps. The CDE is based on the Cosmic Dust Analyzer instrument aboard *Cassini* (Srama et al., 2004).

Table 3.9: Plasma Waves Analyzer characteristics

Item	Value	Units
Type of instrument	Plasma wave analyzer	-
Mass	37.7	kg
Power	16.4	W
Dimensions	61 x 67 x 67	cm x cm x cm
Instrument field of view	-	degrees
Uncompressed average science data rate	1	kbps

The science objectives of the Plasma Waves Analyzer (PWA) are to measure electron content and temperature as well as extremely low-frequency radio waves. The PWA uses a Langmuir probe to measure electron density, temperature, and energy (range: 0.7 – 30,000 eV). The PWA also measures electromagnetic waves in the range of 1 Hz – 16 kHz using three 10 m orthogonal deployable monopole antennas. The PWA produces 1 kbps of data during regular operation, but can produce up to 365 kbps during intensive measurements. The PWA is based on the Radio and Plasma Wave Science instrument aboard *Cassini* (Gurnett et al., 2004).

3.1.2 Atmospheric Probe Payload

Table 3.10: Atmospheric Structure Package characteristics

Item	Value	Units
Type of instrument	Atmospheric structure package (temperature, pressure, acceleration)	-
Mass	4	kg
Power	6.3	W
Dimensions	6 x 6	cm x cm
Uncompressed average science data rate	0.05	kbps
Range (acceleration/ temperature/pressure)	(3 μg – 409 g)/ (0 – 500 K)/ (0.1 – 10 bar)	

The science objectives of the Atmospheric Structure Package (ASP) are to measure temperature, pressure, and density of the atmosphere as a function of depth. The instrument is approximately cylindrical and will sample continuously during the probe's descent from 0.1 bar to 10 bar. Temperature and pressure sensors will produce 10 bits/second, while the accelerometer will produce 12 bit/sample. Over the course of the descent, a total 0.27 Mbit will be produced. The ASP is based on the Atmospheric Structure Instrument aboard *Galileo* (Seiff and Knight, 1992).

Table 3.11: Mass Spectrometer characteristics

Item	Value	Units
Type of instrument	Mass spectrometer	-
Mass	13.2	kg
Power	13	W
Dimensions	16 x 31	cm x cm
Uncompressed average science data rate	0.064	kbps

The science objectives of the Mass Spectrometer (MS) are to measure the atmospheric abundances of the noble gases and the isotopic ratios of H, C, N, and O. The MS consists of a gas sampling system and a quadrupole mass analyzer contained in a roughly cylindrical unit. The instrument can measure atomic masses from 2 to 150 amu. Measurements will be performed continuously during the descent from 0.1 bar to 10 bar. The MS is based on the mass spectrometer aboard *Galileo* (Niemann et al., 1992).

Table 3.12: Solar Flux Radiometer characteristics

Item	Value	Units
Type of instrument	Flux radiometer	=
Mass	3.1	kg
Power	4.6	W
Dimensions	13 x 19.5 x 16	cm x cm x cm
Uncompressed average science data rate	0.02	kbps

The scientific objectives of the Solar Flux Radiometer (SFR) are to better constrain the interior heat flux and measure the depths of cloud layers on both Uranus and Saturn. The SFR consists of an optical head that continuously chops between upward and downward facing views. The optics feed 5 spectral channels between 0.3-500 μm to observe methane and water vapor absorption, as well as deposition/loss of internal and solar heat. The SFR is based on the Net Flux Radiometer instrument aboard *Galileo* (Sromovsky et al., 1992).

Table 3.13: Helium Abundance Detector characteristics

Item	Value	Units
Type of instrument	Helium detector	-
Mass	1.4	kg
Power	0.9	W
Dimensions	10 x 10 x 10	cm x cm x cm
Uncompressed average science data rate	0.004	kbps

The science objectives of the Helium Abundance Detector (HAD) are to determine the bulk abundances of helium and hydrogen at Saturn and Uranus. Accurate helium abundance measurements will help to better constrain planetary formation models. The HAD will take samples of gas throughout the probe descent phase. The gas will be scrubbed of NH_3, H_2O, CH_4, and other gasses. The resulting helium mole fraction will then be measured using an interferometer that measures the refractive index of the remaining gasses. The HAD is based on the Helium Abundance Detector instrument aboard Galileo (Zahn and Hunten, 1992).

Table 3.14: Nephelometer characteristics

Item	Value	Units
Type of instrument	Nephelometer	-
Mass	1.3	kg
Power	8.1	W
Dimensions	10 x 15 x 15	cm x cm x cm
Uncompressed average science data rate	0.01	kbps

The scientific objective of the Nephelometer (NEP) is to measure the presence of aerosols and constrain the depth of clouds layers. The NEP uses a pulsed light source (0.9 µm) and a detector to measure scattered light. The NEP will sample from 0.1 to 10 bar. The NEP is based on the nephelometer aboard Pioneer Venus (Ragent et al., 1980).

3.2 Instrument Traceability Matrices

Tables 3.15 and 3.16 provide traceability matrices that relate the various OCEANUS science investigations to the instruments that help fulfill them. This highlights the synergistic measurements accomplished by the science payload and also provides a means of descoping redundant instruments should costs or schedules become prohibitive. In each table the instruments are labeled either as a primary instrument, which measures phenomena directly related to the investigation, or as a secondary instrument, which provides observations that add to the context of the investigation.

Table 3.15: Orbiter instrument traceability matrix. A 'P' denotes that the instrument is primary to the investigation, while an 'S' denotes that it is secondary.

Theme	Investigation	MAG	OPI	VNIS	UVS	MIR	SPI	EPE	PWA	CDE	USO
Magnetosphere	Plasma distribution	S	S	S	S		P	P	S	S	
	Aurora and airglow	S	P	P	P		S	S	S		
	Magnetic field	P									
	3D dust distribution		S							P	
	Plasma waves and electric fields	S					S	S	P		
Interior	Gravity field										P
	Magnetic field	P									
	Atmospheric structure		P	P	S	P					
	Net heat flux		P	P		P					
Atmosphere	Cloud structures		P	S							
	Atmospheric structure			P	S	P					S
	Wind fields		P	S		S					
	Thermal emission		P	S	S	P					
	Aerosols										
Satellites and rings	Ring occultations			P		P					P
	Surface imaging and composition		P	P	S						
	Dust and plasma						P	P	S	P	

Table 3.16: Probe instrument traceability matrix. A 'P' denotes that the instrument is primary to the investigation, while an 'S' denotes that it is secondary.

Theme	Investigation	ASP	MS	SFR	HAD	NEP	USO
Interior	Gravity field						
	Magnetic field						
	Atmospheric structure	P	P	P	P	P	S
	Net heat flux			P			
Atmosphere	Cloud structures		S	P	P	P	
	Atmospheric structure	P	P	P	P	P	S
	Wind fields						P
	Thermal emission			P			
	Aerosols					P	

4 Flight Systems

4.1 Orbiter Flight System Design and Development

A walk-around of the OCEANUS spacecraft is pictured below in Figure 4.1. The walk-around highlights the locations of the science instruments and major subsystems. Placement of components on the 3-axis stabilized spacecraft bus was prioritized by mission criticality, mass, and volume. The bus was structured around the main bi-propellant tank, with the science instruments, high-gain antenna, and probes given priority placement. The Uranus and Saturn probes are anchored to the main bus along central structural reinforcements linked to the main bi-propellant tank. They are placed such that they do not cover any instrument or communication line of sight, and so that their deployment does not intersect with any deployed instruments. The telecommunications subsystem consists of two low-gain antennas, a gimballing medium-gain antenna, a fixed high-gain antenna, and associated electronics. Figure 4.2 depicts the spacecraft with its magnetometer and monopole antennas deployed.

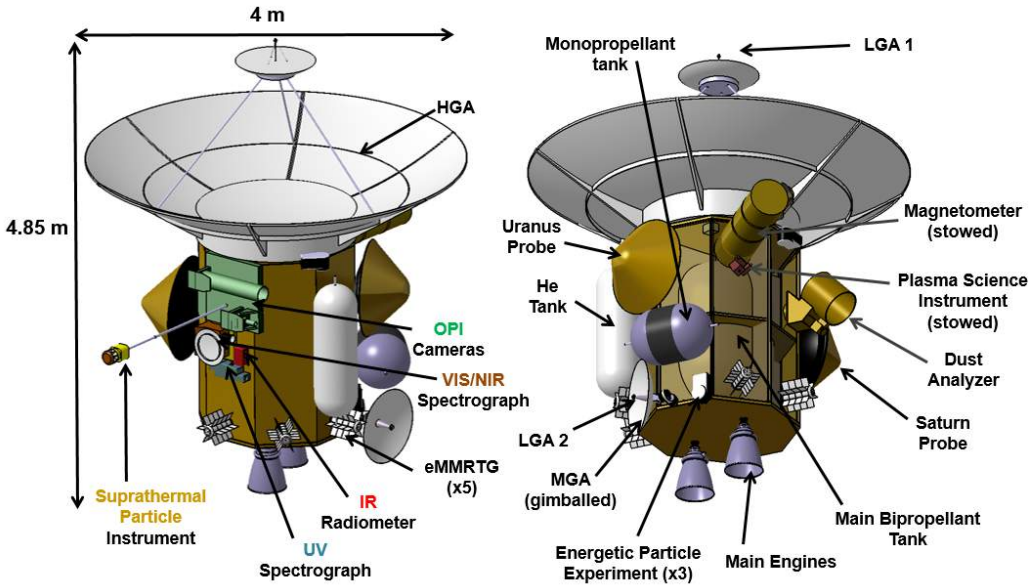

Figure 4.1: OCEANUS spacecraft walk-around. The spacecraft is pictured in the stowed configuration, as it would appear when contained within the 5 m wide fairing of the SLS Bock 1B.

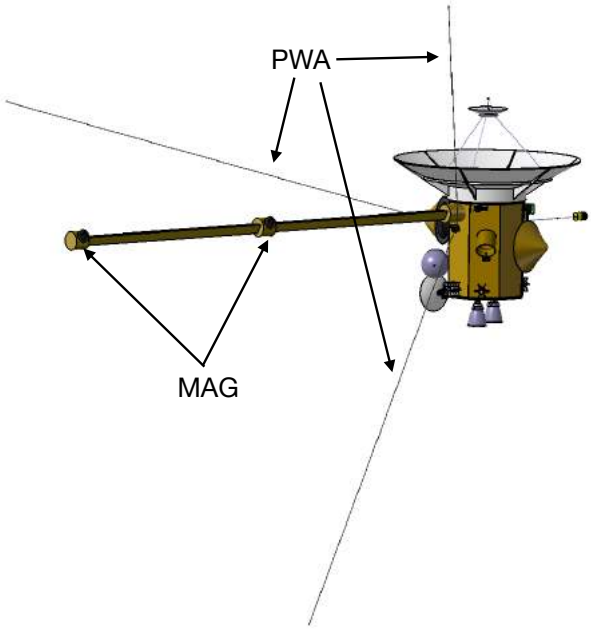

Figure 4.2: Oceanus spacecraft with magnetometer and plasma waves analyzer deployed.

4.1.1 Propulsion

The Propulsion Subsystem provides ΔV and attitude control, momentum management, trajectory correction, and Uranus Orbital Insertion (UOI). To support these activities, the propulsion subsystem utilizes a dual-mode, bipropellant architecture. The spacecraft main bus is centered around the main bipropellant tank (containing both oxidizer and fuel). The monopropellant and pressurant tanks are distributed around the core of the spacecraft. The engines consist of two R-4D 490-N main engines (one flight and one spare), and four 5.3-N attitude-control thrusters. All ΔV maneuvers are designed to be performed by a single main engine, which has an I_{sp} of 316 s (Aerojet-Rocketdyne, 2006a). A cover mechanism for the engines similar to *Cassini*'s was proposed and considered in the mass estimate (Sevilla, 1997). A detailed trade analysis for the rocket engines is given in Appendix B.

4.1.2 Attitude Determination and Control System

The purpose of the Attitude Determination and Control System (ADCS) is to determine the location and orientation of the spacecraft and maintain or adjust its orientation throughout the mission. The preliminary design of the subsystem was based on that from *Cassini-Huygens* due to the similar nature of the missions. After the types of instruments and sensors were selected, they were sized to account for the most demanding requirements for this mission.

The *Cassini* orbiter had two sun sensors, one stellar reference unit (SRU), one Z-axis accelerometer, and two 3-axis inertial reference units for attitude determination, and

it had four reaction wheels and four RCS thruster assemblies for attitude control. The sun sensors and SRU determine the spacecraft's location and orientation based on the stars or sun in the cameras' fields of view. The accelerometer and inertial reference units track the changes in orientation of the spacecraft. The reaction wheels control the orientation of the spacecraft by spinning up or slowing down to store or release angular momentum. The RCS thruster arrays can also control the orientation of the spacecraft, and they are also used to perform small trajectory correction maneuvers and to desaturate the reaction wheels.

After considering modern versions of these components, the ADCS was designed to have 2 SRUs, 3 IMUs, 4 reaction wheels, and 4 RCS thruster assemblies. The SRU and IMU both have redundant units in case the primary units fail. The reaction wheels are mounted such that three are orthogonal, and the fourth is skewed in all three axes.

Since the mechanical design of the spacecraft is in preliminary stages, the moment of inertia of the spacecraft was approximated as a rod with a diameter and height of 5 m, and a mass of 1500 kg. The momentum wheels must be sized to be able to orient the spacecraft of this size at the maximum required rate, which for this mission will be moon flybys near Uranus. The maximum rate was calculated assuming the spacecraft flies by at a radius of 1500 km, which gives a slew rate of 0.57 deg/s. Since the locations of the instruments is not final and the direction in which the spacecraft must move during the flybys are not known, it was assumed that the spacecraft would have to rotate about its highest moment of inertia axis. This gives are required momentum of 55 Nms and a required torque of 0.082 Nm. Finally, the amount of propellant required for the RCS thrusters was approximated by finding the propellant mass used for two hours of constant thrusting, which is 86 kg.

The selected reaction wheel is a Honeywell Constellation Series reaction wheel. It has a maximum momentum of 75 Nms, a maximum torque of >0.1 Nm, a mass of 10.4 kg, and a steady state power of 22 W (Honeywell International, 2003). Each wheel can provide a maximum slew rate of 0.79 deg/s. The selected RCS thruster is a MR-111C 4 N monopropellant thruster from Aerojet Rocketdyne. The thruster has an I_{sp} of 229 s and a mass of 0.33 kg (Aerojet-Rocketdyne, 2006b). The RCS thrusters will have sufficient propellant for three hours of continuous thrusting. Table 4.1 below provides a summary of the required and delivered performance characteristics of the attitude control system.

Table 4.1: Attitude control system specifications

Quantity	Required	Delivered	Unit
Slew Rate	0.57	0.79	deg/s
Momentum	55	75	N*m*s
Torque	0.082	>0.1	N*m
Propellant	86	104	Kg

Each wheel has a mass of 10.6 kg, so the mass of the 4 wheels is 42.4 kg. Each thruster has a mass of 0.33 kg, so the mass of the 4 array of 4 thrusters is 5.3 kg. The

hydrazine tanks have a mass of 15 kg, and the propellant mass is 104 kg. In total, the system has a mass of 167 kg before contingency. Due to uncertainties in the design, the maximum expected value of the system with a 20% contingency is 200 kg.

4.1.3 Power and Thermal Design

The power source for this spacecraft is a power plant of five eMMRTG's. The power system is sized to accommodate the failure of one RTG. Excess power is stored in an internally redundant 624 W-h lithium-ion battery or dumped as heat through a thermal shunt. For transient mission phases that require more power than produced by the RTG's in steady state, additional power is temporarily drawn from the battery. Power is distributed by a power conditioning and distribution unit of *Galileo* heritage. Developed by Terma Space (2016), the unit is designed with full redundancy and is pictured below in Figure 4.3. The dimensions of the unit are 50.8 cm x 23.5 cm x 15.6 cm.

Figure 4.3: Power conditioning and distribution unit developed by Terma Space for the Galileo mission (Terma Space, 2016).

Thermal regulation of the spacecraft and is accomplished via a combination of passive and active mechanisms. The orbiter includes 117 radioisotope heating units (RHUs), an optical solar reflector (OSR), 170 heat pipes, and 14 louvers, as well as 12.6 kg of multi-layer insulation (MLI). More details regarding thermal design are given in Appendix C.

4.1.4 Telecommunications, Command, and Data Handling

OCEANUS' telecommunications subsystem consists of several antennas and their associated electronics. The primary antenna is a 4-m diameter parabolic high-gain antenna (HGA) implemented with *Cassini-Huygens* heritage (Taylor et al., 2002). Forward and aft 6.4 cm diameter low-gain antennas (LGA) allow omnidirectional communication for emergencies or during maneuvers and are also similar to the LGAs on *Cassini*. Finally, a gimbaled 0.8 m parabolic medium-gain antenna (MGA) near the rear of the orbiter performs real-time data relaying to Earth during planetary entry of the atmospheric probes, when the forward HGA is focused on receiving data from the probe. The MGA also serves as back up to the HGA. Uplinks and downlinks with the orbiter are performed using the X and Ka frequency bands, while probe communications are at a ultra-high frequency (UHF) of 405 MHz in order to limit atmospheric attenuation.

A central component of the telecomm subsystem is the ultra-stable oscillator (USO), which serves as a highly precise frequency reference using a piezoelectric crystal. In addition to regulating the frequency of telecommunications, the USO is critical to radio science measurements performed by the orbiter. The USO used on the OCEANUS orbiter and probes is based on *Cassini* heritage and is pictured in Figure 4.4. The dimensions are 16.8 cm x 10.2 cm x 10.2 cm.

In addition to the USO, the telecommunications subsystem includes a deep space transponder, travelling wave tube amplifiers, waveguide transfer switches, diplexers, and isolators, with flight heritage taken from various missions. Details of these components are included in Appendix F. For communicating with the entry probes, the orbiter and probes also include a UHF transceiver. The transceiver selected in this study is the Electra-lite transceiver developed by L-3 Communications Cincinnati Electronics, which is space rated, radiation-resistant, and can be adapted to any mission design demands, such as a low data rate of 200 bps for deep space missions (L-3 Communications, 2007). The transceiver is pictured in Figure 4.4. The dimensions are 16.1 cm x 20.3 cm x 10.4 cm.

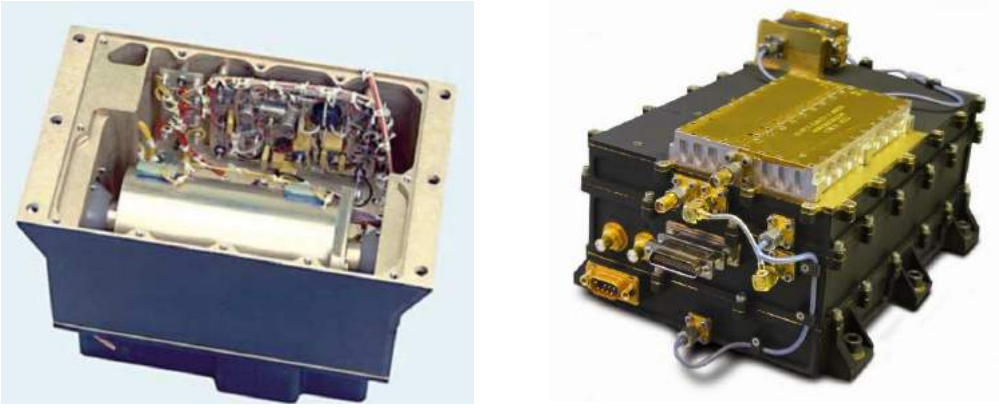

Figure 4.4: Left - Ultra-stable oscillator developed by the Applied Physics Laboratory at Johns Hopkins University (Suter et al., 2001). Right – Electra-lite UHF transceiver.

The computer of the orbiter is a RAD750® 6U CompactPCI single-board computer developed by BAE Systems (2016). The computer uses a PowerPC RAD750® microprocessor that is resistant to radiation in order to be used for deep space missions. It is pictured in Figure 4.5 with a volume of 23.3cm x 22.0 cm x 1.0 cm. In order to limit risk for the command and data handling subsystem, two single computers are included on OCEANUS for full redundancy. Data storage is handled by a solid-state recorder similar to the one developed by Airbus Defense & Space (2014). This recorder provides 4 Tbits of storage and is pictured in Figure 4.5 with a volume of 25.0 cm x 25.0 cm x 8.0 cm.

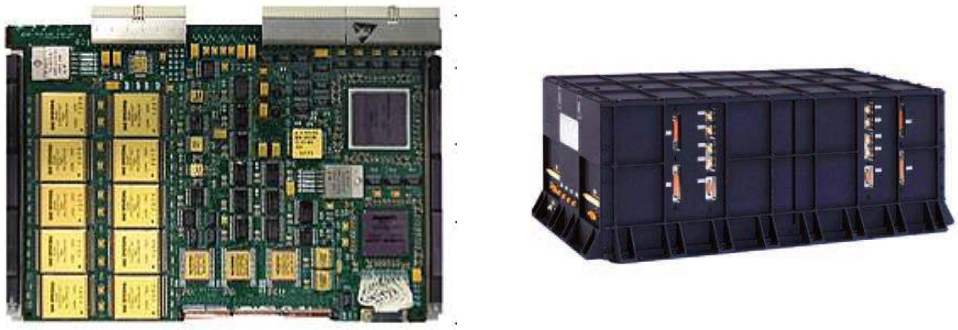

Figure 4.5: Left - RAD750® 6U CompactPCI single-board computer by BAE Systems (2016). Right – Solid-state recorder from Airbus Defense and Space (2014).

4.1.5 Structures and Mechanisms

The orbiter bus structure is designed to support the main bipropellant tank, in a configuration similar to *Cassini*. The option of adopting the *Cassini* metallic monocoque bus structure was considered. Instead, after consulting heritage spacecraft and studying modern bus architectures, a structure composed of carbon fiber panels (with aluminum honeycomb) was adopted (ESA, 1988; O'Neil and Mitchell, 1983). Two probe launch mechanisms and a dish mount were also included in the structural mass estimate. The probe launch mechanism is a non-pyrotechnic device developed by NEA Electronics (2016).

The structural mass was not calculated, but estimated as a mass percentage of the orbiter mass. A structural octagon comprised of panels with carbon fiber facings and a 5052 aluminum honeycomb core was chosen for the orbiter bus. A fraction of 25% of the total orbiter dry mass was projected to be structural mass, which is considered a conservative estimate compared to the 20% usually applied (Wijker, 2008). A 30% contingency is added for the final MEV.

4.1.6 Orbiter Mass and Power Summary

Table 4.2: OCEANUS orbiter mass-power summary

Orbiter						
Subsystem	**Total CBE Mass (kg)**	**Cont.**	**Total MEV Mass (kg)**	**Total CBE Power (W)**	**Cont.**	**Total MEV Power (W)**
Science Instruments	169.6	5%	178.1	128.3	5%	134.7
Power	245.8	5%	258.9	28.3	10%	31.1
Thermal	74.5	20%	89.4	1.0	30%	1.3
Propulsion	178.7	5%	187.8	58.9	5%	61.8
Telecommunications	142.3	20%	170.4	289.3	21%	348.7
Command and Data Handling	37.9	14%	43.0	69.5	10%	76.5
Attitude Controls	54.3	20%	65.2	159.6	20%	191.5
Mechanism and Structures	270.0	30%	351.0	N/A	N/A	N/A
Total Dry Mass	**1173.0**	**15%**	**1343.8**			
Dry Mass Margin		30%	502.7			
Maximum Total Dry Mass			**1675.7**			

Table 4.3: OCEANUS orbiter detailed mass-power breakdown

Subsystem	Unit Mass CBE (kg)	# Of Units		Flight Hardware Masses			Unit Power CBE (W)	Flight Hardware Power		
		Flight Units	Flights Spares	Total CBE Mass (kg)	Contingency	Total MEV Mass(kg)		Total CBE Power (W)	Contingency	Total MEV Power (W)
Science Instruments										
Magnetometer	8.8	1	0	8.8	20.0%	10.6	12.6	12.6	5.0%	13.2
WAC/NAC	59.6	1	0	59.6	20.0%	71.5	45.6	45.6	5.0%	47.9
VIS/NIR Spectrograph	10.5	1	0	10.5	20.0%	12.6	7.1	7.1	5.0%	7.5
UV Spectrograph	4.4	1	0	4.4	20.0%	5.3	4.3	4.3	5.0%	4.5
Mars Climate Sounder II	9.0	1	0	9.0	20.0%	10.8	18.0	18	5.0%	18.9
Superathermal Particle Imager	3.3	1	0	3.3	20.0%	4.0	3.0	3	5.0%	3.2
Energetic Particles Experiment	19.2	1	0	19.2	20.0%	23.0	9.3	9.3	5.0%	9.8
Plasma Waves Experiment	37.7	1	0	37.7	20.0%	45.2	16.4	16.4	5.0%	17.2
Total (Sci. Int.)				**160.9**		**168.9**		**128.3**		**134.7**
Power										
Batteries	4.5	1	0	4.5	5.0%	4.7	0.0	0	5.0%	0.0
Power Unit	16.3	1	0	16.3	10.0%	17.9	28.3	28.3	10.0%	31.1
eMMRTG	45.0	4	0	180.0	10.0%	198.0	0.0	0	5.0%	0.0
Total (Power)				**301.5**		**326.2**		**28.3**		**31.1**
Thermal										
MLI	12.6	1	0	12.6	20.0%	15.1	0.0	0	5.0%	0.0
OSR	1.3	1	0	1.3	20.0%	1.6	0.0	0	5.0%	0.0
RHU	6.3	1	0	0.0	20.0%	0.0	0.0	0	5.0%	0.0
Heat Pipes	49.6	1	0	49.6	20.0%	59.5	0.0	0	5.0%	0.0
Thermal Louvers	11.0	1	0	11.0	20.0%	13.2	1.0	1	30.0%	1.3
Total (Thermal)				**74.5**		**89.4**		**1.0**		**1.3**
Propulsion										
Hydrazine and Nitrogen Tetroxide Tanks	61.0	1	0	61.0	5.0%	64.1	4.3	4.3	5.0%	4.5
Helium Tank	25.0	1	0	25.0	5.0%	26.3	4.3	4.3	5.0%	4.5
Helium Pressurant	9.1	1	0	9.1	5.0%	9.5	0.0	0	0.0%	0.0
Monopropellant Tanks	15.0	1	0	15.0	5.0%	15.8	4.3	4.3	5.0%	4.5
R-4D 445N Rocket Engine	4.3	1	1	8.6	8.0%	9.3	46.0	46	5.0%	48.3
Tanking Structure	60.0	1	0	60.0	5.0%	63.0	0.0	0	0.0%	0.0
Total (Propulsion)				**178.7**		**187.8**		**58.9**		**61.8**
Command and Data Handling										
Processor	1.2	1	1	2.4	10.0%	2.7	14.0	14	10.0%	15.4
Storage	14.0	1	0	14.0	10.0%	15.4	35.0	35	10.0%	38.5
Mission Timer Unit	3.2	2	0	6.4	10.0%	7.0	19.5	19.5	10.0%	21.5
Probe Launch Mec	0.7	2	0	1.4	10.0%	1.5	1.0	1.0	10.0%	1.1
Cables and Harness	13.6	1	0	13.6	20.0%	16.3	0.0	0	30.0%	0.0
Total (CD&H)				**37.9**		**43.0**		**69.5**		**76.5**

Table 4.3: OCEANUS orbiter detailed mass-power breakdown (continued)

Subsystem	Unit Mass CBE (kg)	# Of Units		Flight Hardware Masses			Unit Power CBE (W)	Flight Hardware Power		
		Flight Units	Flights Spares	Total CBE Mass (kg)	Contingency	Total MEV Mass(kg)		Total CBE Power (W)	Contingency	Total MEV Power (W)
Telecommunications										
High Gain Antenna	100.6	1	0	100.6	20.0%	120.7	0.0	0	20.0%	0.0
Medium Gain Antenna	5.0	1	0	5.0	20.0%	6.0	0.0	0	20.0%	0.0
Low Gain Antenna	0.5	2	0	1.0	20.0%	1.2	0.0	0	20.0%	0.0
Gimbal	5.0	1	0	5.0	20.0%	6.0	22.6	22.6	20.0%	27.1
Deep Space Transponder	3.2	2	0	6.4	20.0%	7.7	19.5	19.5	20.0%	23.4
X-Band TWTA	1.0	3	0	2.9	20.0%	3.5	120.0	120	20.0%	144.0
Ka-band TWTA	1.5	2	0	3.0	20.0%	3.6	100.0	100	20.0%	120.0
Waveguide Transfer Switch	0.4	5	0	2.0	20.0%	2.4	0.0	0	20.0%	0.0
X-Band/Ka-band diplexer	0.4	2	0	0.8	20.0%	1.0	0.0	0	20.0%	0.0
X-band/Ka-band isolator	0.6	2	0	1.1	20.0%	1.3	0.0	0	120.0%	0.0
Ka-Band Waveguide	0.2	1	0	0.2	20.0%	0.2	0.0	0	20.0%	0.0
X-Band Waveguide	6.3	1	0	6.3	20.0%	7.6	0.0	0	20.0%	0.0
Microwave Components	1.0	1	0	1.0	20.0%	1.2	0.0	0	20.0%	0.0
UHF Electra-Lite	3.0	1	0	3.0	20.0%	3.6	25.0	25	10.0%	27.5
Ultra Stable Oscillator	1.3	2	0	4.0	20.0%	4.8	2.2	2.2	20.0%	6.7
Total (Telecommunications)				**142.3**		**170.7**		**289.3**		**348.7**
Controls										
Attitude Control thruster (5N)	0.3	4	0	1.3	20.0%	1.6	13.6	54.56	20.0%	65.5
Reaction wheel	10.6	4	1	53.0	20.0%	63.6	105.0	105	20.0%	126.0
Total (Controls)				**54.3**		**65.2**		**159.6**		**191.5**
Mechanisms & Structures										
Frame	100.0	1	0	100.0	30.0%	130.0	0.0	0	0.0%	0.0
Dish Mount	50.0	1	0	50.0	30.0%	65.0	0.0	0	0.0%	0.0
Probe Mount	60.0	2	0	120.0	30.0%	156.0	0.0	0	0.0%	0.0
Total (Mechanisms & Structures)				**270.0**		**351.0**		**0.0**		**0.0**

4.2 Entry Probe Design and Development

OCEANUS' two entry probes are designed to perform *in situ* science investigations of Saturn and Uranus' atmospheres. Successful delivery of the science payload to the shallow atmosphere (<10 bars) of either of these planets is complicated by the extreme entry conditions, which feature peak heat rates of nearly 7000 W/cm^2 and peak decelerations of over 100 Earth g. Even after atmospheric entry, the payloads must survive for several hours in the frigid atmosphere as they descend to a target depth of 10 bars pressure. These conditions impose an especially rugged design consisting of a titanium pressure vessel enclosed inside an 45^o sphere-cone aeroshell. The general configuration of the atmospheric probes is depicted below in Figure 4.6 and is based on configuration of the *Galileo* entry probe.

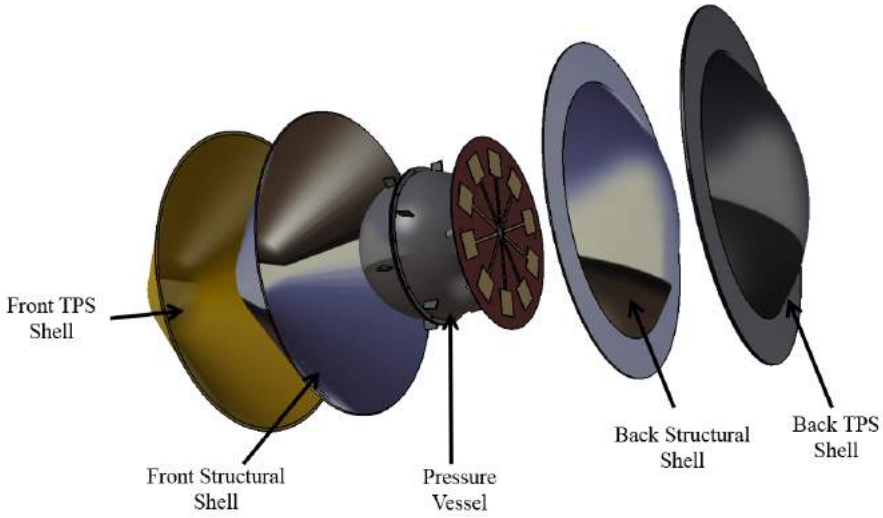

Figure 4.6: Exploded view showing the configuration of the OCEANUS entry probes.

4.2.1 Aeroshell

The Saturn and Uranus probes share the same design in all aspects, except for sizing of the aeroshells and thickness of the thermal protection system (TPS) due to the different entry conditions for each case. The relative size of the two aeroshells is compared in Figure 4.7.

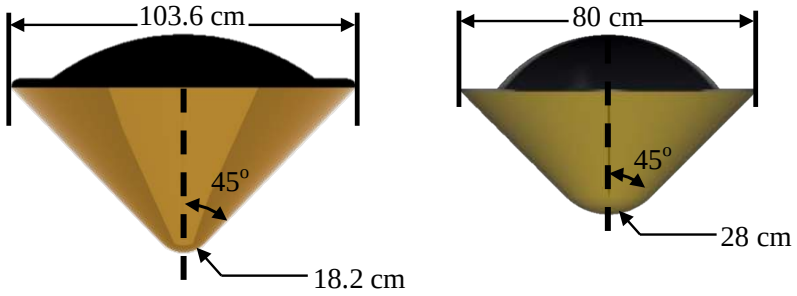

Figure 4.7: Comparison of Saturn (left) and Uranus (right) probe aeroshells.

The TPS material is HEEET as described in Section 2 and serves to protect the pressure vessel from entry heating. Underneath, the structural shell serves as backing for the TPS against the dynamic pressures experienced during entry. The mass of TPS material was determined from simulated heat loads. A detailed analysis is presented in Appendix D. Based on the entry parameters given in Section 5, the TPS masses for the Saturn and Uranus probes are presented in Table 4.4.

Table 4.4: TPS mass breakdown for Saturn and Uranus entry probes.

	Front Shell TPS (kg)	Back Shell TPS (kg)	TPS Structure (kg)
Saturn Probe	23.1	9.2	27.3
Uranus Probe	7.5	3.5	27.3

4.2.2 Pressure Vessel

The aeroshell and any remaining TPS are jettisoned after the entry phase, leaving the spherical pressure vessel. Each vessel is 46 cm in diameter and constructed of 6 mm thick titanium. Numerous vanes protrude from the vessel and function to rotate the module during descent. The vessel contains a set of 5 science instruments, a primary battery for power along with a power distribution unit, on-board computer, SDRAM for data storage, and a patch array antenna with associated electronics for communication. A total of 20 RHUs and both internal (foam) and external (MLI) insulation regulate the temperature of the module. Figures 4.8 and 4.9 depict exploded views of the pressure vessel.

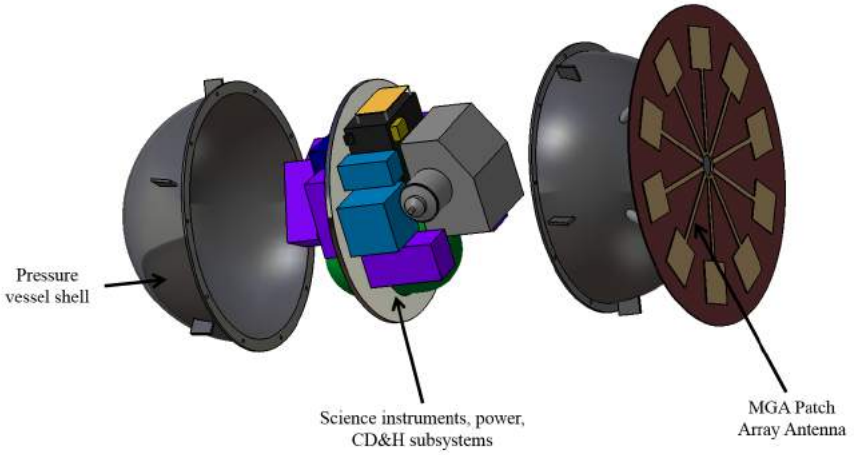

Figure 4.8: Pressure Vessel Configuration

The patch antenna has a diameter of 0.6 m and has an estimated efficiency of 0.5. It is based on designs for CubeSat antennas by the Antenna Development Corporation (2009). As with the orbiter, the probe pressure vessels also contain an Eletra-lite UHF transceiver and a USO to regulate communication frequencies. Power for the module is

distributed from 8 primary batteries by a 10W DC/DC Flexible converter such as the one produced by Thales Alenia Space (2016). Data processing is performed by a fully redundant RAD750® 3U CompactPCI single-board computer that is similar to, though smaller than, the orbiter's onboard computers. Since data storage requirements are much less for the probe than for the orbiter, data is stored on a small, 4.05 g, SDRAM unit produced by 3D-plus (2016). This unit can store up to 2.56 Gbit of data.

The pressure vessel includes a pilot parachute (1.95 m reference diameter) and main parachute (3.1 m reference diameter), similar to the *Galileo* probe. Parachute deployment condition on Saturn and Uranus features low Mach number (~0.55) and high dynamic pressure of (~2000 Pa). To ensure reliable deployment of both the pilot and main parachutes, conical ribbon was chosen based on its stability at high dynamic pressure (up to 7000 Pa), and descent stability (<1° oscillation). Deployment of the parachutes is performed by a pyro unit that is powered by 4 thermal batteries (Eagle-Picher Industries, 2006). The deployment time is controlled by a small mission timer unit similar to the one used on the *Huygens* probe (Clausen et al., 2002). The timer unit also includes two g-switches to start the system and release the parachute should the main unit fail.

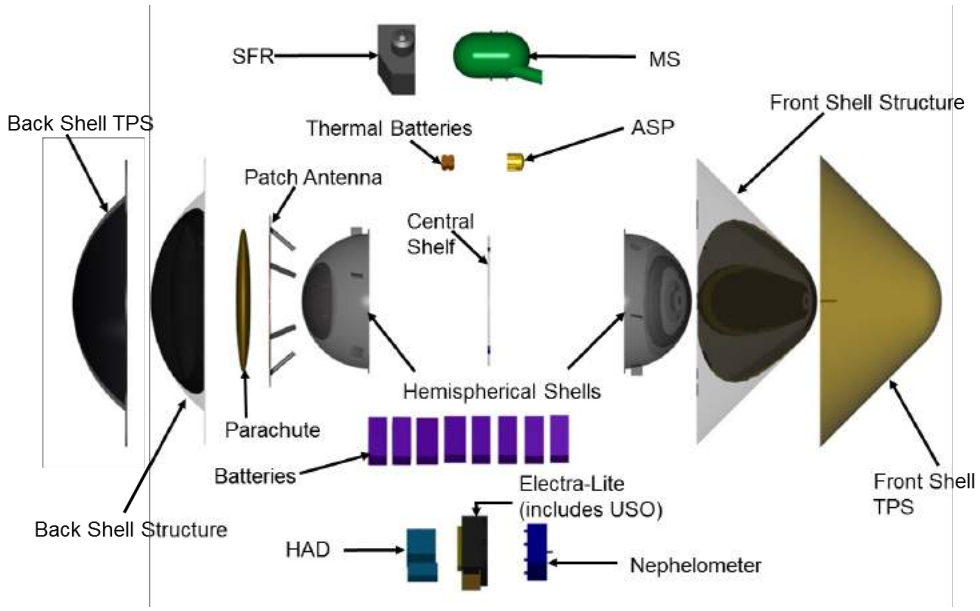

Figure 4.9: Exploded view of entry probe components.

4.2.3 Probe Mass Power Summaries

Table 4.5: Saturn entry probe mass-power summary

Saturn Entry Probe						
Subsystem	**Total CBE Mass (kg)**	**Cont.**	**Total MEV Mass (kg)**	**Total CBE Power (W)**	**Cont.**	**Total MEV Power (W)**
Science Instruments	25.5	5%	26.8	35.9	5%	37.7
Power	8.3	30%	10.8	10.0	10%	11.0
Thermal	7.6	30%	9.9	5.0	20%	6.0
Command and Data Handling	3.1	30%	4.0	14.5	20%	17.4
Telecommunications	5.7	30%	7.4	27.2	20%	32.6
Structures	89.5	30%	116.4	N/A	N/A	N/A
Total Dry Mass	**139.7**	**26%**	**175.3**			
Dry Mass Margin		30%	59.9			
Maximum Total Dry Mass			**199.6**			

Table 4.6: Uranus entry probe mass-power summary

Uranus Entry Probe						
Subsystem	**Total CBE Mass (kg)**	**Cont.**	**Total MEV Mass (kg)**	**Total CBE Power (W)**	**Cont.**	**Total MEV Power (W)**
Science Instruments	25.5	5%	26.8	35.9	5%	37.7
Power	8.3	30%	10.8	10.0	10%	11.0
Thermal	7.6	30%	9.9	5.0	20%	6.0
Command and Data Handling	3.1	30%	4.0	14.5	20%	17.4
Telecommunications	5.7	30%	7.4	27.2	20%	32.6
Structures	68.2	30%	88.7	N/A	N/A	N/A
Total Dry Mass	**118.4**	**25%**	**147.6**			
Dry Mass Margin		30%	50.7			
Maximum Total Dry Mass			**169.1**			

Table 4.7: Saturn entry probe detailed mass-power breakdown

Subsystem	Unit Mass CBE (kg)	# Of Units		Flight Hardware Masses			Unit Power CBE (W)	Flight Hardware Power		
		Flight Units	Flights Spares	Total CBE Mass (kg)	Contingency	Total MEV Mass(kg)		Total CBE Power (W)	Contingency	Total MEV Power (W)
Science Instruments										
Atmospheric Structure Package	4.0	1	0	4.0	5.0%	4.2	6.3	6.3	5.0%	6.6
Mass Spectrometer	13.2	1	0	13.2	5.0%	13.9	13.0	13.0	5.0%	13.7
Nephlometer	1.3	1	0	1.3	5.0%	1.4	8.1	8.1	5.0%	8.5
Net flux radiometer	3.1	1	0	3.1	5.0%	3.3	4.6	4.6	5.0%	4.8
Helium Abundance detector	1.4	1	0	1.4	5.0%	1.5	0.9	0.9	5.0%	0.9
Lightning detector	2.5	1	0	2.5	5.0%	2.6	3.0	3.0	5.0%	3.2
Total (Sci. Int.)				**25.5**		**26.8**		**35.9**		**37.7**
Power										
Primary battery	1.4	5	1	8.3	30.0%	10.8	0.0	0.0	0.0%	0.0
PCDU (Power Conditioning & Distribution Unit)	0.1	1	0	0.1	30.0%	0.2	10.0	10.0	10.0%	11.0
Total (Power)				**8.3**		**10.8**		**10.0**		**11.0**
Thermal										
MLI	2.0	1	0	2.0	30.0%	2.6	0.0	0.0	0.0%	0.0
Insulation	3.8	1	0	3.8	30.0%	4.9	0.0	0.0	0.0%	0.0
RHU	0.7	1	0	0.7	30.0%	0.9	0.0	0.0	0.0%	0.0
Paint	0.0	0	0	0.0	30.0%	0.0	0.0	0.0	0.0%	0.0
Pyro Unit - Thermal Batteries	1.1	1	0	1.1	30.0%	1.4	5.0	5.0	20.0%	6.0
Total (Thermal)				**7.6**		**9.9**		**5.0**		**6.0**
Telecommunications										
MG Patch Array	1.2	1	0	1.2	30.0%	1.6	0.0	0.0	0.0%	0.0
USO	1.3	1	0	1.3	30.0%	1.7	2.2	2.2	20.0%	2.6
Electra-Lite	3.2	1	0	3.2	30.0%	4.2	25.0	25.0	20.0%	30.0
Total (Telecommunications)				**5.7**		**7.4**		**27.2**		**32.6**
Command and Data Handling										
Cables	2.0	1	0	2.0	30.0%	2.6	0.0	0.0	0.0%	0.0
Rad750 single on board computer 3U	0.5	1	1	1.1	30.0%	1.4	11.5	11.5	20.0%	13.8
SDRAM 2.56 Gbits	0.0	1	0	0.0	30.0%	0.0	3.0	3.0	20.0%	3.6
Total (CD&H)				**3.1**		**4.0**		**14.5**		**17.4**
Structures										
Pressure vessel	20.9	1	0	20.9	30.0%	27.2	0.0	0.0	0.0%	0.0
Frontshell TPS	23.1	1	0	23.1	30.0%	30.0	0.0	0.0	0.0%	0.0
Backshell TPS	9.2	1	0	9.2	30.0%	12.0	0.0	0.0	0.0%	0.0
Pilot Chute	1.0	1	0	1.0	30.0%	1.3	0.0	0.0	0.0%	0.0
Main Chute	5.0	1	0	5.0	30.0%	6.5	0.0	0.0	0.0%	0.0
Deployment bag	3.0	1	0	3.0	30.0%	3.9	0.0	0.0	0.0%	0.0
Structures	27.3	1	0	27.3	30.0%	35.5	0.0	0.0	0.0%	0.0
Total (Structures)				**89.5**		**116.4**		**0.0**		**0.0**

Table 4.8: Uranus entry probe detailed mass-power breakdown

Subsystem	Unit Mass CBE (kg)	# Of Units		Flight Hardware Masses			Unit Power CBE (W)	Flight Hardware Power		
		Flight Units	Flights Spares	Total CBE Mass (kg)	Contingency	Total MEV Mass(kg)		Total CBE Power (W)	Contingency	Total MEV Power (W)
Science Instruments										
Atmospheric Structure Package	4.0	1	0	4.0	5.0%	4.2	6.3	6.3	5.0%	6.6
Mass Spectrometer	13.2	1	0	13.2	5.0%	13.9	13.0	13.0	5.0%	13.7
Nephlometer	1.3	1	0	1.3	5.0%	1.4	8.1	8.1	5.0%	8.5
Net flux radiometer	3.1	1	0	3.1	5.0%	3.3	4.6	4.6	5.0%	4.8
Helium Abundance detector	1.4	1	0	1.4	5.0%	1.5	0.9	0.9	5.0%	0.9
Lightning detector	2.5	1	0	2.5	5.0%	2.6	3.0	3.0	5.0%	3.2
Total (Sci. Int.)				**25.5**		**26.8**		**35.9**		**37.7**
Power										
Primary battery	1.4	5	1	8.3	30.0%	10.8	0.0	0.0	0.0%	0.0
PCDU (Power Conditioning & Distribution Unit)	0.1	1	0	0.1	30.0%	0.2	10.0	10.0	10.0%	11.0
Total (Power)				**8.3**		**10.8**		**10.0**		**11.0**
Thermal										
MLI	2.0	1	0	2.0	30.0%	2.6	0.0	0.0	0.0%	0.0
Insulation	3.8	1	0	3.8	30.0%	4.9	0.0	0.0	0.0%	0.0
RHU	0.7	1	0	0.7	30.0%	0.9	0.0	0.0	0.0%	0.0
Paint	0.0	0	0	0.0	30.0%	0.0	0.0	0.0	0.0%	0.0
Pyro Unit - Thermal Batteries	1.1	1	0	1.1	30.0%	1.4	5.0	5.0	20.0%	6.0
Total (Thermal)				**7.6**		**9.9**		**5.0**		**6.0**
Telecommunications										
MG Patch Array	1.2	1	0	1.2	30.0%	1.6	0.0	0.0	0.0%	0.0
USO	1.3	1	0	1.3	30.0%	1.7	2.2	2.2	20.0%	2.6
Electra-Lite	3.2	1	0	3.2	30.0%	4.2	25.0	25.0	20.0%	30.0
Total (Telecommunications)				**5.7**		**7.4**		**27.2**		**32.6**
Command and Data Handling										
Cables	2.0	1	0	2.0	30.0%	2.6	0.0	0.0	0.0%	0.0
Rad750 single on board computer 3U	0.5	1	1	1.1	30.0%	1.4	11.5	11.5	20.0%	13.8
SDRAM 2.56 Gbits	0.0	1	0	0.0	30.0%	0.0	3.0	3.0	20.0%	3.6
Total (CD&H)				**3.1**		**4.0**		**14.5**		**17.4**
Structures										
Pressure vessel	20.9	1	0	20.9	30.0%	27.1	0.0	0.0	0.0%	0.0
Frontshell TPS	7.5	1	0	7.5	30.0%	9.8	0.0	0.0	0.0%	0.0
Backshell TPS	3.5	1	0	3.5	30.0%	4.6	0.0	0.0	0.0%	0.0
Pilot Chute	1.0	1	0	1.0	30.0%	1.3	0.0	0.0	0.0%	0.0
Main Chute	5.0	1	0	5.0	30.0%	6.5	0.0	0.0	0.0%	0.0
Deployment bag	3.0	1	0	3.0	30.0%	3.9	0.0	0.0	0.0%	0.0
Structures	27.3	1	0	27.3	30.0%	35.5	0.0	0.0	0.0%	0.0
Total (Structures)				**68.2**		**88.7**		**0.0**		**0.0**

4.3 Integrated Flight System

The block diagram for the integrated flight system, including the orbiter element and the probe elements, are provided in Figure 4.10.

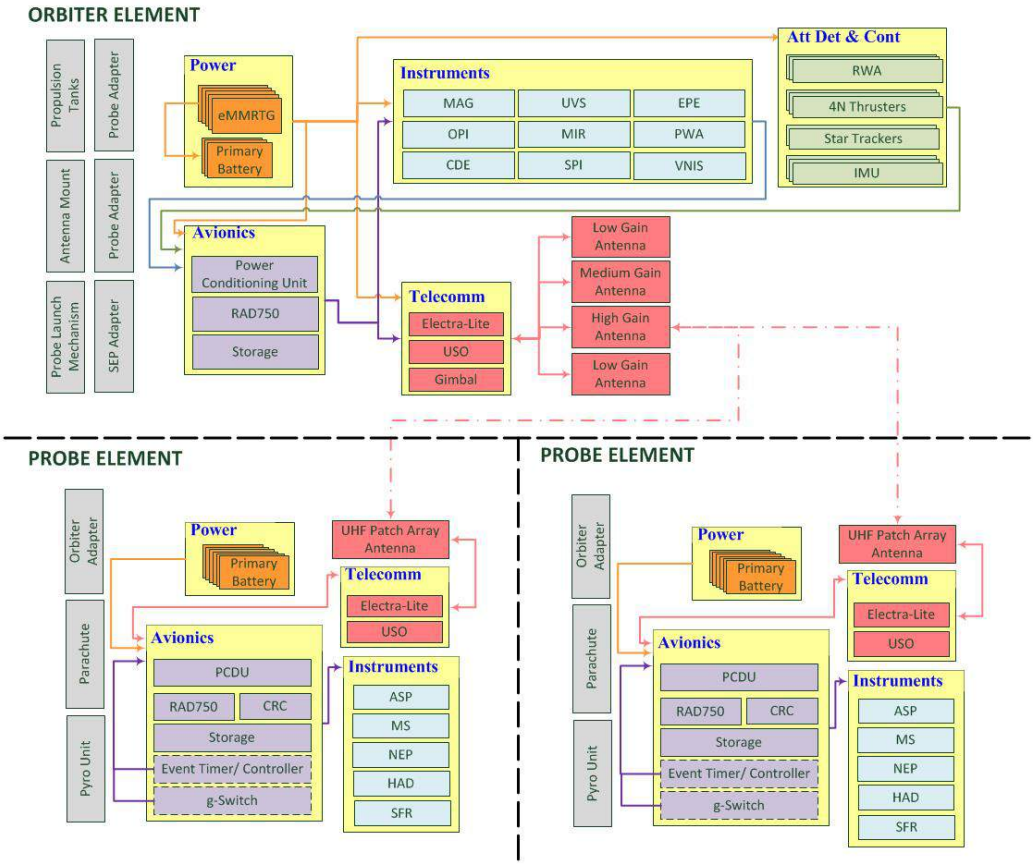

Figure 4.10: Integrated Flight System Block Diagram

5 Mission Design and Operations

5.1 OCEANUS Trajectory Overview

An extensive search of ballistic and chemical impulsive trajectories was performed using JPL-Purdue's STOUR software to develop the solution space of Saturn-Uranus trajectories. The mid-fidelity solutions were compared based on time of flight, distance and relative speed of the Saturn encounter, and the final delivered mass at Uranus. Of these trajectories, as well as a number of low-thrust SEP trajectories using the Atlas V551 launch vehicle, a ballistic Saturn-Uranus launched in 2028 by the SLS was selected by the study team.

Results from the mid-fidelity simulations were be used to run higher-fidelity simulations that form a baseline 2028 SU ballistic trajectory. Using AGI's Systems Tool Kit (STK) software, a converged solution was found with the following properties:

Table 5.1: Baseline trajectory properties

Parameter	Value
Launch Date	Jul 3, 2028
Saturn Flyby Radius	1,120,000 km
Arrival Date	Jan 8, 2040
Time of Flight (TOF)	11.51 yr
Total ΔV	1401 m/s

This high-fidelity interplanetary trajectory is depicted in Figure 5.1.

While the mid-fidelity solution assumes a completely ballistic trajectory until capture, the actual trajectory performs trajectory deflection maneuvers (DMs) prior to the flyby of Saturn and arrival at Uranus in order to target specific encounters. These additional maneuvers, along with a slightly shorter time of flight, account for most of the difference in total required ΔV between the mid-fidelity and higher-fidelity solutions. More information regarding the trajectory trade analyses performed in this study is presented in Appendix E. Other than minor differences, both the mid-fidelity and the higher-fidelity simulations correspond to the same solution. As a result, the trajectories for both simulations are qualitatively the same.

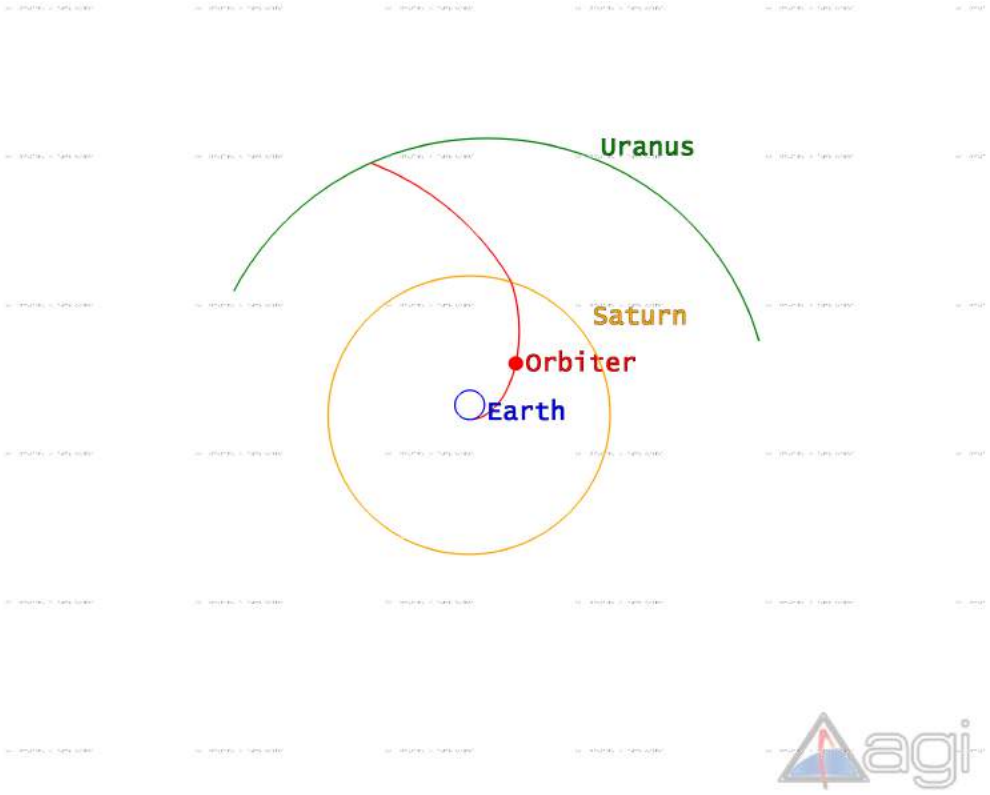

Figure 5.1: The full interplanetary trajectory for the baseline case, as determined by STK.

5.1.1 Earth Escape

The launch segment of the mission was not modeled, and it is assumed that the mission starts after the separation of the orbiter from any launch vehicle components, including the Star 48B booster. The higher-fidelity simulation starts on a hyperbolic escape trajectory with a C_3 of 120.97 km^2/s^2. The Earth escape trajectory places the orbiter on a trajectory that intersects with Saturn. The early phases of this interplanetary cruise may be used to perform a full spacecraft checkout before placing it in a hibernation mode. Once the orbiter approaches Saturn, it will release the first probe and conduct a deflection maneuver to avoid colliding with the planet. The nominal Earth escape trajectory must target entry conditions suitable for the Saturn entry probe.

The selected solution approaches Saturn from its southern hemisphere, and has the potential to cross the ring-plane before entering the atmosphere. In order to avoid this, the entry flight path angle was specified such that atmospheric entry occurs before the ring-plane crossing while still ensuring feasible probe entry conditions. Figure 5.2 depicts the geometry of the probe's approach and entry.

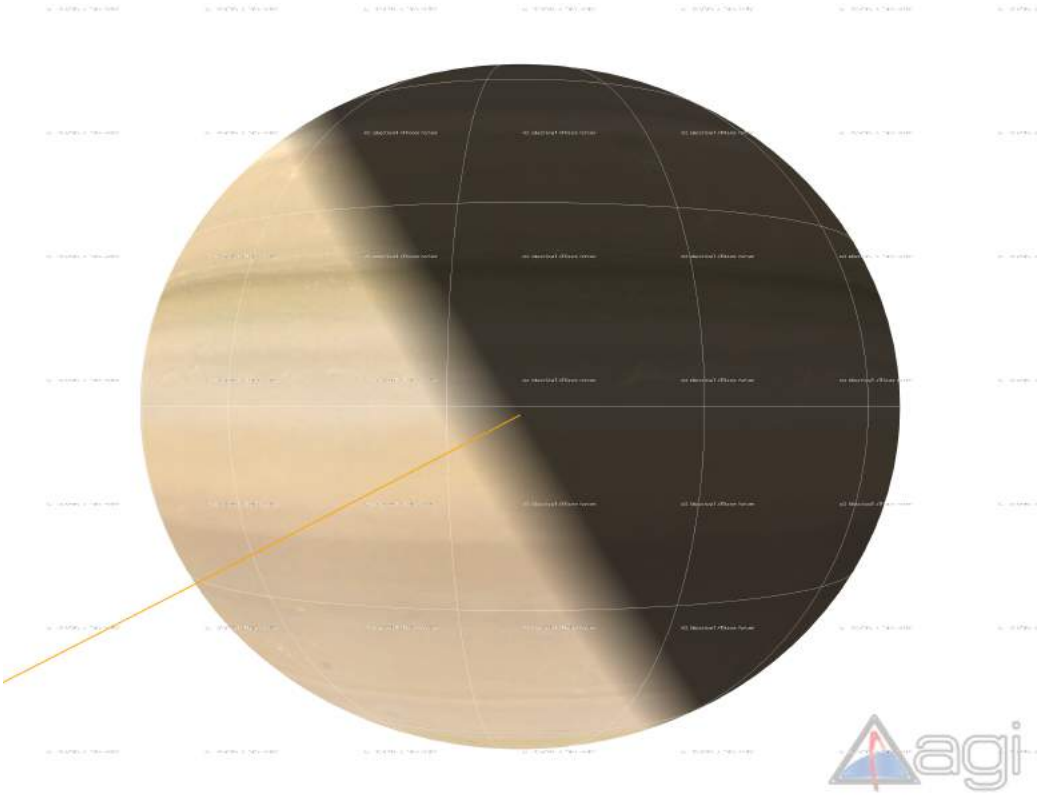

Figure 5.2: The Saturn probe approaches and enters the atmosphere before crossing the ring-plane.

5.1.2 Saturn Encounter

Approximately 130 days before reaching Saturn's atmosphere, the Saturn probe separates from the main orbiter. After separation, the orbiter performs a deflection maneuver to adjust its flyby at Saturn in order to target an encounter at Uranus. As shown in Figure 5.3, there is a clear line-of-sight between the probe and the orbiter throughout the entire probe EDL. Additionally, the orbiter is always visible from Earth during the Saturn encounter. This allows the orbiter to focus its HGA on the probe while using its MGA to relay the probe's data to Earth.

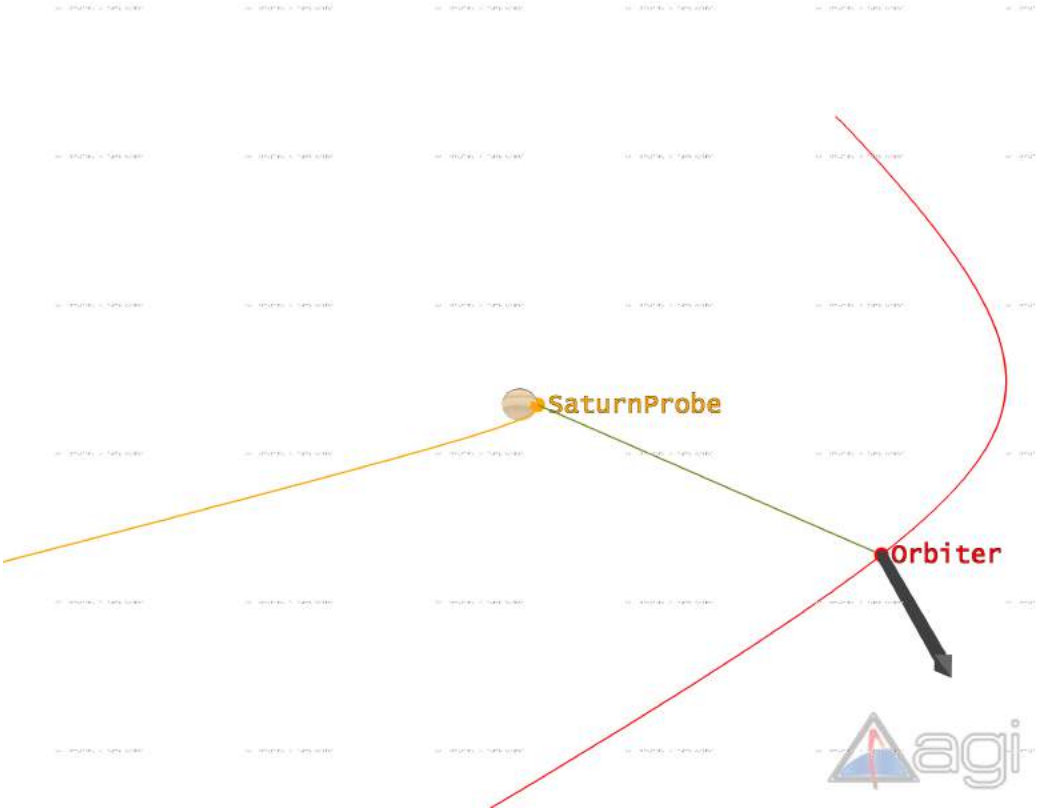

Figure 5.3: Probe-orbiter access and Earth-orbiter access at the start of Saturn EDL.

Table 5.2: Properties of Saturn probe entry and orbiter flyby

Parameter	Value
Flyby Radius	1,120,000 km
Flyby Date	Jan 14, 2032
Probe-Orbiter Distance at Start of EDL	1,618,000 km
Probe-Orbiter Distance at End of EDL	1,556,000 km
Probe Entry Flight Path Angle	-11.4 deg
Probe Entry Velocity	36.296 km/s
Probe Entry Inclination	27.455 deg
Probe Entry Latitude	-0.926 deg
Orbiter DM ΔV	157.8 m/s

The deflection maneuver at Saturn must target suitable entry conditions at Uranus with the added constraint of a near-polar inclination relative to Uranus's equatorial plane in order to simplify the transition to a polar science orbit.

As with the Saturn encounter, there is a possibility of crossing the ring-plane of Uranus before the start of atmospheric entry. However, such a crossing cannot be

prevented by modifying the entry flight path angle alone, because the required angle results in higher atmospheric heating rates than the probe thermal protection system can safely manage. Instead, a combination of steeper entry flight path angle and a slightly lower inclination was used to ensure that the ring-plane is not crossed before atmospheric entry begins. Figure 5.4 depicts the probe's approach to Uranus.

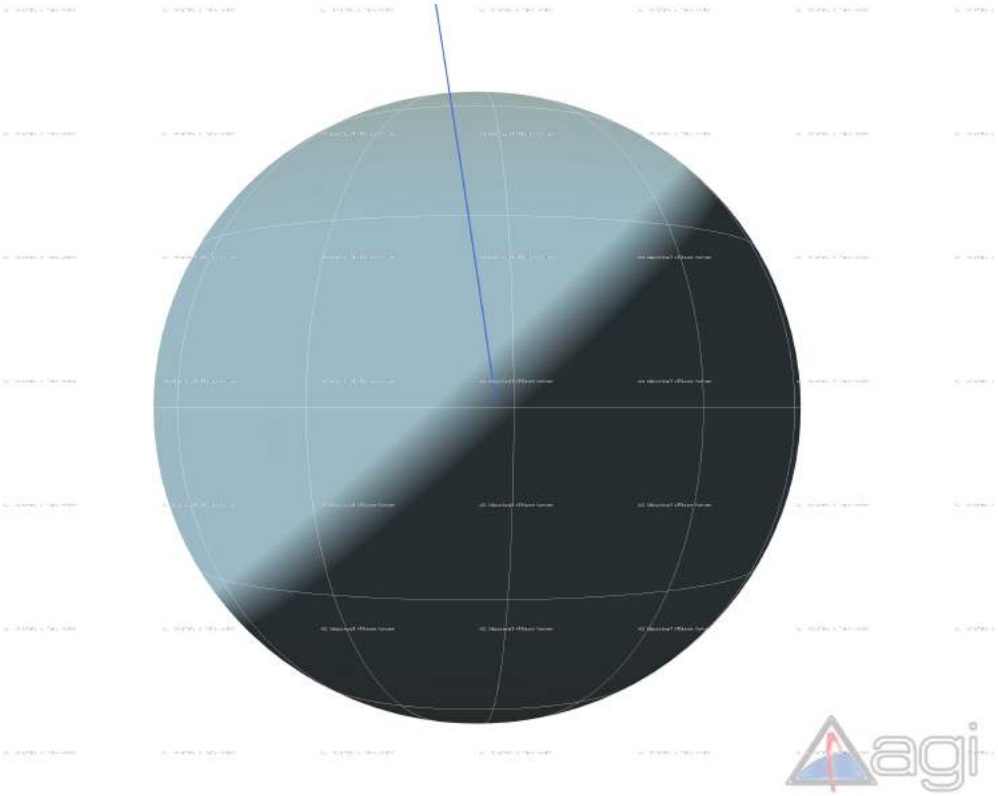

Figure 5.4: The Uranus probe approaches and enters the atmosphere before crossing the ring-plane.

5.1.3 Uranus Encounter

130 days before reaching the atmosphere at Uranus, the orbiter releases the Uranus atmospheric probe and performs a deflection maneuver to prepare for insertion into its final science orbit. This maneuver targets a specific Uranus periapsis, and therefore has a very low ΔV requirement as only small orbital adjustments are needed. In order to avoid colliding with the rings, the orbiter radius of periapsis is set to approximately two Uranus radii.

Figure 5.5 shows the probe-orbiter access at the start of Uranus probe EDL and three hours later. Throughout the entire EDL sequence, the probe always has line-of-sight with the orbiter, which always has line-of-sight with Earth. Despite a planned probe lifetime of approximately two and a half hours, line-of-sight can be maintained for a

maximum time of just under four hours, at which point the orbiter must reorient to prepare for orbital insertion.

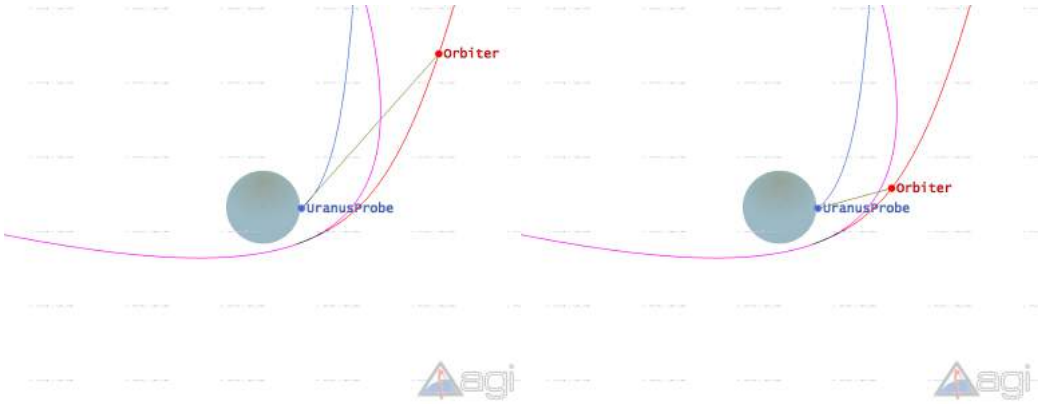

Figure 5.5: View of Uranus approach at the start of probe EDL and three hours later, as seen from Earth.

Table 5.3: Properties of Uranus probe entry and orbiter approach

Parameter	Value
Probe-Orbiter Distance at Start of EDL	155,000 km
Probe Entry Flight Path Angle	-31.5 deg
Probe Entry Velocity	21.47 km/s
Probe Entry Inclination	80 deg
Probe Entry Latitude	0.91 deg
Orbiter DM ΔV	7.15 m/s

5.1.4 Uranus Science Orbit

After the Uranus atmospheric probe ceases communications and the orbiter stops probe tracking, preparations are made for Uranus orbital insertion, which is the largest single maneuver in the mission. The burn is centered about the periapsis of the orbiter's Uranus orbit, and targets an orbital period of 20 days. Both the insertion maneuver and the science orbit are visible from Earth for the entire lifetime of the orbiter. The science orbit is pictured as it would appear from Earth in Figure 5.6. Parameters for the science orbit are summarized in Table 5.4.

Figure 5.6: Science orbit as seen from Earth.

Table 5.4: Science orbit properties

Parameter	Value
Periapsis Radius	52,000 km
Orbital Period	20 days
Eccentricity	0.9317
Inclination	81.15 deg
RAAN	253.5 deg
Argument of Periapsis	223.7 deg

Since there are several constraints on the science orbit, such as radius of periapsis and inclination, it is important to analyze how perturbations affect these parameters. The observed orbital perturbations include effects from third bodies and effects from Uranus's oblateness. The perturbations are shown in Figures 5.7 and 5.8.

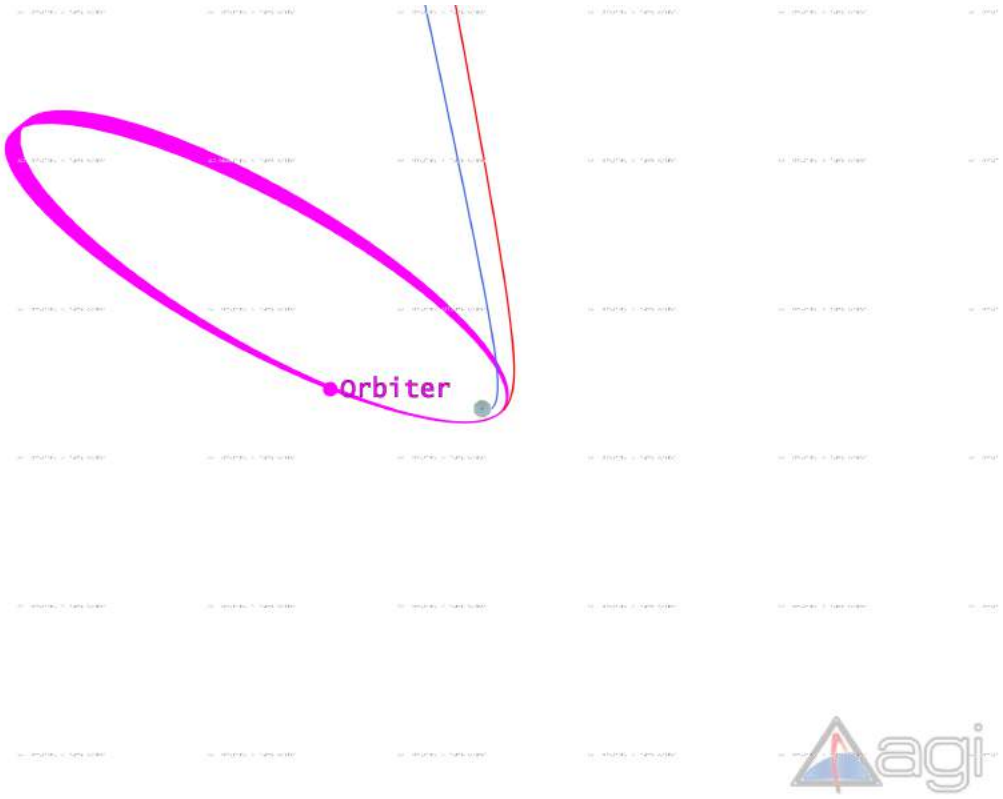

Figure 5.7: Science orbit perturbations over three years as seen from Earth.

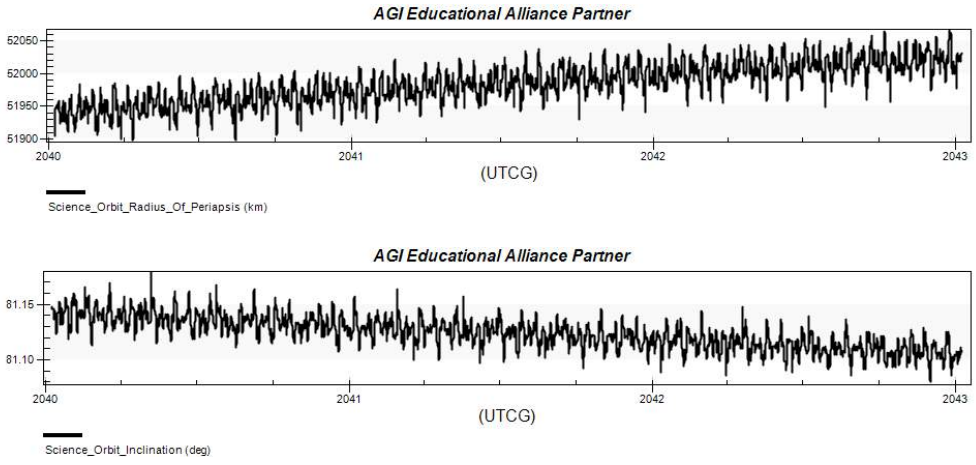

Figure 5.8a: Effect of orbital perturbations on the science orbit over the course of three years.

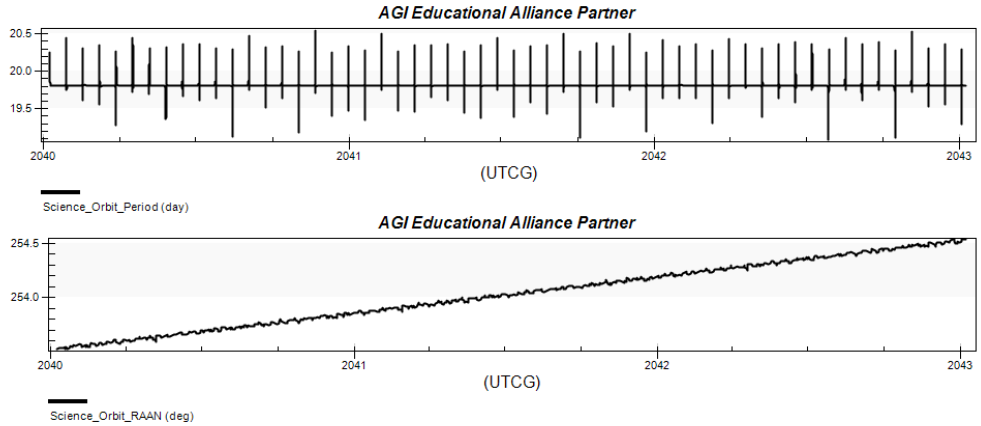

Figure 5.8b: Effect of orbital perturbations on science orbit over the course of three years.

The main science phase is planned to last approximately two years, but variations in the science orbit are analyzed for three years in order to account for possible mission extensions. As indicated by Figure 5.8, the effects of orbital perturbations on the significant orbital elements are negligible. The single largest effect is on the right ascension of the ascending node, which increases by approximately one degree over the course of three years. All of the other orbital elements remain relatively stable throughout the mission.

5.1.5 Uranus Satellite Polar Tour (Optional)

Once the main science tour is completed, the orbiter will embark on an optional polar tour of the moons of Uranus. Specifically, flybys of Ariel, Umbriel, Titania, Oberon, and Miranda will be targeted. Due to the time constraints, a full polar tour design was beyond the scope of this study. However, several studies have already been conducted on the design of such a tour. This study will assume a tour characteristically similar to that described by a study published by the Johns Hopkins Applied Physics Laboratory (McAdams et al., 2011). This tour is shown in Figure 5.9.

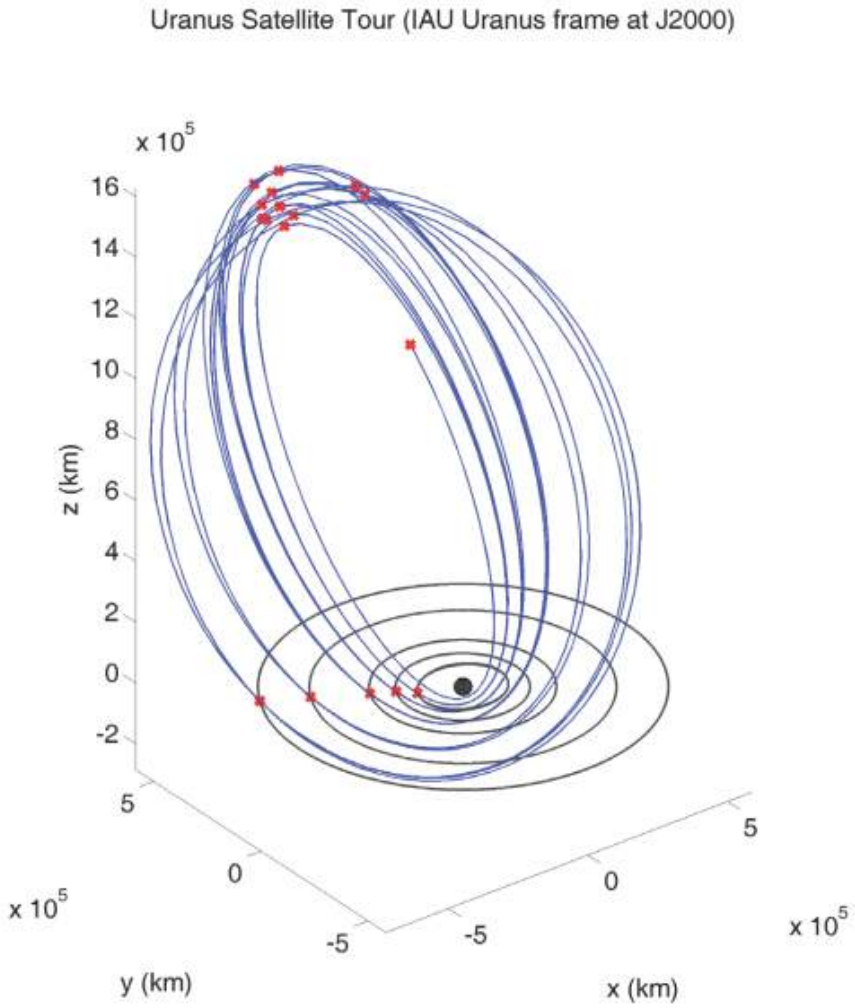

Figure 5.9: Sample polar tour (from McAdams, 2011).

An ideal polar tour would schedule at least two close flybys to each of Uranus's five major moons. The most effective way to accomplish such a tour is to target orbital resonances between the orbiter and each of the moons. This method would minimize the ΔV required to conduct the polar tour while increasing the mission lifetime. Since a satellite tour would be scalable by the number of flybys performed, a trade study can be conducted between the science return and the mission lifetime extension.

For the purpose of this study, it is assumed that a satellite polar tour begins after the main science phase, and required a ΔV on the order of ~600-700 m/s.

5.2 Entry Probe Operations

5.2.1 Saturn Entry

Despite near equatorial latitude and an inclination closely aligned with the planet's fast rotation, the atmospheric entry at Saturn is physically the most extreme phase of the OCEANUS mission. Some 130 days after deployment from the orbiter, the Saturn probe begins entry with an atmospheric-relative speed of 28.46 km/s and an altitude of 1200 km above the level of 1 bar atmospheric pressure. The probe quickly progresses through the phases of peak heating and peak deceleration. During peak heating, the vehicle experiences nearly 7000 W/cm^2. Just before the 12-minute mark, the pilot chute is deployed to stabilize the vehicle and remove the protective back shell. Seconds later, the front half of the aeroshell is ejected and main chute deployed. The probe then begins the science phase of its mission, taking data and relaying it to the orbiter as it descends towards a target depth of 10 bars pressure. Though the probe's batteries are designed to power the module for up to 2.5 hours, communication is likely to be lost between 1 and 2 hours after parachute deployment due to atmospheric attenuation. Figure 5.10 shows the major events involved in the entry and descent of the Saturn atmospheric probe.

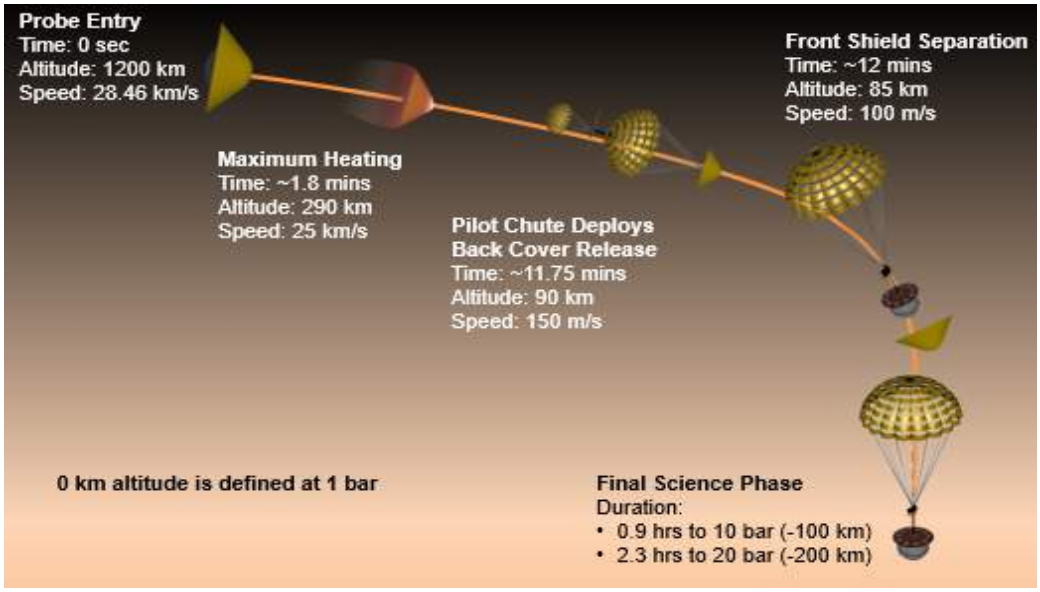

Figure 5.10: Saturn Entry Probe Operations Timeline

5.2.2 Uranus Entry

The concept of operations for OCEANUS' Uranus probe is similar to the Saturn one. Entering at an atmospheric-relative speed of 19.8 km/s, the probe undergoes peak heating at about 1.4 minutes into the trajectory. At 2000 W/cm^2, the peak heating rate is much lower than for the Saturn probe. At approximately 2.5 minutes into the entry, the

pilot chute is released and the back shell removed. At this point, the patch antenna on the probe is revealed, and the probe can send back engineering data collected during the entry. Soon afterwards, the front shell is ejected, and the science instruments start collecting data on the atmosphere. The probe continues to transmit back data to the orbiter until it reaches an altitude between the 10 bar and 20 bar pressure mark. This occurs at approximately 1.5 to 2.5 hours after entry. Figure 5.11 illustrates the major events involved in the entry and descent of the Uranus probe.

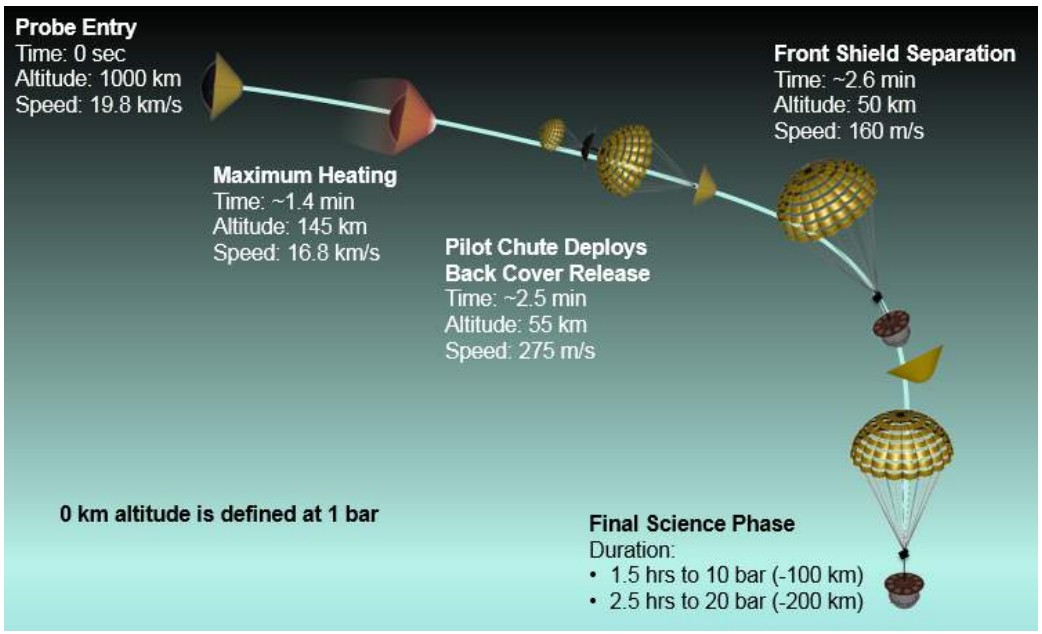

Figure 5.11: Uranus Entry Probe Operations Timeline

5.3 Telecommunication Operations

5.3.1 Overview of Orbiter-Earth Communications

Communication is maintained with the OCEANUS orbiter throughout all phases of the mission. Contact with Earth is supported by the Deep Space Network (DSN), which operates arrays of 34-m and 70-m antennas at locations in Spain, Australia, and the United States. Figure 5.12 illustrates the general concept of operations for the communications. The communication between the orbiter and the DSN can be decomposed into phases. The phases in order are: Early Operations/Instrument Commissioning (up to the first 16 weeks of the mission), Hibernation Cruise, Probe release, Probe entering Saturn, Instruments warm-up Orbiter, Saturn Flyby - Orbiter Science, Hibernation Cruise, Probe release, Probe entering Uranus, Instruments warm-up, Orbiter Uranus Insertion- Orbiter Science, Science orbits, and Science Flybys.

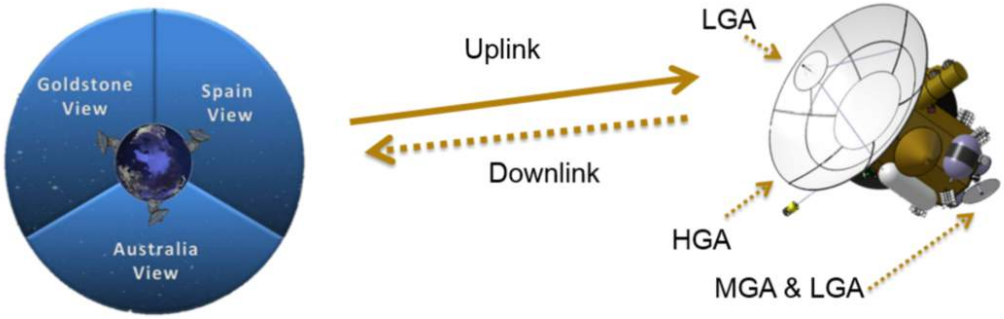

Figure 5.12: Illustration of orbiter telecommunications with the Deep Space Network.

The mission phases requiring instrument calibrations and orbiter check-outs are the early operations/instrument commissioning phase and the orbiter instruments warm-ups, for which the downlink data rate is expected to be similar to *Cassini* (Taylor et al., 2002). In the case of a less demanding communications period, such as hibernation cruise, or probe release, we would require less data to be transmitted to the orbiter or downlinked to Earth. Therefore, the data rates can be estimated to be 40 bps for the downlink. For the uplink, we can expect 500 bps in case of the probe release but only 62.5 bps during the hibernation cruise. These values are also similar to *Cassini*. Commands are uplinked via a combination of X-band and Ka-band depending on the receiving antenna.

Communication for the instrument check-out phase and hibernation phase will be performed using X-band at 8.4GHz for the uplink and 7.2GHz for the downlink. Nevertheless, the orbiter instruments' data volume is high, reaching 5400 Mbits every 20-day orbit. This requires a 34 kbps downlink rate when assuming an 8-hours contact interval each day to ensure copies of science data can be sent back to Earth every orbit. The uplink communication during science operations will only need to average around 500 bps, in order to send confirmation to the orbiter that the data has been well received. In order to communicate the instruments' data rapidly, a Ka-band frequency of 32GHz will be considered for the orbiter downlink to Earth.

5.3.2 Overview of Orbiter-Probe Communications

During entry of the Saturn and Uranus atmospheric probes, the OCEANUS orbiter maneuvers to point its 4 m HGA at the entry site. Science experiments onboard the probes generate an average data rate of 156 bps, but the link is designed to handle up to 200 bps. Reception of this data is highly constrained by atmospheric attenuation and this challenge is exacerbated by the large orbiter-probe distance at Saturn. S-band, X-band, and Ka-band frequencies rapidly weaken with depth, with S-band communications suffering as much as –200 dB by 10 bars (Spilker, 2007). UHF frequencies are not as heavily affected. The probes therefore transmit to the orbiter at an UHF frequency of 405 MHz. Nevertheless, a communication link for probe depths below 10 bars may become challenging and contact with both the Saturn and Uranus probes is expected to be lost before they reach a depth of 20 bars.

Probe data received by orbiter is relayed to Earth in real-time over the X-band using OCEANUS' MGA. Thus, there is no need to reorient the orbiter and transmit the entirely of the probe's data set to Earth over the HGA. This is especially important in the case of the Uranus entry probe, since there is only a narrow interval of only 1-1.5 hours between the end of the probe's mission and the beginning of the orbit insertion maneuver. Note that orbiter-probe communications are primarily one-way, as no commands are transmitted to the atmospheric probes once they have begun EDL. Figure 5.13 illustrates the set-up of the probe data relay.

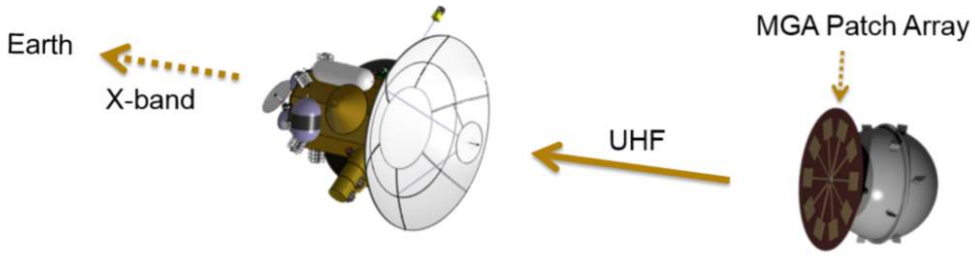

Figure 5.13: Entry Probe Data Relay

5.3.3 Communications Summary

Table 5.5 provides a summary of the telecommunication operations for all phases of the mission. Link-budget analyses and the design control tables for each data downlink are presented in Appendix F.

Table 5.5: OCEANUS telecommunication operations by mission phase

Downlink Info	Early Ops and Commissioning	Cruise	Probe Release/ Cruise	Saturn Probe Entry	Instrument Warm-up	Saturn Approach Science	Cruise	Probe Release/ Cruise	Instrument Warm-up	Uranus Approach Science	Uranus Probe Entry	Science Operations	Satellite Flybys
Length of Phase	16 weeks	143 weeks	21 weeks	0 weeks	0 weeks	0 weeks	400 weeks	21 weeks	0 weeks	0 weeks	0 weeks	104 weeks	0 weeks
Downlink Band	X/Ka-band	X-band	X-band	UHF/X-band	X-band	Ka-band	X-band	X-band	X-band	Ka-band	UHF/X-band	Ka-band	Ka-band
Downlink Freq.	8.4GHz/32GHz	8.4GHz	8.4GHz	405MHz/ 8.4GHz	8.4GHz	32GHz	8.4GHz	8.4GHz	8.4GHz	32GHz	405MHz/ 8.4GHz	32GHz	32GHz
Telemetry Data Rate	948 bps	40 bps	40 bps	200 bps	948 bps	34 kbps	40 bps	40 bps	948 bps	34 kbps	200 bps	34 kbps	34 kps
Transmitting Antenna	LGA	MGA	MGA	Patch array/MGA	MGA	HGA	MGA	MGA	MGA	HGA	Patch array/MGA	HGA	HGA
Transmitter DC Power	116 W	116 W	116 W	116 W	116 W	100 W	116 W	116 W	116 W	100 W	116 W	100 W	100 W
Receiving Antenna	DSN 34-m	DSN 34-m	DSN 34-m	HGA/ DSN 34-m	DSN 34-m	DSN 34-m	DSN 34-m	DSN 34-m	DSN 34-m	DSN 34-m	HGA/ DSN 34-m	DSN 34-m	DSN 34-m
Receiver Gain	68.23/79.83 dBi	68.23 dBi	68.23 dBi	22.37/ 68.23 dBi	68.23 dBi	79.83 dBi	68.23 dBi	68.23 dBi	68.23 dBi	79.83 dBi	22.37/ 68.23 dBi	79.83 dBi	79.83 dBi
Transmitter RF Output	60 W	60 W	60 W	10.7/60 W	60 W	40 W	60 W	60 W	60 W	40 W	10.7/60 W	40 W	40 W
Daily Data Returned	81.9 Mbit	3.5 Mbit	3.5 Mbit	842 kbit	81.9 Mbit	979 Mbit	3.5 Mbit	3.5 Mbit	81.9 Mbit	5000 Mbit	842 kbit	979 Mbit	979 Mbit
Uplink Info	**Early Ops and Commissioning**	**Cruise**	**Probe Release**	**Saturn Probe Entry**	**Instrument Warm-up**	**Saturn Orbiter Science**	**Cruise**	**Probe Release**	**Instrument Warm-up**	**Uranus Approach Science**	**Uranus Probe Entry**	**Science Operations**	**Satellite Flybys**
Uplinks per Day	3	1 per month	1	3	3	3	1 per month	1	3	1	3	1	1
Uplink Band	X-band	X-band	X-band	X-band	X-band	Ka-band	X-band	X-band	X-band	Ka-band	X-band	Ka-band	Ka-band
Uplink Freq.	7.2 GHz	7.2 GHz	7.2 GHz	7.2 GHz	7.2 GHz	32 GHz	7.2 GHz	7.2 GHz	7.2 GHz	32 GHz	7.2 GHz	32 GHz	32 GHz
Telecommand Data Rate	500 bps	62.5 bps	500 bps	500 bps	500 bps	500 bps	62.5 bps	500 bps	500 bps	500 bps	500 bps	500 bps	500 bps
Receiving Antenna	LGA	MGA	MGA	MGA	MGA	HGA	MGA	MGA	MGA	HGA	MGA	HGA	HGA
Receiver Gain	11.45 dBi	32.83 dBi	32.83 dBi	32.83 dBi	32.83 dBi	60.33 dBi	32.83 dBi	32.83 dBi	32.83 dBi	60.33 dBi	32.83 dBi	60.33 dBi	60.33 dBi

5.4 End-of-Life Operations

The OCEANUS concept is designed to allow for one or more mission extensions or enhancements (such as a satellite tour). However, the declining power output of the orbiter's five eMMRTGs will eventually prevent further operations. Before this occurs, the orbiter may engage in an end-of-life program to dispose the spacecraft in Uranus' atmosphere in the interests of planetary protection.

Uranus and its satellites are considered category II bodies in terms of the level of planetary protection that is mandated by the Committee on Space Research. This means that they are of interest to understanding the chemical origins and evolution of life but there is little to no chance of contamination compromising future investigations. The entry probes delivered to Saturn and Uranus are certain to be completely vaporized several hours after their batteries deplete as they continue descend into deep atmosphere of these planets. They are therefore of little consequence to planetary protection. The OCEANUS orbiter, on the other hand, could potentially collide with one of Uranus' satellites or rings many years after operations have ceased. To preclude this possibility, a small propulsive burn or series of burns will be made near the end of the mission to lower the science orbit periapsis to a critical altitude where atmospheric drag will slowly de-orbit the spacecraft.

A lowered science orbit periapsis also provides opportunities for additional science investigations. The primary reason for the selection of an initial periapse radius of 2.05 R_U was to prevent the spacecraft from passing between Uranus and its rings and therefore being at the risk of colliding with possible debris. However, this distance makes studies of Uranus' interior through orbit perturbations difficult. Near the end of the OCEANUS mission, when many studies of the rings have been performed, the risks of crossing Uranus' ring-plane are likely to be better understood. Furthermore, the slow orbital decay caused by a low periapse may also allow for *in situ* studies of the neutral portion of Uranus' upper atmosphere.

6 Mission Risk Assessment

6.1 Risk Analysis

The study narrowed down the identified risks for the mission concept to the top 12 major risks items. They mostly comprised of cost and technical risks. Table 6.1 identifies these risks along with their likelihood (L), consequence (C), and summarized mitigation strategies. Figure 6.1 presents a 5×5 risk matrix for the top 12 risks after the risk mitigation strategies have been applied. Appendix G provides a detailed account of the risk study for this mission concept.

Table 6.1: OCEANUS major risk items and mitigation strategies.

No.	Risk Source	Category	L	C	Mitigation Strategy
1	Cost overruns due to delay	Cost – Design and Evaluation	3	3	Descope updated instruments in favor of heritage instruments when necessary
2	Probe lost before 1 bar	Technical - Entry, Descent & Landing	2	4	Monte-carlo simulation of different entry conditions & atmospheric conditions
3	Probe communication lost before H20 clouds	Technical - Telecommunications	5	1	Complimentary imaging from orbiter
4	Probe deployment failure	Technical - Mechanical Systems	1	3	Extensive testing Cassini-Huygens heritage
5	Engine cover mechanism failure	Technical - Mechanical Systems	1	4	Make cover detachable in the case of retraction failure
6	Increased operational risk due to multiple probes	Cost - Mission Design	2	2	Pioneer Venus heritage Pre mission cost estimation
7	Availability of HEEET for the probes	Cost - Entry, Descent & Landing	1	3	Increase funding and continue research and development of HEEET
8	Probe lost before 10 bars	Technical - Telecommunications	2	3	Complimentary imaging from orbiter
9	Parachute failure during final descent	Technical - Entry, Descent & Landing	1	3	Extensive testing Heritage stowing and deployment
10	Main engine failure	Technical - Propulsion	1	3	Contingency engine
11	Patch antenna development delays	Cost - Telecommunications	1	5	Increase development efforts into patch antennas
12	HGA failure	Technical - Telecommunications	1	4	Testing, heritage, and MGA as back-up

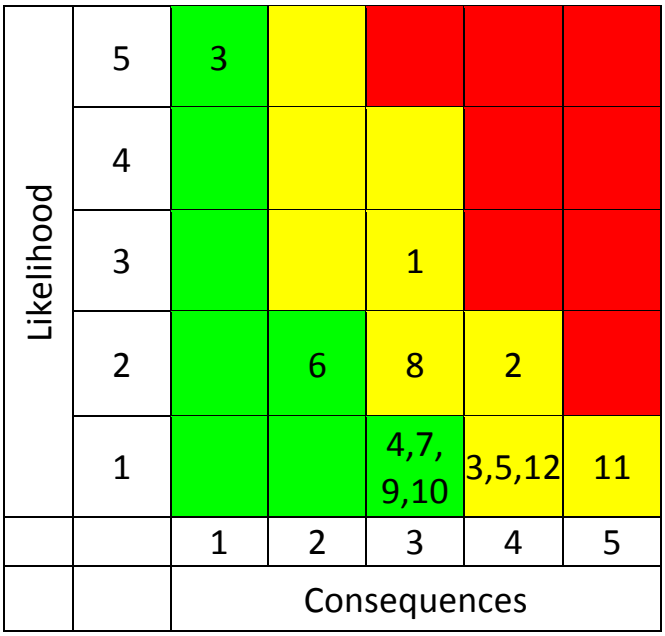

Figure 6.1: Risk matrix of top 12 risk items listed.

7 Mission Life-Cycle Cost

7.1 Overview

This study carried out mission concept life-cycle cost estimation at Work Breakdown Structure (WBS) Level 2. Given that there were limited resources available at the time of point design, the estimation relied on an analogy-based method which was validated by actual flown mission data and NASA's cost software Project Cost Estimating Capability (PCEC).

7.2 Ground Rules and Assumptions

- Cost estimation performed at WBS Level 2 specified in Revision D of NPR 7120.5 only.
- Reported cost estimation is based on Fiscal Year 2015 (FY15) dollars. Reference cost data used to make the analogy model also converted to FY15 dollars.
- The cost estimation is not broken down in a year-wise or phase-wise manner. It only provides overall cost for each element of the WBS Level 2.
- Launch cost (WBS 07) was not included in the total cost estimation since Space Launch System (SLS) is going to be used for the mission.
- Reserve calculated to be 30 % of the entire subtotal cost including Phase A-D and Phase E-F, excluding launch cost.

7.3 Approach

7.3.1 Analogy Model Development

At the time of designing the mission concepts, there were no publicly available tools to accurately estimate the entire mission cost, including operation cost. NASA's PCEC- the only cost estimating software open to the public - cannot compute certain WBS Level 2 elements such as mission operations. Thus, to estimate the entire mission cost, an analogy-based cost estimator model was developed. This model can provide an estimate of the subtotal cost (without launch service fee and reserve), and a cost breakdown at the WBS Level 2 for the subtotal when the following mission design variables are provided:

- Total launch cost (kg)
- Usable orbiter mass w/o contingency (kg)
- Probe mass w/o contingency (kg)
- Instrument mass w/o contingency (kg)
- Length of Phase A-D (years)
- Length of Phase E-F (years)
- SEP usage (0: no, 1: yes)

The data from past Planetary Science Decadal Survey studies were used to build an analogy based cost predictor model for project OCEANUS. The decadal studies used high-fidelity cost analyses by quasi-grassroots methods and parametric models for their own cost estimations. 22 mission concept studies were collected from 14 Decadal Survey proposals listed by Space Studies Board as used as input data for the analogy model. The mission design variables, subtotal cost without launch service (WBS 07.0) and cost breakdown for each element of the WBS Level 2 (including Education/Public Outreach and DSN service fee) were gathered and various regressions were carried out on those data.

7.3.2 Analogy Model Selection – Neural Network Regression

A total of 7 different regression methods were assessed for best fit to the cost estimation data from the decadal study reports.

- Linear Regression by Least Squares
- Linear Regression by Support Vector Machine (SVM)
- Non-Linear Regression by Support Vector Machine (SVM)
- Gaussian Process Regression (Kriging)
- Ensemble Regression Tree by LSBoost
- Ensemble Regression Tree by Bagging
- Neural Network Regression (NNR)

To implement these regression methods, MATLAB® 2016a Statistics and Machine Learning Toolbox™ and Neural Network Toolbox™ were used. Validation of the cost predictor was based on comparing its output to the total cost of four actual flown missions - *Cassini-Huygens*, *Galileo*, *Dawn*, and *Juno*. First, the mean squared error against the total cost of those missions was computed. Then, the ratio of its root to the average of the total cost was used as a performance metric. (Note that total cost here doesn't also include launch cost.) Table 7.1 shows the results of the validation step.

$$Total\ Cost\ Estimation\ Error = \frac{\sqrt{Mean\ Squared\ Error\ against\ Total\ Cost}}{Average\ Total\ Cost}\ (\%)$$

Table 7.1: Comparison of prediction error in the different regression models for analogy-based cost estimation.

Regression Models	Total Cost Estimation Error (%)
Linear Regression (Least Squares)	65.7
Linear Regression (SVM)	68.2
Non-Linear Regression (SVM)	71.7
Gaussian Process Regression (Kriging)	72.1
Ensemble Regression Tree (LSBoost)	63.3
Ensemble Regression Tree (Bagging)	66.5
Neural Network Regression (NNR)	**4.1**

Among the 7 different regression models, Neural Network Regression (NNR) was the most capable of estimating the total cost, of the mission, with the least total estimation error of 4.1 %.

The neural network process is a sort of feedback control. Initial weights w_i for each input x_i are assigned and predicted output $\hat{y}_j$ is computed by introducing them into output functions. The difference between the output $\hat{y}_j$ and actual target output y_j is used as a basis for deciding how the weights change for the next step. This is a common dogma of supervised machine learning methods. What makes Neural Network unique among other methods is that it contains one more additional buffer stage called "hidden layer" between input and output. Inputs are multiplied by weights and fed into each element of this hidden layer, and each of them creates output h_k which combines all the inputs and weights. These tentative outputs are again combined with different weights w'_k and used as arguments of an output function to produce the predicted output $\hat{y}_j$. Usually, Logistic function is used to link inputs with hidden layer output h_k, and a simple linear combination of h_k is used to construct the final output $\hat{y}_j$. These functions are called *transfer functions*. Neural Network fits non-linear function data into a linear combination of inputs. By changing the number of elements of the hidden layer, transfer functions, and a learning algorithm, Neural Network can be applicable to a wide variety of data sets.

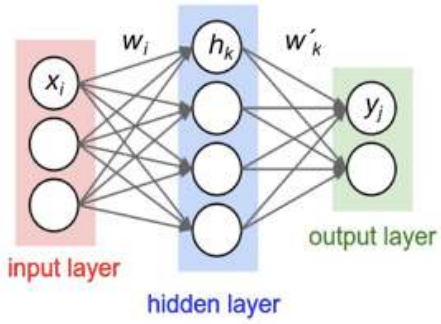

$$h_k(\boldsymbol{x}) = \frac{2}{1 + \exp\left(-2\sum w_i x_i\right)} - 1 \; (-1 \leq h_k(\boldsymbol{x}) \leq 1)$$

$$y_j(\boldsymbol{x}) = \sum w'_k h_k(\boldsymbol{x})$$

Figure 7.1: Graphical representation of a Neural Network. The input layer corresponds to the input variables to be used for predicting the values of outputs coming from the output layer (Karpathy, 2016).

In addition to the total mission cost, excluding the launch cost, the NNR model developed in this project estimates the cost breakdown of the mission cost at the WBS

Level 2. The cost breakdown estimation was validated by NASA's Project Cost Estimating Capability (PCEC).

7.3.3 Analogy Model Validation by PCEC

The PCEC software (General Public Release License) contains a library of NASA cost estimating relationship (CER) and a framework to estimate the project cost based on it. This software is an add-in for Microsoft Excel® and provides a user with an interactive user interface (Figure 7.2). It computes cost breakdown at the WBS Level 2 (for some elements, Level 3 in detail) when provided with user inputs - a mission profile, schedule and spacecraft subsystems. The PCEC cannot compute any cost breakdown in a year-wise or phase-wise manner, which means that the PCEC alone cannot provide total cost estimation compatible with the Ground Rules specified in the Planetary Science Decadal Survey guideline. Nevertheless, since the PCEC predicts cost based on parametric models developed from the library of CER, its estimation for the cost of some WBS Level 2 elements can be used to validate the cost breakdown estimation performed by the NNR model.

Robotic Spacecraft

FY2015 $M

WBS #	Level	WBS Element	Non-Recurring	D&D	STH	Flt Unit	Recurring Production	Non-Allocated	Total
0	1	System Name	$ 73.42				$ 62.59	$ 632.60	$ 768.61
1.0	2	Project Management						$ 48.62	$ 48.62
2.0	2	Systems Engineering						$ 113.48	$ 113.48
3.0	2	Safety and Mission Assurance						$ 60.93	$ 60.93
4.0	2	Science/Technology						$ -	$ -
5.0	2	Payload(s)	$ -	$ -	$ -	$ -	$ -	$ 72.31	$ 72.31
5.01	3	Payload Management						$ 10.29	$ 10.29
5.02	3	Payload System Engineering						$ 24.02	$ 24.02
5.03	3	Payload Product Assurance						$ 12.89	$ 12.89
5.10	3	Instruments - EMPTY ROLLUP							$ -
5.x	3	Payload I&T						$ 25.11	$ 25.11
6.0	2	Flight System \ Spacecraft	$ 73.42	$ -	$ -	$ -	$ 62.59	$ 250.78	$ 386.79
6.01	3	Flight System Project Management						$ 26.84	$ 26.84
6.02	3	Flight System Systems Engineering						$ 62.64	$ 62.64
6.03	3	Flight System Product Assurance						$ 33.63	$ 33.63
6.10	3	Spacecraft	$ 73.42	$ -	$ -	$ -	$ 62.59	$ 127.66	$ 263.67
	4	Spacecraft Management						$ -	$ -
	4	Spacecraft Systems Engineering						$ -	$ -
	4	Spacecraft Product Assurance						$ -	$ -
	4	Structures & Mechanisms	$ 7.40	$ -	$ -	$ -	$ 4.33	$ -	$ 11.73
	4	Thermal Control	$ 2.53	$ -	$ -	$ -	$ 6.11	$ -	$ 8.64
	4	Electrical Power & Distribution	$ 6.79	$ -	$ -	$ -	$ 9.12	$ -	$ 15.91
	4	GN&C	$ 10.22	$ -	$ -	$ -	$ 23.13	$ -	$ 33.34
	4	Propulsion	$ 1.10	$ -	$ -	$ -	$ 7.68	$ -	$ 8.79
	4	Communications	$ 40.61	$ -	$ -	$ -	$ -	$ -	$ 40.61
	4	C&DH	$ 4.76	$ -	$ -	$ -	$ 12.23	$ -	$ 16.99
	4	Spacecraft Software							$ -
6.x	4	Spacecraft I&T						$ 127.66	$ 127.66
7.0	2	Ground Data System (GDS)						$ -	$ -
8.0	2	Launch Vehicle/Services							$ -
9.0	2	Mission Operations System (MOS)							$ -
10.0	2	System Integration, Assembly, Test & Check Out						$ 81.90	$ 81.90
11.0	2	Education & Public Outreach						$ 4.59	$ 4.59

Figure 7.2: Screenshot of a Microsoft Excel® spread sheet of the PCEC user interface. The sheet displayed here is a WBS sheet which summarizes a result of cost estimation based on user's inputs. This estimation doesn't include WBS 4.0, 7.0 – 9.0 and DSN service portions.

The validation of the NNR model by the PCEC was carried out in a similar manner to the evaluation of regression models described earlier. The absolute value of the error between the estimates by the NNR and by the PCEC is divided by the value of the PCEC's estimate to give the deviation in percentage. The result of the validation is summarized in Table 7.2.

$$Deviation = \frac{|PCEC's\ estimate - NNR's\ estimate|}{Value\ of\ PCEC's\ estimate}\ (\%)$$

Table 7.2: Validation of the NNR by the PCEC. Since the PCEC can only give estimates of WBS 1.0-3.0, 5.0-6.0, and 9.0-10.0 elements, the subtotal in this table includes only these elements. Note: the NNR can provide estimates for other elements, but they are not included here.

WBS Level 2 Elements	PCEC (FY15M$)	NNR (FY15M$)	Deviation (%)
1.0 Project Management	48.62	35.2	27.6
2.0 Systems Engineering	113.48	32.1	71.7
3.0 Safety & Mission Assurance	60.93	33.2	45.5
5.0 Payloads	81.75	408.4	399.6
6.0 Flight System (Orbiter)	386.79	322.4	16.6
6.0 Flight System (Probe)	147.68	147.0	0.5
9.0 System Integration & Test	112.11	68.4	39.0
10.0 Education & Public Outreach	5.76	11.8	104.9
Subtotal	**957.12**	**1058.5**	**10.6**

Deviation from the PCEC's estimate was significant for certain WBS level 2 elements - Systems Engineering (2.0), Payloads (5.0) and Education and Public Outreach (10.0). However, the NNR could provide very close predictions for cost of both orbiter and probe (6.0). The overall estimate of the subtotal cost deviated from PCEC estimation by only 10.6 %. The significant deviations in a certain WBS Level 2 elements could be a result of different methods being used to estimate cost breakdowns in those studies. Though it is still necessary to refine the NNR model to increase the accuracy of estimating cost breakdown at the WBS Level 2, project OCEANUS settled on this model as a current best estimator for the total mission cost.

7.4 Mission Life Cycle Cost Analysis

7.4.1 WBS Level 2 Cost Breakdown of OCEANUS

Estimation of cost breakdown at the WBS Level 2 was carried out by using the NNR analogy model. Cost reserve was assumed to be 30% of the subtotal cost. This assumption might be too optimistic at the stage of CML 4 because most of the Planetary Science Decadal Survey mission proposals estimated the cost reserve to be 50% for Phase A-D and 25% for Phase E-F, thus, around 40% for entire cost. However, since OCEANUS's flight systems are mostly dependent on modified heritage systems, 30% reserve was chosen for OCEANUS. The result of the cost breakdown is shown in Table 7.3.

Table 7.3: Cost breakdown at the WBS Level 2 for the OCEANUS mission concept. The estimated total cost without launch service fee is slightly below the cost cap of $2 billion.

WBS Level 2 Elements	NNR Estimate for OCEANUS (FY15M$)
1.0 Project Management	35.2
2.0 Systems Engineering	32.1
3.0 Safety & Mission Assurance	33.2
4.0 Science & Technology	206.3
5.0 Payloads	408.4
6.0 Flight System (Orbiter)	322.4
6.0 Flight System (Probe)	147.0
7.0 Ground Data System	22.8
8.0 Mission Operations System	165.9
9.0 System Integration & Test	68.4
10.0 Education & Public Outreach	11.8
DSN Service	16.9
Subtotal	**1470.4**
Reserve (30 % of Subtotal)	441.1
Total w/o Launch Service	**1911.5**

The estimation was not conducted in a year-wise or phase-wise manner due to the limitation of the analogy model. The total cost without the launch service fee was estimated to be FY15$1.92 billion, which is less than the $2 billion cost cap specified in the Ground Rules and Assumptions. Additional high-fidelity cost analysis with a bottom-up approach could refine the cost estimation in a later stage of the mission design, to mitigate the risk of cost overruns.

7.4.2 Sensitivity to Development Delay and De-scoping

The developed NNR analogy model can evaluate the impact of individual variable changes and associated risk about life cycle cost. Due to the very complex coupling of the variables in the cost estimation, it is difficult to depict the pure influence of a single variable. The sensitivity of the total cost to the length of Phase A-D was computed and the result is plotted in Figure 7.3. The figure depicts the $2 billion cost cap the current point design of OCEANUS. As can be seen, the total cost would be highly sensitive to the system development time. Cost associated with 7-year development time instead of 6 years for OCEANUS is about $2.07 billion, which is more than the cost cap requirement. This means that the consequence of system development delay would be around $100 million or more than that if it happens. To mitigate the risk of cost overrun, alternative plans with de-scoped mission concepts should be taken into account.

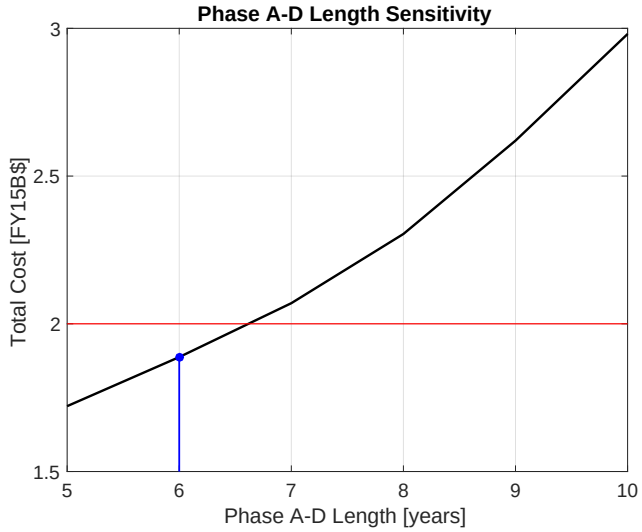

Figure 7.3: Sensitivity of the total cost to the length of Phase A-D. A black line is the resultant sensitivity plot, a red line is the $2 billion cost cap and a blue line is the current point design.

With 7 years for Phase A-D considered, a sensitivity analysis for instrument mass was also conducted (Figure 7.4). The current point design with 7-year development time was estimated to be $2.07 billion. However, the diagram indicates that descoping some instruments to reduce the instrument mass down to below 190 kg would enable the mission cost to stay under the $2 billion cost cap.

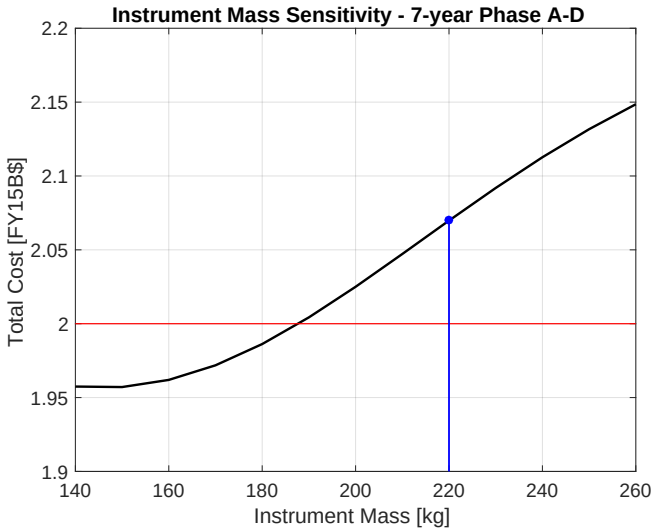

Figure 7.4: Sensitivity of the total cost to mass of instruments when the length of Phase A-D is 7 years. The color code is same as that of Figure 7.3.

To enable the mission under the cost cap, some of the instruments should be de-scoped. One possible candidate would be the OPI instrument. Downgrading it to smaller one such as the Lorri Camera installed on the *New Horizons* mission would save around 30 kg of the instrument mass and lower the total cost below the allowable maximum. Though this de-scoping would limit the science capability of the orbiter, the science objectives including enhanced ones can still be achieved by complementing the observation with other spectroscopic measurements.

7.4.3 Opportunistic Mission Extension

While the length of development time was expected to be very influential on the mission total cost, another sensitivity analysis indicated thatthe length of the mission operation time (Phase E-F) would not be as influential. Figure 7.5 is the result of the sensitivity analysis for the impact of the length of Phase E-F. It can be speculated that the mission can be implemented within the cost cap even with longer mission operation time such as 14 years. This result suggests the possibility of opportunistic extension of the mission. The prolonged mission would enable additional "bonus" operations such as touring of Uranus moons.

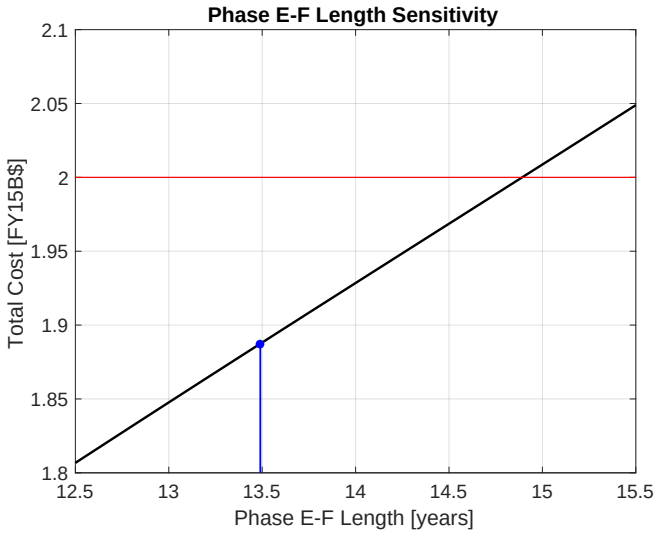

Figure 7.5: Sensitivity of the total cost to the length of Phase E-F. The color code is same as that of Figure 7.3.

7.4.4 Comparison of Life Cycle Cost among Different Concepts

Estimations of life cycle cost were also conducted for other candidate mission concepts which were not chosen as a baseline. Table 7.4 is a summary of mission variables and total cost estimation for those concepts and the baseline concept. It was found out that the selected mission architecture would cost the least among all mission concepts assessed for OCEANUS.

Table 7.4: Cost comparison among different mission concepts for OCEANUS. The chosen baseline concept had the lowest total cost.

Mission Concepts	SLS, Chemical, Impulsive Capture (FY15M$)	SLS, SEP, Impulsive Capture (FY15M$)	SLS, Chemical, Aerocapture (FY15M$)
Total Launch Mass (kg)	3797.9	9010.0	15766.0
Usable Orbiter Mass (kg)	1128	1848	2205
Probe Mass (kg)	297.5	297.5	297.5
Instrument Mass (kg)	220	220	220
Length of Phase A-D (years)	6	6	6
Length of Phase E-F (years)	13.49	10.72	11.11
Total Cost w/o Launch Service in FY15M$ (Reserves Included)	**1911.5**	**2076.5**	**2318.1**

References

3D-Plus, Memory Module SDRAM. Radiation Tolerant Memory. Obtained via web May 2016 from: http://www.3d-plus.com/doc/prod/3dfp_0493_1.pdf

Aerojet Rocketdyne, Aerojet Rocketdyne Bipropellant Rocket Engine Data Sheet. pp. 1-9, 2006a.

Aerojet Rocketdyne, MR-11C 4 N (1.0 Lbf) Rocket Engine Assembly. 2006b. Obtained via web May 2016 from: http://www.rocket.com/files/aerojet/documents/Capabilities/PDFs/Monopropellant%20Data%20Sheets.pdf

Agrawal, P., Allen, G.A., Sklyanskiy, E.B., et al., Atmospheric Entry Studies for Uranus. 2014 IEEE Aerospace Conference, Big Sky, MT, pp. 1-19, 2014, doi: 10.1109/AERO.2014.6836417.

Airbus Defence and Space, Solid State Recorders for Space Applications. Earth Observation, Navigation, and Science, 2014. Obtained via web May 2016 from: http://www.space-airbusds.com/media/document/ens_5_ssr_2014_bd.pdf

Ali-Dib, M., Mousis, O., Petit, J., and Lunine, J. I. , The Measured Compositions of Uranus and Neptune from Their Formation on the CO Ice Line. Astrophys. J. 793, No. 9, 2014, doi:10.1088/0004-637X/793/1/9.

Amore, L.J. and Saylor, W.P. Optical Solar Reflector and Mounting Method. Patent, US5400986 A, 1995.

Antenna Development Corporation, Medium Gain Patch Antennas. Precision Antennas for Spacecraft, Rockets, and Missiles, 2009. Obtained via web My 2016 from: http://www.antdevco.com/ADC-0512271640 R3 4-Patch Array data sheet.pdf

Arnold, J.O., Iaud, B., Chen, Y., Prabhu, D.K., Bittner, M.E., and Venkatapathy, E., Arcjet Testing of Woven Carbon Cloth for Use on Adaptive Deployable Entry Placement Technology. 10th International Planetary Probe Workshop, San Jose, CA, 2013.

Arridge, C. S., Achilleos, N., Agarwal, J., et al., The Science Case for an Orbital Mission to Uranus: Exploring the Origins and Evolution of ice giant Planets. Planet. Space Sci. 104, pp. 122-140, 2014.

Atkinson, D.H., Oudrhiri, K., Spilker, T.R., Baines, K.H., Asmar, S., Bienstock, B., and Sichi, S., Direct-To-Earth Communications For Outer Planetary Entry Probe Missions. Fourth Interplanetary Probe Workshop (IPPW), Pasadena, CA, 2006.

Atreya, S.K. Atmospheres and Ionospheres of the Outer Planets and their Satellites. Springer, pp. 18-105, 1985.

BAE Systems, RAD750® 6U CompactPCI Single-board Computer. RAD750® Family of Products. Obtained via web May 2016 from: http://www.baesystems.com/en/document/space-products-rad750

Balint, T.S. Overview of Mission Architecture Options for Jupiter Deep Entry Probes. Outer Planets Advisory Group Meeting, Boulder, CO, 2005. Web. 28 May 2016.

Ball, A.J., Garry, J., Lorenz, R., and Kerzhanovich, V., Planetary Landers and Entry Probes. Cambridge University Press, New York, NY, 2007.

Bridge, H.S., Belcher, J.W., Coppi, B., et al., Plasma Observations Near Uranus: Initial Results from Voyager 2. Science 233, pp. 89-93,1986.

Broadfoot, A.L., Herbert, F., Holberg, J.B., Ultraviolet Spectrometer Observations of Uranus. Science 233, pp. 74-79, 1986.

Burgdorf, M., Orton, G., Van Cleve, J., Meadows, V., and Houck, J., Detection of new hydrocarbons in Uranus' atmosphere by infrared spectroscopy. Icarus 184, pp. 634– 637, 2006.

Chang, C., Slobin, S.D., Sniffin, R., et al., DSN Telecommunication Link Handbook: Space Link Interface. Jet Propulsion Laboratory, 810-005, 2015.

Cianciolo, A.D., Zang, T.A., Sostaric, R.R., and Mcguire, K.M., Overview of the NASA Entry, Descent and Landing Systems Analysis Exploration Feed-Forward Study. 8th International Planetary Probe Workshop, Portsmouth, VA, 2011.

Clausen, K.C., Hassan, H., Verdant, M., Couzin, P., Huttin, G., Brisson, M., Sollazzo, C., and LeBreton, J.P., The Huygens Probe System Design. Space Science Reviews 104, pp. 155-189, 2002.

Colwell, J.E., The disruption of planetary satellites and the creation of planetary rings. Planet. Space Sci. 42, No. 12, pp. 1139-1149, 1994.

Cornwell, D., Space-Based Laser Communications Break Threshold. Optics & Photonics News, 2016. Obtained via web May 2016 from: http://www.osa-opn.org/home/articles/volume_27/may_2016/features/space-based_laser_communications_break_threshold/

De Pater, I., Hammel, H.B., Showalter, M.R., and van Dam, M.A., The Dark Side of the Rings of Uranus. Science 317, pp. 1888-1890, 2007.

De Pater, I., Romani, P.N., and Atreya, S.K., Possible Microwave Absorption by H_2S Gas in Uranus' and Neptune's Atmospheres. Icarus 91, pp. 220-233, 1991.

De Pater, I., Romani, P.N., and Atreya, S.K., Uranus Deep Atmosphere Revealed. Icarus 82, pp. 288-313, 1989.

Devore, J.L., Probability and Statistics for Engineering and the Sciences. Brooks/Cole, Monterey, CA, 1982.

DiTom Microwave Inc., Space Qualified Isolators And Circulators. Obtained via web May 2016 from: *https://www.rfmw.com/data/DiTom_Space_Capabilities.pdf*

Domingo, M. and Ramirez, J.J., Mechanical Design and Test of Rosetta Platform Louvres.

Proceedings of the 10th European Space Mechanisms and Tribology Symposium, San Sebastián, Spain, 2003.

Dougherty, M.K., Kellock, S., Southwood, D.J., Balogh, A., Smith, E.J., Tsurutani, B.T., Gerlach, B., Glassmeier, K.H., Gleim, F., and Russell, C.T., The Cassini magnetic field investigation. Space Sci. Rev. 114, pp. 331–383, 2004.

Eagle-Picher Industries Inc., Technical Data Sheet for Battery No. SAP-12116. Thermal Battery, 2006. Obtained via web May 2016 from: http://www.electronicsdatasheets.com/download/53735145e34e24db3051a277.pdf?format=pdf

Ellerby, D., Beerman, A., Blosser, M., et al, Heatshield for Extreme Entry Environment Technology (HEEET) for Missions to Saturn and Beyond (poster), Meeting of the Outer Planets Assessment Group, Laurel, MD, 2015.

Ellerby, D., Gage, P., Kazemba, C., Mahzari, M., Nishioka, O., Peterson, K., Stackpoole, M., Venkatapathy, E., Young, Z., Heatshield for Extreme Entry Environment Technology Development Status (presentation), 13th Interplanetary Probes Workshop, Johns Hopkins University, Baltimore, MD, 2016.

Elphic, R.C., Delory, G.T., Hine, B.P., Mahaffy, P.R., Horanyi, M., Colaprete, A., Benna, M., Noble, S.K., and the LADEE Science Team, The Lunar Atmosphere and Dust Environment Explorer Mission. Space Sci. Rev. 185, pp. 3-25, 2014, doi: 10.1007/s11214-014-0113-z.

ESA, *Cassini* Saturn Orbiter and Titan Probe: Report on the Phase A Study, ESA, SCI(88)5, 1988.

Floyd, H., Aurora and magnetic field of Uranus. J. Geophys. Res. 114, 2009, doi:10.1029/2009JA014394.

Force, D.A., Rodríguez-Arroyo, A., Spitsen, P.C., et al., K-Band TWTA for the NASA Lunar Reconnaissance Orbiter. NASA Glenn Research Center, Cleveland, OH, 2008. Obtained via web May 2016 from: http://www.dtic.mil/dtic/tr/fulltext/u2/a493150.pdf

French, R.G., Elliot, J.L., and Levine, S.E., Structure of the Uranian Rings. Icarus 67, pp. 134-163, 1986.

Goebel, D. and Katz, I., Fundamentals of Electric Propulsion: Ion and Hall Thrusters. Wiley, Hoboken, NJ, pp. 1-440, 2008.

Green, M.J. and Davy, W.C., Galileo Probe Forebody Thermal Protection. AIAA 16th Thermophysics Conference, Palo Alto, CA, 1981.

Guillot, T., Atreya, S., Charnoz, S., Dougherty, M. K., and Read, P., Saturn's Exploration Beyond Cassini-Huygens, in: Dougherty et al., Saturn after Cassini-Huygens. Springer, pp. 745-761, 2009.

Guillot, T., Gautier, D., Giant planets, In: Schubert, G., Spohn, T. (Eds.), Treatise on Geophysics, vol. 10 – Planets and Moons. pp. 439–464, 2007, doi:10.1016/B978-044452748-6.00165-6.

Guillot, T., The Interiors of Giant Planets: Models and Outstanding Questions. Annu. Rev. Earth Planet. Sci. 33, pp. 493-530, 2005.

Gurnett, D.A., Kurth, W.S., Kirchner, D.L., Hospodarsky, G.B., Averkamp, T.F., Zarka, P., Lecacheux, A., Manning, R., Roux, A., Canu, P., Galopeau, P., Meyer, A., Gustafsson, G., Wahlund, J., Ahlen, L., Rucker, H.O., Kaiser, M.L., Desch, M.D., Farrell, W.M., Harvey, C.C., and Louarn, P., The Cassini Radio and Plama-Wave Investigation. Space Sci. Rev. 114, pp. 395–463, 2004.

Hammel, H.B., Sromovsky, L.A., Fry, P.M., Rages, K., Showalter, M., de Pater, I., van Dam, M.A., LeBeau, M.A., and Deng, X. The Dark Spot in the atmosphere of Uranus in 2006: Discovery, description, and dynamical simulations. Icarus 201, pp. 257-271, 2009.

Hastie, T., Tibshirani, R., and Friedman, J., The Elements of Statistical Learning: Data Mining, Inference, and Prediction (2nd Ed.). Springer, 2009.

Hayes, S., and Jacobs, M., Spacecraft and Support Function Cost Models for NASA PCEC (presentation slides), NASA 2015 Cost Symposium, Moffett Field, August 25-27, 2015.

Hofstadter, M., and 26 co-authors, The Atmospheres of the Ice Giants, Uranus and Neptune. White Paper For the Planetary Science Decadal Survey 2013-2023, 2010.

Honeywell International Inc., Constellation Series Reaction Wheels. 2003. Obtained via web May 2016 from: http://www51.honeywell.com/aero/common/documents/Constellation_Series_Reaction_Wheels.pdf

Holberg, J.B., Nicholson, P.D., French, R.G., and Elliot, J.L., Stellar Occultation Probes of the Uranian Rings at 0.1 and 2.2 μm: A Comparison of Voyager UVS and Earth-Based Results. Astron. J. 94, No. 1, pp. 178-188, 1987.

Hubbard, W., Lindstorm, K., Turtle, E., Seifert, H., et al., Ice Giants Decadal Study. NASA, SDO-12345, 2010.

Hughes, K.M., Saikia, S.J., Minton, D.A., et al., Design of Interplanetary Trajectories for Uranus Probe and Orbiter Mission Including Two-Planet Saturn-Uranus Opportunity, NASA Outer Planets Assessment Group Meeting, Laurel, MD, August 24-26, 2015.

Hughes, K.M, Agrawal, P., Allen, G.A., Mudek, A.J., Saikia, S.J., Longuski, J.M., Hwang, H.H., and Venkatapathy, E., Trajectories to Uranus from 2024 to 2038 Including an Opportunity for a Saturn Probe, 13th International Planetary Probe Workshop, Johns Hopkins University Applied Physics Laboratory, Laurel, MD, June 13-17, 2016.

Hussmann, H., Sohl, F., and Spohn, T. Subsurface oceans and deep interiors of medium-sized outer planet satellites and large trans-neptunian objects. Icarus 185, pp. 258-273, 2006.

Ice Giants Science Definition Team, Draft Science Traceability Matrix. Obtained via web May

2016 from: http://www.lpi.usra.edu/icegiants/.

Jet Propulsion Laboratory, Spacecraft Visibility Plotter and Horizon Mask Plotter Program, In: DSN Link Communication Handbook, 2015. Obtained via web May 2016 from: http://deepspace.jpl.nasa.gov/dsndocs/810-005/301/SC_Vis_Masks.xlsm

Johnson, S.M., Thermal Protection Materials: Development, Characterization and Evaluation. HiTemp2012, Munich, Germany, 2012.

Johnson, W., Thermal analysis of low layer density multilayer insulation test results. AIP Conference Proceedings 1434, 1519, 2016, doi: 10.1063/1.4707081.

Juhasz, A.J., High Conductivity Carbon-Carbon Heat Pipes for Light Weight Space Power System Radiators. NASA, TM-2008-215420, 2008.

Kargel, J.S., Cyrovolcanism on the Icy Satellites. Earth, Moon, and Planets 67, pp. 101-11, 1995.

Karpathy, A., Convolutional Neural Networks for Visual Recognition, 2016. Obtained via web June 2016 from CS231n course notes: http://cs231n.github.io/neural-networks-1/

L-3 Communications Electron Technologies Inc., Space Qualified TWT Product Listing. Space LTWTA Products, 2012. Obtained via web May 2016 from: http://www2.l-3com.com/eti/downloads/summarytable_space.pdf

L-3 Communications. C-TT/510 Electra Lite - UHF Proximity Link Transceiver. L3 Communications, Mason, OH, 2007. Obtained via wev May 2016 from: http://combatpropulsion.com/products-services/docoutput.aspx?id=1614

Lamy, L., Prangé, R., Hansen, K.C., Earth-based detection of Uranus' aurorae. Geophys. Res. Lett. 39, 2012, doi:10.1029/2012GL051312.

Landau, D., Try, L., Strange, N., Broad Search and Optimization of Solar Electric Propulsion Trajectories to Uranus and Neptune. Amer. Astron. Soc. 09-428, pp. 2093-2112, 2009.

Leinhardt, Z.M., Ogilvie, G.I., Latter, H.N., and Kokubo, E., Tidal disruption of satellites and formation of narrow rings. Mon. Not. R. Astron. Soc. 424, pp. 1419-1431, 2012.

Lindal, G.F., Lyons, J.R., Sweetnam, D.N., Eshleman, V.R., Hinson D.P., and Tyler, G.L., The Atmosphere of Uranus: Results of Radio Occulation Measurements with Voyager 2. J. Geophy. Res. 92, No. A13, pp. 14987-15001, 1987.

Linford, L., NMT's Contributions to the Cassini Saturn Mission Follow Division's Space Exploration Tradition. Los Alamos National Lab., The Actinide Research Quarterly, 1996. Obtained via web May 2016 from: http://www.lanl.gov/discover/publications/actinide-research-quarterly/pdfs/ARQ-1996-10.pdf

Lockwood, M.K., Baily, R.W., Justus, C.G., et al., Aerocapture Systems Analysis for a Neptune Mission. NASA, TM-2006-214300, 2006.

Lunine, J.I., The Atmospheres of Uranus and Neptune. Annu. Rev. Astron. Astrophys. 31, pp.

217-263, 1993.

Marks, G., Keay, E., Kuehn, S., Fedyk, M., and Laraway, P., Performance of the AstroMesh® Deployable Mesh Reflector at Ka-Band Frequencies And Above. Astro Aerospace – Northrop Grumman Aerospace Systems. Obtained via web May 2016 from: http://www.northropgrumman.com/BusinessVentures/AstroAerospace/Documents/pageDocs/tech_papers/tech_papers_AMLiteDe.pdf

Masters, A., Achilleos, N., Agnor, C.B., et al., Neptune and Triton: Essential pieces of the Solar System Puzzle. Space Sci. 104, pp. 108-121, 2014.

Masters, A., Magnetic reconnection at Uranus' magnetopause. J. Geophys. Res. Space Physics 119, pp. 5520–5538, doi:10.1002/2014JA020077.

Mauk, B.H., Haggerty, D.K., Jaskulek, S.E., Schlemm, C.E., Brown, L.E., Cooper, S.A., Gurnee, R.S., Hammock, C.M., Hayes, J.R., Ho, G.C., Hutcheson, J.C., Jacques, A.D., Kerem, S., Kim, C.K., Mitchell, D.G., Nelson, K.S., Paranicas, C.P., Paschalidis, N., Rossano, E., and Stokes, M.R., The Jupiter Energetic Particle Detector Instrument (JEDI) Investigation for the Juno Mission. Space Sci. Rev., 2013, doi: 10.1007/s11214-013-0025-3.

McAdams, J., Scott, C., Guo, Y., Dankanich, J., and Russell, R., Conceptual Mission Design of a Polar Uranus Orbiter and Satellite Tour. 21st AAS/AIAA Space Flight Mechanics Meeting, New Orleans, February 13-17, 2011.

McCleese, D.J., Schofield, J.T., Taylor, F.W., Calcutt, S.B., Foote, M.C., Kass, D.M., Leovy, C.B., Paige, D.A., Read, P.L., and Zurek, R.W., Mars Climate Sounder: An investigation of thermal and water vapor structure, dust and condensate distributions in the atmosphere, and energy balance of the polar regions. J. Geophys. Res. E: Planets 112, pp. 1–16, 2007.

McFadden, J.P., Kortmann, O., Curtis, D., Dalton, G., Johnson, G., Abiad, R., Sterling, R., Hatch, K., Berg, P., Tiu, C., Gordon, D., Heavner, S., Robinson, M., Marckwordt, M., Lin, R., and Jakosky, B., MAVEN SupraThermal and Thermal Ion Compostion (STATIC) Instrument. Space Sci. Rev. 195, pp. 199-256, 2015.

Melaragno, M.G. An Introduction to Shell Structures: The Art and Science of Vaulting. Van Nostrand Reinhold, New York, NY, 1991.

Morton, T., Bryson, S.T., Coughlin, J.L., Rowe, J.F., Ravichandran, G., Petigura, E.A., Haas, M.R., and Batalha, N.M., False Positive Probabilities for All Kepler Objects of Interest: 1284 Newly Validated Planets and 428 Likely False Positives. Astrophys. J. (preprint), May 10, 2016.

Mukai, R., Hansen, D., Mittskus, A., Taylor, J., and Danos, M., Article 16: Juno Telecommunications. Jet Propulsion Laboratory Design & Performance Summary Ser., California Institute of Technology, Pasadena, CA, 2012.

Murray, F.J., The Buckling of Thin Spherical Shells. J. Aerosp. Sci. 28, No. 3, pp. 223-236, 1961.

NASA Space Flight Program and Project Management Handbook, NPR 7120.5, 2010.

National Research Council (U.S.) Committee on the Planetary Science Decadal Survey, Visions and Voyages: for Planetary Science in the Decade 2013-2022. National Academies Press, pp. 175-209, 2011.

NEA Electronics, Hold Down & Release Mechanisms. Products. Obtained via web June 2016 from: http://www.neaelectronics.com/products/hold-down-and-release-mechanisms/

Nellis, W.J., The unusual magnetic fields of Uranus and Neptune. Mod. Phys. Lett. B 29, No. 1, 2015, doi: 10.1142/S021798491430018X.

Ness, N.F., Acúna, M.H., Behannon, K.W., Burlaga, L.F., Connerney, J.E.P., Lepping, R.P., and Neubauer, F.M., Magnetic Fields at Uranus. Science 233, pp. 85-89, 1986.

Niemann, H.B., Harpold, D.N., Atreya, S.K., Carignan, G.R., Hunten, D.M., and Owen, T.C., Galileo Probe Mass Spectrometer experiment. Space Sci. Rev. 60, pp. 111-142, 1992.

Northrop Grumman, Astromesh Deployable Reflector. Northrop Grumman - Space Technology Astro Aerospace, 2004. Obtained via web May 2016 from: http://www.northropgrumman.com/BusinessVentures/AstroAerospace/Products/Documents/pageDocs/DS-409-AstroMeshReflector.pdf

O'Neil, W.J. and Mitchell, K.T., Galileo Mission Overview, 21st Aerospace Sciences Meeting, Reno, NV, 1983.

Ochoa, H., Bhandari, P., Mastropietro, A.J., and Paris, A., Thermal Control Architecture Trade Study for the Europa Clipper Pre-Project Study. Thermal Fluids Analysis Workshop, 2015. Obtained via web May 2016 from: https://tfaws.nasa.gov/files/TFAWS2015-PT-10-Paper.pdf

Orton, G. S., Fletcher, L. N., Moses, J. I., et al., Mid-infrared Spectroscopy of Uranus from the Spitzer Infrared Spectrometer: Determination of the Mean Temperature Structure of the Upper Troposphere and Stratosphere. Icarus 243, pp. 494-513, 2014.

Pappalardo, R.T., Reynolds, S.J., and Greely, R., Extensional tilt blocks on Miranda: Evidence for an upwelling origin of Arden Corona. J. Geophy. Res. 102, No. E6, pp. 13,369-13,379, 1997.

Porco, C.C., West, R.A., Squyres, S., McEwen, A., Thomas, P., Murray, C.D., Delgenio, A., Ingersoll, A.P., Johnson, T.V., Neukum, G., Veverka, J., Dones, L., Brahic, A., Burns, J.A., Haemmerle, V., Knowles, B., Dawson, D., Roatsch, T., Beurle, K., and Owen, W., Cassini imaging science: Instrument characteristics and anticipated scientific investigations at Saturn. Space Sci. Rev. 115, pp. 363-497, 2005.

Püstow, R., Nettelmann, N., Lorenzen, W., and Redmer, R. H/He demixing and the cooling behavior of Saturn. Icarus 267, pp. 323-333, 2016.

Ragent, B., Wong, T., Blamont, J.E., Eskovitz, A.J., Harnett, L.N., and Pallai, A., Pioneer Venus Sounder And Small Probes Nephelometer Instrument. IEEE T. Geosci. Remote GE-18, pp. 111-117, 1980.

Reuter, D.C., Stern, S.A., Scherrer, J., Jennings, D.E., Baer, J., Hanley, J., Hardaway, L.,

Lunsford, A., Mcmuldroch, S., Moore, J., Olkin, C., Reitsma, H., Sabatke, D., Spencer, J., Stone, J., Throop, H., Van, J., Weigle, G.E., and Young, L.A., Ralph: A Visible/Infrared Imager for the New Horizons Pluto/Kuiper Belt Mission. Space Sci. Rev. 140, pp. 129-154, 2008.

Robbins, N.R., Menninger, W.L., Dibb, D.R., and Lewis, D.E. Ka-band Space Traveling Wave Tube Amplifiers. L-3 Communications Electron Technologies, 2006. Obtained via web May 2016 from: http://ieeexplore.ieee.org/stamp/stamp.jsp?arnumber=1666166

Russell, C., The STEREO Mission, Vol. 136. Springer Science & Business Media, p.219, 2008, doi: 10. 1007/s11214-008-9344-1.

Russell, C.T. and Dougherty, M.K., Magnetic Fields of the Outer Planets. Space Sci. Rev. 152, pp. 251-269, 2010, doi: 10.1007/s11214-009-9621-7.

Rymer, A. and 65 co-authors, The Case for Exploring Uranus' Magnetosphere. White Paper For the Planetary Science Decadal Survey 2013-2023, 2010.

Santos, N.C., Martins, J.H.C., Boué, G., et al. Detecting ring systems around exoplanets using high resolution spectroscopy: the case of 51 Pegasi b. Astron. Astrophys. 583, 2015, doi:10.1051/0004-6361/201526673.

Schinder, P.J., Flaser, F.M., Marouf, E.A., and Anabtawi, A., Saturn's Equatorial Oscillation: Evidence of Descending Thermal Structure from Cassini Radio Occultations. April, 2011. Obtained via web June 2016 from NASA Technical Reports Server (NTRS).

Schinder, P.J., Flaser, F.M., Marouf, E.A., and Rappaport, N.J., The Structure of Titan's Atmosphere from Cassini Radio Occultations. August, 2008. Obtained via web May 2016 from NASA Technical Reports Server (NTRS).

Schmidt, G.R., Patterson, M.J., and Benson, S.W., The NASA Evolutionary Xenon Thruster (NEXT): The Next Step for U.S. Deep Space Propulsion. 2008. Obtained via web May 2016 from NASA Technical Reports Server (NTRS).

Seiff, A., and Knight, T.C.D., The Galileo Probe Atmosphere Structure Instrument. Space Sci. Rev. 60, pp. 203-232, 1992.

Sevilla, D.R., The Cassini Main Engine Assembly Cover Mechanism. Thirty-first Aerospace Mechanisms Symposium, Huntsville, AL, 1997.

Showalter, M.R. and Lissauer, J.J, The Second Ring-Moon System of Uranus: Discovery and Dynamics. Science 311, pp. 973-977, 2006.

Siegel, R. and Howell, J.R., Thermal Radiation Heat Transfer, 4th Edition. Taylor & Francis, New York, NY, 2002.

Slobin, S.D., Pham, T., and Chang, C., 103 - 34-m HEF Subnet Telecommunications Interface. Jet Propulsion Laboratory, 810-005, 103, 2014. Obtained via web May 2016 from: http://deepspace.jpl.nasa.gov/dsndocs/810-005/103/103C.pdf

Slobin, S.D., Pham, T., and Chang, C., 104 - 34-m BWG Stations Telecommunications

Interfaces. Jet Propulsion Laboratory, 810-005, 104, 2015. Obtained via web May 2016 from: http://deepspace.jpl.nasa.gov/dsndocs/810-005/104/104H.pdf

Spilker, T.R., Radio Opacity Estimates for Giant Planet Atmospheres. Jet Propulsion Laboratory, California Institute of Technology, 2007. Obtained via web May 2016 from: https://solarsystem.nasa.gov/docs/7_18SPILKER_paper.pdf

Srama, R., Ahrens, T.J., Altobelli, N., Auer, S., and Bradley, J.G., The Cassini Cosmic Dust Analyzer. Space Sci. Rev. 114, pp. 465–518, 2004.

Sromovsky, L.A., Best, F.A., Revercomb, H.E., and Hayden, J., Galileo Net Flux Radiometer Experiment, Space Sci. Rev. 60, pp. 233-262, 1992.

Sromovsky, L.A., Collard, A.D., Fry, P.M., Orton, G.S., Lemmon, M.T., Tomasko, M.G., and Freedman, R.S., Galileo probe measurements of thermal and solar radiation fluxes in the Jovian atmosphere. J. Geophys. Res. 103, pp. 22,929–22,977, 1998.

Sromovsky, L.A., de Pater, I., Fry, P.M., and Marcus, P., High S/N Keck and Gemini AO imaging of Uranus during 2012–2014: New cloud patterns, increasing activity, and improved wind measurements. Icarus 258, pp. 192-223, 2015.

Sromovsky, L.A., Fry, P.M., and Kim, J.H., Methane on Uranus: The case for a compact CH_4 cloud layer at low latitudes and a severe CH_4 depletion at high-latitudes based on re-analysis of Voyager occultation measurements and STIS spectroscopy. Icarus 215, pp. 292-312, 2011.

Sromovsky, L.A., Hammel, H.B., de Pater, I., et al. Episodic bright and dark spots on Uranus. Icarus 220, pp. 6-22, 2012.

Sromovsky, L.A., Karkoschka, E., Fry, P.M., Hammel, H.B., de Pater, I., and Rages, K. Methane depletion in both polar regions of Uranus inferred from HST/ STIS and Keck/NIRC2 observations. Icarus 238, pp. 137-155, 2014.

Stanely, S., and Bloxham, J., Numerical dynamo models of Uranus' and Neptune's magnetic fields. Icarus 184, pp. 556-572, 2006.

Stern, S.A., Slater, D.C., Scherrer, J., Stone, J., Dirks, G., Versteeg, M., Davis, M., Gladstone, G.R., Parker, J.W., Young, L.A., and Siegmund, O.H.W., ALICE: The ultraviolet imaging spectrograph aboard the New Horizons Pluto-Kuiper belt mission. Space Sci. Rev. 140, pp. 155–187, 2008.

Suter, J.J., Crawford, L.J., Montgomery, B.G., and Swann, W.E., Syntonics LLC: APL-Developed Technology Makes Its Commercial Debut. Johns Hopkins APL Technical Digest 22, No. 2, pp. 168-175, 2001. Obtained via web May 2016 from: http://www.syntonicscorp.com/documents/SyntonicsLLC_TechnologyTransfer .pdf

Taylor, J. Article 13: DAWN Telecommunications. Jet Propulsion Laboratory Design & Performance Summary Ser., California Institute of Technology, Pasadena, CA, 2009.

Taylor, J., Sakamoto, L., and Wong, C., Article 3: Cassini Orbiter/Huygens Probe Telecommunications. Jet Propulsion Laboratory Design & Performance Summary Ser.,

California Institute of Technology, Pasadena, CA, 2002.

Terma Space, Power Conditioning & Distribution Unit. Obtained via web May 2016 from: http://www.terma.com/media/177707/power_conditioning_and_distribution_unit.pdf

Thales Alenia Space, Flexible Converter for RF Units and Low Power Applications. Obtained via web May 2016 from: https://www.thalesgroup.com/sites/default/files/asset/document/10W DCDC Flex3.pdf

Thomson, M.W., Astromesh Deplyable Reflectors For Ku- And Ka-Band Commercial Satellites. TRW Astro Aerospace, 2002. Obtained via web May 2016 from: http://www.northropgrumman.com/BusinessVentures/AstroAerospace/ Documents/pageDocs/aiaa-2032.pdf

Trafton, L.M., Miller , S., Geballe, T.R., Tennyson , J., and Ballester , G.E., H2 Quadrupole and H3+ Emission From Uranus: the Uranian Thermosphere, Ionosphere, and Aurora. Astrophys. J. 524, pp. 1029-1083, 1999.

Tsiganis, K., Gomes, R., Morbidelli, A., and Levison, H.F., Origin of the orbital architecture of the giant planets of the Solar System. Nature 435, pp. 459-461, 2005.

Venkatapathy, E., Szalai, C.E., Laub, B., Hwang, H.H., Conley, J.L., Arnold, J., and 90 co-authors, Thermal Protection System Technologies for Enabling Future Sample Return Missions. White Paper to the NRC Decadal Primitive Bodies Sub-Panel, 2010.

Verderame, J. and Stiller, E., Small Deep-Space Transponder (SDST) Reliable X-Band and Ka-Band Deep Space Transmission. General Dynamics Advanced Information Systems. Obtained via web May 2016 from: https://gdmissionsystems.com/wp-content/uploads/2015/07/SDST_-_DS5-813-12.pdf

Webb, C.M., Thermal design of a Saturn/Uranus entry probe for descent missions to 20 bars. 8th Thermophysics Conference, Palm Springs, CA, 1973.

Wijker, J.J., Spacecraft Structures. Springer, Heidelberg, Germany, 2008.

Williams, M., Saturn: The Ringed Gas Giant. Universe Today, August, 2015. Obtained via web May 2016 from: http://www.universetoday.com/15298/saturn/

Williams, M., What Is The Atmosphere Like On Others Planets?. Universe Today, January, 2016. Obtained via web May 2016 from: http://www.universetoday.com/35796/atmosphere-of-the-planets/

Young, D.T., Waite, J.H., Krimigis, S.M., Dougherty, M.K., Gurnett, D.A., Srama, R., et al., The Cassini-Huygens Mission: Orbiter In Situ Investigations. Russell, C. (Ed.), Springer, Kluwer Academic Publishers, Norwell, MA, 2004.

Zahn, U.Von, and Hunten, D.M., The Jupiter Helium Interferometer Experiment on the Galileo Entry Probe. Space Sci. Rev. 60, pp. 263–281, 1992.

Appendix A – Aerocapture

One of the alternative concepts that was investigated was performing an aerocapture at Uranus with small impulsive burns where needed, rather than simply a single large impulsive burn to be inserted into Uranus orbit. The basic architecture requires an aeroshell around the orbiter, which would be discarded after the aerocapture maneuver. Afterwards, impulsive burns would place the orbiter into its final science orbit. Aerocapture serves to reduce the orbital energy from a hyperbolic escape trajectory to an elliptical orbit. The capture orbit should be highly eccentric in order to minimize the maneuver ΔV required to place the spacecraft in the final science orbit. Although it has yet to be performed, aerocapture could enhance, or in some cases enable, a mission to one of the ice giants.

Concept of Operations for Aerocapture

As the spacecraft approaches Uranus, any deployed mechanisms such as magnetometers or antennas are retracted. The spacecraft then orients to approach the atmosphere at the appropriate angle of attack. During the atmospheric phase, a guidance algorithm keeps the vehicle on a trajectory that will lead to capture. Once the capture is complete, the aeroshell is jettisoned from the orbiter and instruments such as the magnetometer can be redeployed. The vehicle then cruises to the apoapsis of the capture orbit, where a minor burn is performed to adjust the orbital periapsis. After coasting to the new periapse, a second impulsive burn is preformed to place the spacecraft in the final science orbit. These operations are summarized in Figure A.1. Note that, although aerocapture can be performed with a single burn, the uncertainty in Uranus' atmosphere forced the trajectory team to consider using two impulsive burns.

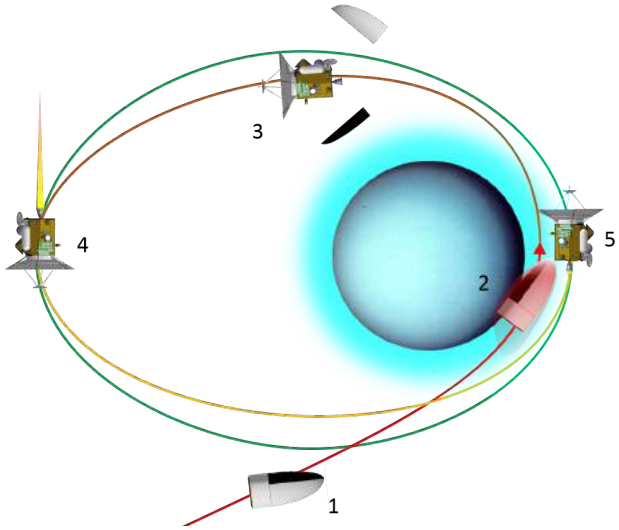

Figure A.1: Concept of operations for aerocapture at Uranus. 1. Orbiter approaches Uranus. 2. Orbiter undergoes atmospheric deceleration. 3. Aeroshell is released. 4. Burn to raise periapsis. 5. Burn to correct apoapsis.

Trajectory Design

Aerocapture design mainly focuses on the trajectory design and vehicle design. The former concentrates on the incoming entry conditions, deliverable mass, and desired outgoing orbit, while the latter impacts the efficiency of the aerocapture maneuver.

Designing the incoming trajectory involves finding an interplanetary trajectory that is feasible in terms of mass delivered and time of flight. Depending on the orientation of the planet relative to the Earth, the entry velocity and flight path angle may have to consider the rings or any moons that are in the way. For a Uranus aerocapture in the 2030s or 2040s, the rings are a major issue in determining which trajectories are safe.

Vehicle Design

Vehicle design impacts the trajectory and the final deliverable mass. Depending on the geometry and the control mechanism, different ballistic coefficients and L/D ratios can be achieved. The main objective is to construct the decelerator to be rigid enough to handle the peak dynamic pressure experienced and be made out of a material resistant enough to handle the heating. The material must also be light and flexibile enough to allow for a significant payload mass and fit into a launch vehicle fairing. A packaging requirement of having an internal volume between 22 and 29 cubic meters was considered. For this study, five types of decelerators were initially investigated: deployable spherecone, deployable spherecone with ballute, rigid sphere cone, rigid spherecone with a ballute, and rigid mid-L/D. The various configurations are depicted below.

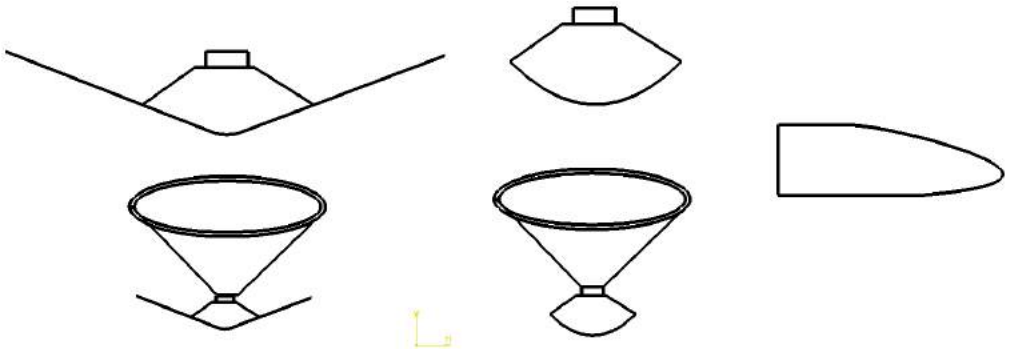

Figure A.2: Aerocapture vehicle concepts. Clockwise from the upper left: deployable spherecone, rigid spherecone, rigid mid-L/D, deployable spherecone with ballute, rigid spherecone with ballute.

One of the main challenges to aerocapture is the narrow aerocapture corridor, which is defined as the exit flight path angle from no orbital energy (i.e. parabolic orbit) to an exit flight path angle that only skips. For an L/D that can be accomplished with a spherecone (~0.2), the aerocapture corridor was less than a quarter of a degree. Mid L/D vehicles (L/D ~ 0.8) have a corridor of approximately 1^{o}, allowing for a larger margin (Lockwood et al., 2006).

For deployable spherecones and spherecones with ballutes, rather than increasing the L/D to allow for aerocapture, the ballistic coefficient was decreased to create a large drag area to aid in deceleration. One of the challenges that these vehicles have is that they need to decelerate as much as possible in the upper atmosphere in order to keep heating rates low. For Uranus, peak heat rates were found to be over the limit for inflatable decelerators (50 W/cm^2), so inflatable deployable decelerators were not considered viable (Cianciolo et al., 2011).

Mechanically deployable decelerators have a higher heat rate limit. For example, the carbon cloth used on the Adaptive Deployable Entry Placement Technology (ADEPT) has a heating limit of about 250 W/cm^2 (Arnold et al., 2013). However, due to launch vehicle fairing constraints, a device similar to ADEPT could not be made large enough to keep Uranus aerocapture heat rates low enough for a carbon cloth TPS.

The rigid mid-L/D vehicle used a superellipsoid construction, described by equation A1. The additional parameters allow for more fine-tuning of the geometry to increase internal volume. The front portion of the vehicle uses two superellipsoids: one for the bottom and top.

$$(|x|^r + |y|^r)^{t/r} + |z|^t = 1 \qquad \text{(A1)}$$

Aerodynamic coefficients were determined using Newtonian impact theory. Equation A2 was calculated on each panel and numerically integrated to calculate the overall aerodynamic performance.

$$C_p = C_{p,\max} \sin^2(\theta) \qquad \text{(A2)}$$

$C_{p,max}$ represents the pressure coefficient at the stagnation point and θ is the angle between the local inward surface normal and the freestream velocity vector.

An ellipsed that is 5.8 m long, 2.6 m tall, and 3.5 m wide was created for the aerocapture analysis. Figure A.3 shows the shape and dimensions of the vehicle. Table A.1 presents a number of important parameters associated with the vehicle.

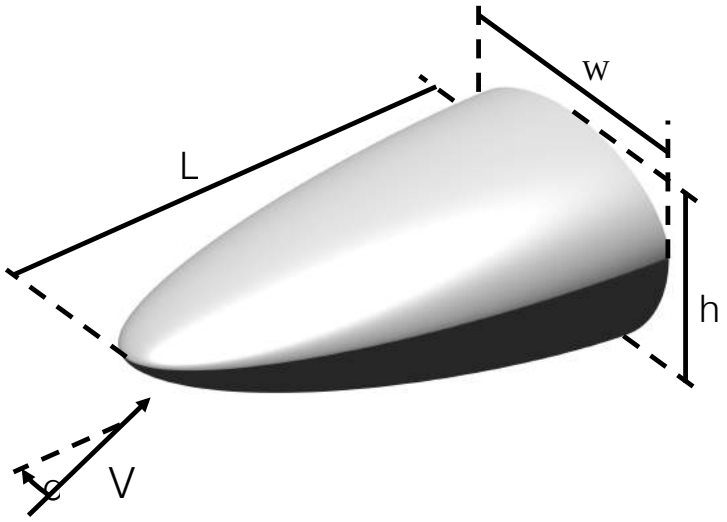

Figure A.3: Ellipsled geometry for the rigid mid-L/D aerocapture shell.

Table A.1: Important values for the ellipsesled aerocapture vehicle.

Variable	Value
L	5.8 m
h	2.6 m
w	3.5 m
α_{trim}	20.12°
L/D_{trim}	1.457
β_{trim}	1397 kg/m^2
Volume	23.3 m^3
S_{ref}	5.919 m^2
S_{wet}	44.91 m^2
$R_{n,x,trim}$	3.72 m
$R_{n,y,trim}$	3.93 m

To calculate the post-aerocapture usable payload mass, the TPS mass and propellant mass for orbit corrections were considered. For an entry velocity of 24.14 km/s and a flight path angle of -12.53^o, the TPS mass was computed to be 795 kg and propellant mass was 1728 kg. The resulting usable payload mass was 2205 kg.

Relative to the impulsive capture cases, the delivered mass to Uranus orbit was higher. However, the larger launch mass, along with the development costs for aerocapture vehicles, caused aerocapture to exceed the cost limits outlined in the study.

Appendix B – Propulsion Trades

Chemical Propulsion or Solar Electric Propulsion

Ultimately, the decision to use either conventional chemical propulsion or solar electric propulsion as a means to reach Uranus depended almost entirely on the trajectory that would be chosen. Some trajectories require impulsive burns in order to target their next flyby bodies, while others are optimized for low thrust solar electric propulsion using the JPL low thrust optimizer, MALTO. Therefore, the decision to use either chemical propulsion or solar electric propulsion was not only a trade study within the propulsion team, but a system-level trade. Both chemical propulsion systems and solar electric propulsions systems therefore had to be researched and explored before a final trajectory decision was made.

Solar Electric Propulsion System Trade Study

Solar electric propulsion combines low-thrust, high I_{sp} electric propulsion with state of the art solar panel technologies to create a constant thrust that slowly accelerates a spacecraft over a long period of time (Goebel and Katz, 2008). The result is a spacecraft that can reach its target body more efficiently and in a timelier manner. Generally, a spacecraft using low-thrust propulsion systems will reach its target body at a faster relative velocity, increasing the advantage of using aerocapture as a deceleration strategy while decreasing the viability of chemical burns. However, this is not always the case as some trajectories were found that utilized low-thrust and yet were still perfectly viable candidates for a chemical deceleration.

JPL's MALTO software optimizes low thrust trajectories by considering (among other things) a specific low-thrust engine. Therefore, a trade study between possible engines for a solar electric propulsion system had to be conducted in the early stages of this study. Specific properties of the engine that was ultimately chosen would then be inputted into MALTO to allow the program to optimize trajectories more accurately. The details and results of this trade study are outlined in the following paragraphs.

Goebel and Katz (2008) have outlined the key differences, advantages, and disadvantages to the many different varieties of electric propulsion. Using their work as a guide, the propulsion team gained a more enhanced understanding of what possible engine candidates were available for this mission. Possible solar electric propulsion candidates are: resistojets, arcjets, ion thrusters, hall thrusters and pulsed plasma thrusters (Goebel and Katz, 2008). Table B.1 shows, qualitatively, the key properties of each type of electric propulsion.

Table B.1: Comparison of several modern electric propulsion systems.

Electric Thruster Type	I_{sp} (s)	Efficiency (%)	Input power (kW)	Propellant
Resistojet	300	65 – 90	0.5 – 1	N_2H_4
Arcjet	500 - 600	25 – 45	0.9 – 2.2	N_2H_4
Ion thrusters	2500 - 3600	40 – 80	0.4 – 4.3	Xenon
Hall thrusters	1500 – 2000	35 – 60	1.5 – 4.5	Xenon
Pulsed plasma	850 - 1200	7 – 13	< 0.2	Teflon

Based on the results tabulated in Table B.1, ion thrusters were chosen to be the most likely candidate for a solar electric prolusion system. This was due to their high I_{sp} and efficiency. The high input power of ion thrusters could also be matched by state-of-the-art solar panel technologies.

Next, the propulsion team researched specific ion engines that have been developed for or flown on past space missions in order to achieve a greater understanding of the performance capabilities of existing ion engines. Again, Goebel and Katz have outlined all ion engines that have ever flown as well as some ion engines that are currently in development. Existing ion engines and some properties are tabulated in Table B.2.

Table B.2: Properties of existing or near-future ion engines

Engine	First Flown	Thrust (mN)	I_{sp} (s)	Power (kW)	Efficiency (%)
13 cm XIPS	Hughes PAS-5, 1997	17.2	2507	0.421	50
25 cm XIPS	Boeing 702 Communication Satellite,	166	3550	4.200	69
NSTAR	Deep Space 1, 1998	92.7	3127	2.567	62
T5	ESA Artemis, 2001	18	3200	0.476	55
RIT-10	ESA Artemis, 2001	15	3400	0.459	52
NEXT	NASA ARRM, 2020s (planned)	236	4190	6.860	71

Based on the results tabulated in Table B.1, the NEXT engine (or NASA Evolutionary Xenon Thruster) was chosen as the best thruster for solar electric propulsion. The NEXT thruster has relatively high thrust (236 mN), a high I_{sp}, and high efficiency. The NEXTs high input power is of little concern, as a solar electric propulsion system would already need to employ state-of the art solar panel technologies that could reasonably power an array of NEXT engines.

JPL's MALTO software requires the user to define an engine or pick one from a list of pre-defined engines. The NASA Evolutionary Xenon Thruster (NEXT) is already defined in MALTO. MALTO will optimize how many engines are needed in an array and the ideal duty cycle for this array. Because of this, the solar electric propulsion system trade study only needed to pick an engine to input into MALTO and allow MALTO to optimize the system.

Chemical Rocket Engine Trade Study

A Uranus trajectory was chosen by a system level trade study based on a pool of possible trajectories provided by the mission design team. Ultimately, the trajectory that was chosen is purely ballistic. Impulsive burns are required following release of both the Saturn and Uranus probes prior to the Saturn flyby and Uranus arrival respectively. These maneuvers are referred to as deflection maneuver 1 (DM1) and deflection maneuver 2 (DM2) respectively. The trajectory that was chosen was also deemed infeasible for aerocapture at Uranus by the systems and aerocapture/entry teams, meaning an impulsive burn is required for Uranus orbit insertion (UOI) as well. Table B.3 below presents the ΔV budget for the trajectory that was chosen. It will be the basis of the following chemical engine trade study.

Table B.3: ΔV Budget

Maneuver	ΔV (m/s)
DM1	158
DM2	8
UOI	1236
Total	1402

With the ΔV budget for the entire trajectory established, a trade study was conducted to select the best engine for mission. A tool was created in Microsoft Excel® which compares the properties of a variety of existing rocket engines. Based on the properties of these engines and the ΔV budget above, the engines can be compared based on the amount of engines needed to achieve the required ΔV, the mass of fuel needed, and the mass of oxidizer needed. These are the basis of the trade study between multiple engines.

Table B.4 below shows the important properties of all of the engines considered (Aerojet Rocketdyne, 2006). Note that all engines below used monomethyl hydrazine (MMH) and nitrogen tetroxide (MON-3) as their fuel and oxidizer, respectively.

Table B.4: Properties of candidate engines for the OCEANUS orbiter.

Name	Expansion Ratio	Force	I_{sp} (s)	O/F Ratio	Maximum Steady State Firing Time (s)	Total Impulse Demonstrated (N-s)	Mass (kg)	TRL
R-4D	44:1	490	300	1.65	12000	20016500	3.4	9
R-4D	164:1	490	311	1.65	12000	20016500	3.76	9
R-4D	300:1	490	316	1.65	12000	20016500	4.31	9
Hi-Pat	300:1	445	320	1	3600	20016500	5.2	9
Hi-Pat	375:1	445	323	1	3600	20016500	5.44	9
Hi-Pat DM	300:1	445	326	0.85	1800	2150000	5.2	8
Hi-Pat DM	375:1	445	329	0.85	1800	2150000	5.44	8
R-42 DM	200:1	890	327	1	1000	20000000	7.3	6
AMBR	400:1	623	333	1.1	2700	5586000	5.4	6

Calculations were performed for each engine based on their properties and the ΔV budget. For each burn (DM1, DM2, UOI) the propellant mass, impulse and burn time were calculated for each engine. The total mass and volume of fuel and oxidizer was calculated as well as the total impulse and burn time. A 12% tanking factor was assumed, meaning that the mass of the propellant tanks and structure is equal 12% of the total propellant mass. Based on the propellant mass of each burn, and accounting for dropping mass at Saturn and Uranus, a final orbiter mass was calculated that could be delivered by each engine. Finally, by comparing the burn time of the longest burn (UOI) to the maximum burn time of each engine, the amount of engines needed to accomplish the mission was calculated. An extra engine was then added for risk mitigation purposes.

By subtracting the tank mass and engine mass from the orbiter mass, a usable mass was calculated. This was done in order to compare masses between engine candidates without considering the mass of the propellant tanks or engines. The results from these calculations are tabulated in Table B.5 below.

Table B.5: Comparison of OCEANUS engine canditates.

Engine		R-4D			Hi-Pat		Hi-Pat DM		R-42 DM	AMBR
Expansion Ratio		44:1	164:1	300:1	300:1	375:1	300:1	375:1	200:1	400:1
DM 1	Propellant mass (kg)	185.2	178.8	176.1	173.9	172.3	170.8	169.3	170.3	167.3
	Burn time (s)	1174	1173	1172	1290	1290	1290	1290	644.7	920.6
	Impulse (kN-s)	545	545.5	545.8	545.9	546.1	546.2	546.3	546.2	546.5
DM 2	Propellant mass (kg)	8.66	8.38	8.25	8.15	8.08	8.01	7.94	7.99	7.85
	Burn time (s)	49.33	49.43	49.48	54.52	54.55	54.58	54.61	27.29	39.03
	Impulse (kN-s)	25.50	25.55	25.57	25.59	25.60	25.62	25.63	25.62	25.65
UOI	Propellant mass (kg)	1092	1063	1050	1040	1032	1025	1018	1023	1009
	Burn time (s)	9978	9920	9895	10870	10860	10840	10830	5419	7721
	Impulse (kN-s)	3213	3242	3254	3264	3271	3279	3286	3281	3295
Total	Propellant mass (kg)	1286	1250	1234	1222	1213	1204	1195	1201	1184
	Impulse (kN-s)	3783	3813	3826	3836	3843	3850	3858	3853	3867
	Tanking Factor (kg)	154.3	150.0	148.0	146.6	145.5	144.5	143.4	144.1	142.0
	Num. Engines	1	1	1	4	7	7	7	6	3
	Contingency Engine	1	1	1	1	1	1	1	1	1
	Engine mass (kg)	6.80	7.52	8.62	26.0	43.5	41.6	43.5	51.1	21.6
	Captured mass (kg)	2091	2127	2143	2155	2164	2173	2182	2176	2193
	Capture mass – tanking factor – engine mass (kg)	1932	1970	1986	1982	1975	1987	1995	1980	2030

From Table B.5 above, four possible engines stand out as delivering the most usable mass to Uranus: AMBR, Hi-Pat DM (both expansion ratios), and the R-4D 300:1. These engines deliver 2030, 1995, 1987 and 1986 kilograms of usable mass to Uranus, respectively. However, the maximum possible burn time of both the AMBR and Hi-Pa DM are considerably lower than that of the R-4D, meaning that 3 AMBRs would be required to achieve UOI (plus one contingency) and 7 Hi-Pat DMs would be required (plus one contingency). On the other hand, only one R-4D (plus one contingency) would be required to achieve UOI, making the overall propulsion system using an R-4D 300:1 simpler and less risky than the AMBR or Hi-Pat DM options. It was because of this trade-off that the propulsion team elected to select the Aerojet Rocketdyne R-4D 300:1 expansion ratio rocket engine, which delivers a sizable 1986 kilograms of usable mass to Uranus with a relatively simple configuration.

Appendix C – Thermal Design

For thermal system design, the orbiter and the probes must be considered as two distinct systems undergoing thermal loads. There are several different stages of flight the orbiter and probes will experience. Each of these stages presents unique thermal loads that must be accounted for in the overall system's design. The first phase to be considered is the cruise phase. The orbiter will be exposed to the majority of its radiation flux during this period. Similarly, the probe is housed under an environmental cover, shadowed from direct solar flux except for brief mid-cruise maneuvers. It is not powered on during these maneuvers. The spacecraft will experience a significant amount of solar flux, as well as irradiance from other bodies.

The next phase is the probe cruise, also known as the probe transit phase. The probe will be directly exposed to solar radiation as well as radiation from other bodies. The radiation environment should not be a concern with the internal electronics, considering the low transit time, which is roughly 130 days. The following stage is the probe entry phase. During this phase, the probe's internal electronics activate from the internal timer. The aeroshell and heatshield will separate followed by deployment of the parachute. The temperature gradient is the highest at this phase. Then begins the atmospheric descent phase. This is the science acquisition phase for the probe. Science data is transmitted to the orbiter and is retransmitted to Earth. Once OCEANUS enters orbit around Uranus, the final science orbit phase begins. This is the main mission of the orbiter. The thermal loads experienced during this phase will not be considerable relative the cruise phase.

With these different phases in consideration, there needs to be an appropriate thermal design to maintain the internal subsystems' functionality by keeping the probe temperature within specified limits. For OCEANUS, an internal temperature between -10°C and 50°C (263K – 323K) encompasses the specified operating temperature of the components. For this analysis, only the orbiter and probe cruise phases as well as the science orbit phase will be considered.

Steady State Thermal Analysis

To determine the thermal systems necessary, the thermal conditions the orbiter and probes will encounter during their cruise phases must be analyzed. First, the correct tools must be developed to analyze the inputs and outputs of the spacecraft during flight to the outer bodies. This can be treated as a basic thermodynamic problem. According to the first law of thermodynamics, the increase in internal energy of a closed system is equal to the heat supplied to the system minus the work done by it. This is shown in Equation C1.

$$\Delta U_{system} = Q - W \tag{C1}$$

Since the spacecraft is a closed system, $\Delta U_{system} = 0$. The net work done by the system is equal to the difference of the heat in (Q_{in}) and heat out (Q_{out}). From this basic understanding, Equation C2 can be derived.

$$q_{in} - q_{out} + q_{dissipated} = \frac{\partial E_{int}}{\partial t} \tag{C2}$$

This means that, in a steady-state, the energy absorbed plus the energy dissipated minus the energy emitted is zero. From this understanding, it can be applied it to OCEANUS. First, the heat inputs of the systems need to be identified. The most obvious one being direct radiation from the Sun. Next, the heat radiated from other bodies such as Earth or Saturn must be considered. Not only the heat generated from the bodies have to be considered, but also the reflected solar energy from these bodies. Finally, the heat input from the spacecraft internal systems such as the batteries and radioisotope heater units, which will be defined as Q, need to be factored in. The outputs of the spacecraft will be the heat radiated out. This can be organized into the equation shown below.

$$Heat\ radiated\ \ to\ space = direct\ solar\ input + reflected\ solar\ input + heat\ radiated\ from\ nearby\ bodies + internal\ heat\ generation$$

For this analysis, neither conduction nor convection were considered since the primary means of energy transfer for spacecraft is through radiation. The spacecraft was assumed to be a sphere for this analysis. It is also assumed that the absorptivity stays constant over time. Finally, it was assumed that the spacecraft behaves similar to a blackbody.

For the heat radiated to space, the value can be defined as J. From the Stefan-Boltzmann law,

$$J = A\varepsilon\sigma T^4 \tag{C3}$$

where A is the surface area of the spacecraft, ε is the emissivity of the spacecraft, σ is the Stefan-Boltzmann constant and T is the surface temperature of the spacecraft. The direct solar input is,

$$Direct\ solar\ input = A_c J_s \alpha \tag{C4}$$

where A_c is the cross-sectional area of the spacecraft. J_s is the solar radiation intensity and α is the absorptivity of the spacecraft.

Now the next term is considered:

$$Heat\ radiated\ from\ nearby\ body = A_c \varepsilon J_p F \tag{C5}$$

Here, J_p is the body's radiation intensity and F is the viewing factor. The viewing factor is the fraction of energy exiting an isothermal, opaque, and diffuse surface by emission or reflection that directly impinges on another surface.

Next, the albedo from other bodies must be taken into account:

$$Reflected\ solar\ input = A_c J_a \alpha \tag{C6}$$

In this instance, $J_a = albedo * J_s * a$. Albedo is the ratio of reflected radiation from the surface to incident radiation upon it. The variable a is the fraction of albedo being seen by the spacecraft.

Now that we have defined all of the terms, we can combine them into a full equation:

$$A\varepsilon\sigma T^4 = A_c \alpha J_s + A_c \alpha J_a + A_c \varepsilon F J_p + Q \tag{C7}$$

From Equation C7 this, the surface temperature of the spacecraft can be isolated.

$$T = \sqrt[4]{\frac{\frac{\alpha}{\varepsilon}\left(\frac{A_c}{A}(J_s + J_a)\right) + \frac{A_c}{A} F J_p + \frac{Q}{\varepsilon A}}{\sigma}} \tag{C8}$$

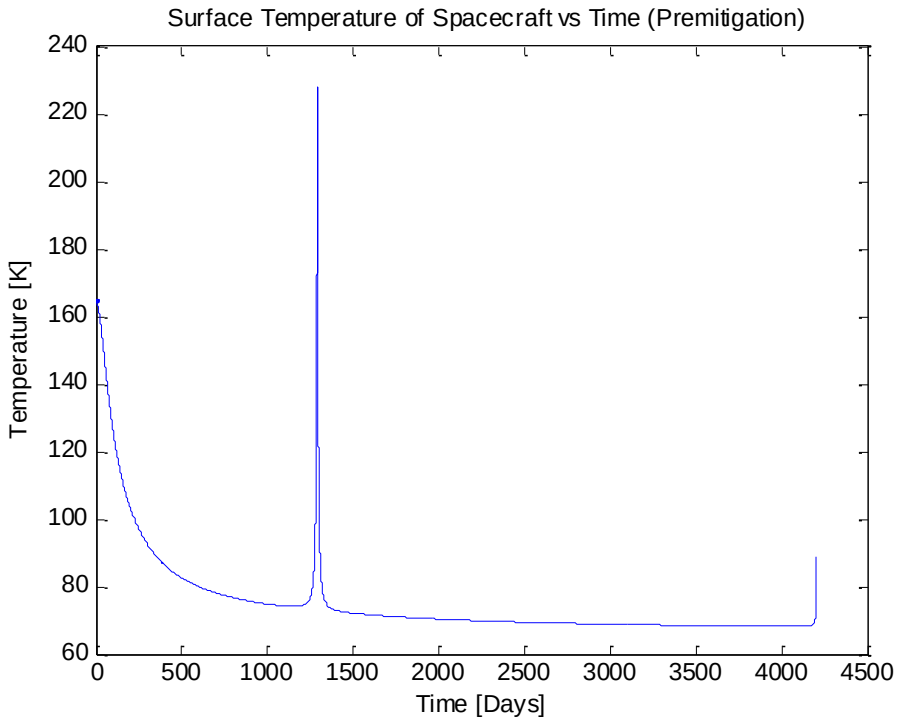

Figure C.1: Surface temperature of the spacecraft. Notable are two major spikes in the steady-state temperature, which correspond to the Saturn encounter and approach to Uranus.

Figure C.1 shows the surface temperature of the spacecraft versus time during the cruise. It should be noted that this analysis is for the purely ballistic case, as opposed to the SEP or aerocapture cases, which were also considered for this project. It should also be noted this is before any thermal system had been included in our design. Hence, the plot represents the raw thermal loads experienced by the spacecraft. As one can see from the plot in Figure C.1, there are several distinct temperature spikes. These spikes correspond to the Saturn encounter (near 1300 days) and the approach to Uranus (near 4200 days). As the spacecraft nears these bodies, the increased heat contribution of thermal and albedo radiation manifests as a brief increase in the steady-state temperature.

Now that the ambient thermal loads the spacecraft will undergo are known, the thermal control systems that will regulate the internal temperature of the orbiter and probe can be determined.

Thermal Control System Design

As mentioned previously, orbiter cruise, probe cruise, and spacecraft science orbit are the distinct phases that need to be considered. There are two types of thermal control components: active and passive thermal control. Active thermal control components refer to cooling or heating techniques that require energy to operate. Passive components do not need a power source to provide protection for the spacecraft since they rely simply on the thermodynamics of conduction, convection or radiation for heat transfer. The orbiter and probes will rely on a combination of these two types of thermal management systems.

Passive thermal control is the most cost effective and widely used thermal management strategy. Radioisotope Heater Units, or RHUs, are extremely common on modern deep space missions. They employ radioactive decay of plutonium-238 for heat generation. These small units (approximately 40 grams per unit) greatly reduce the complexity of heater subsystems by not relying on electrical heating (Linford, 1996). RHUs must be placed strategically throughout the orbiter and probe in order to provide the necessary heating. There must be clusters surrounding temperature sensitive instruments as well the internal electronics such as the onboard computer or navigation system. Within the probes, the RHUs should be located in the service area surrounding the aeroshell. There will be 157 total RHUs in the spacecraft. Roughly 20 will be on each probe and the rest will be on the orbiter. This is based on *Cassini* heritage plus a margin considering the lower ambient temperatures that will be encountered relative to *Cassini*.

Another common thermal management tool to be used is Multilayer Insulation (MLI). MLI is a thermal insulation designed to reduce radiative heat loss. It is characterized by the gold foil material seen on most spacecraft. The Quest MLI from test batch A142 (Johnson, 2012) at 20 layers to insulate the spacecraft and orbiter was chosen for the thermal system design. At 0.52 layer/mm, this MLI will be able to insulate the spacecraft sufficiently from radiative heat losses. MLI will be used on the OCEANUS orbiter as well as both probes. Figure C.2 shows MLI being applied to the *Huygens* entry probe on the *Cassini-Huygens* mission.

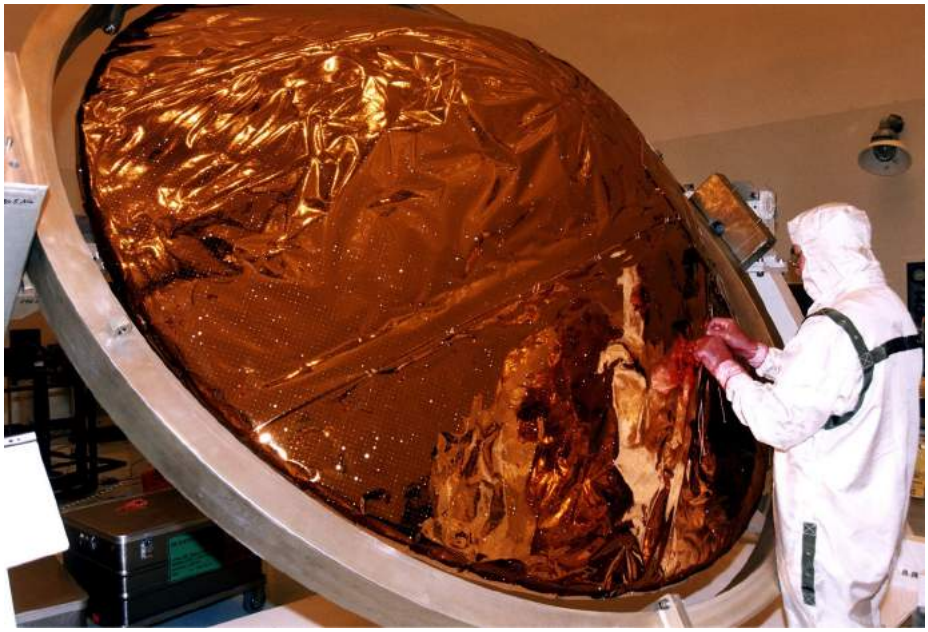

Figure C.2: Multi-layer insulation on the *Huygens* entry probe.

The next passive system used in the design is internal foam insulation. This performs the same action as the MLI, but is internal and surrounds some of the internal components, such as the main battery. Foam with a density of 96 kg/m^3 will be used (Webb, 1973). This insulation will be used mainly on the probe. This is because the probe cannot afford to have as many active control systems on it as the orbiter due to power limitations. The same insulation will also surround the main battery. Since the probe descent heat losses are critical, a 1 cm thick layer of foam insulation can be used to isolate the battery and allow cooler probe equipment temperature.

Another passive system to be considered are Optical Solar Reflectors (OSR). These provide a thermal control surface for a spacecraft by reflecting albedo from surrounding bodies, reducing irradiance input. An OSR consists of flexible tiles. Each tile includes a transparent substrate with a reflective second surface, such as a coating of silver. The front (or space-facing side) is coated with a transparent, electrically conductive layer of indium oxide or indium-tin oxide, which laps over the edges of the OSR tile and is in electrical contact with the reflective coating (Amore, 1995).

Another device is heat pipes. These combine thermal conductivity and phase transition to manage the heat transfer process. The working fluid (liquid sodium metal for OCEANUS) vaporizes by absorbing heat from the hot interface. The vapor then travels along the heat pipe and condenses at the cold interface releasing the heat. Heat pipes operate near isothermally, so they are ideal for spacecraft applications. 170 heat pipes can be placed throughout the spacecraft to manage and disperse the heat generated by internal

components and the eMMRTGs (Juhasz, 2008). Note that the waste heat from the eMMRTGs were considered as inputs into this thermal system.

An active system that was considered consider was louvres. A louvre system is an important part of a spacecraft thermal management system. These vents dump more or less power into space to accommodate extreme variation of energy from internal power and incoming fluxes. Special blades cover a radiator which can open or close depending on the temperature. This varies the infrared emittance of the spacecraft. There will be 14 louvres used on our spacecraft, based on previous deep space mission heritage. Each SENER louvre will only be 0.785 kg (Domingo and Ramirez, 2011). The louvres used on the *Rosetta* spacecraft are pictured in Figure C.3.

Figure C.3: The white rectangles on the *Rosetta* spacecraft shown above are the louvres which are similar to the ones planned for OCEANUS.

With the major components of the thermal subsystem defined, Tables C.1 and C.2 tally the mass requirements for the subsystem.

Table C.1: Orbiter thermal subsystem mass estimates

Orbiter Component	CBE Mass (kg)
Multilayer Insulation	12.6
Optical Solar Reflector	1.3
Radioisotope Heating Units	6.3
Heat Pipes	49.6
Louvre	11.0
TOTAL	**80.8**

Table C.2: Probe thermal subsystem mass estimates

Probe Component	CBE Mass (kg)
Multilayer Insulation	2.0
Internal Insulation	3.8
Radioisotope Heating Units	0.7
TOTAL	**6.5**

Appendix D – Entry and Descent Analysis

The OCEANUS mission calls for atmospheric probes to encounter Saturn's and Uranus' atmosphere at a high entry velocity. To help alleviate the effects of the high velocities experienced during a Saturn entry, a trajectory was chosen near the equator that would enter the same direction as the rotation of the atmosphere, allowing the atmospheric-relative entry velocity to decrease by some 10 km/s. Uranus' rotation does not allow for a significant reduction in the atmospheric-relative entry velocity due to its 98° axial tilt.

Both probes were designed to be identical in order to reduce mission cost, with the aeroshell being slightly larger in diameter and the TPS thicker for the Saturn probe. Encased by the heat shield is a spherical titanium pressure vessel that is identical for both planets, and designed to withstand 120 bars after safety factors have been applied. The pressure vessel houses 6 science instruments with enough power from a primary battery block to last for 2.5 hours.

Overview of Entry and Descent

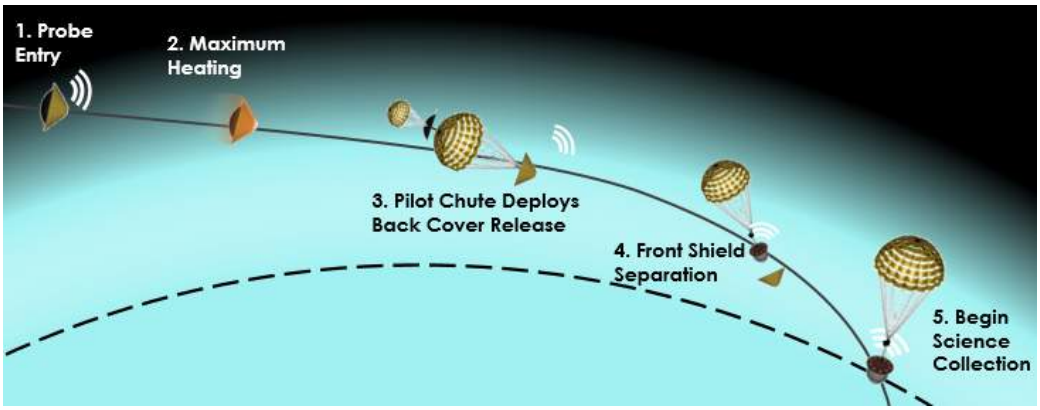

Figure D.1: General concept of operations for probe entry.

The equations normally used to describe the trajectory that a spacecraft follows while undergoing atmospheric drag consider velocity vector magnitude and direction, gravitational forces, aerodynamic forces, and planet rotation. The six equations of motion used to simulate the trajectory are in Equations D1-D6.

$$\frac{dr}{dt} = V\sin(\gamma) \tag{D1}$$

$$\frac{dV}{dt} = -\frac{\rho V^2}{2\beta} - g\sin(\gamma) + f\cos(\gamma)\sin(\xi) + \omega^2 r\left(\sin(\gamma)\cos^2(\phi) + \cos(\gamma)\sin(\xi)\cos(\phi)\sin(\phi)\right) \tag{D2}$$

$$\frac{d\gamma}{dt} = \frac{\rho V}{2\beta}\frac{L}{D}\cos(\sigma) + \left(\frac{V}{r} - \frac{g}{V}\right)\cos(\gamma) - \frac{f}{V}\sin(\gamma)\sin(\xi) + 2\omega\cos(\xi)\cos(\theta) + \omega^2\frac{r}{V}\left(\cos(\gamma)\cos^2(\phi) - \sin(\gamma)\sin(\xi)\cos(\phi)\sin(\phi)\right) \quad \text{(D3)}$$

$$\frac{d\theta}{dt} = \frac{V\cos(\gamma)\cos(\xi)}{r\cos(\phi)} \quad \text{(D4)}$$

$$\frac{d\phi}{dt} = -\frac{V\cos(\gamma)\sin(\xi)}{r} \quad \text{(D5)}$$

$$\frac{d\xi}{dt} = \frac{\rho V}{2\beta}\frac{L}{D}\frac{\sin(\sigma)}{\cos(\gamma)} + \frac{V}{r}\cos(\gamma)\cos(\xi)\tan(\phi) + \frac{f}{V}\frac{\cos(\xi)}{\cos(\gamma)} + 2\omega\left(\sin(\gamma) + \tan(\gamma)\sin(\xi)\cos(\phi)\right) + \omega^2\frac{r}{V}\cos(\xi)\cos(\phi)\sin(\phi)\cos(\gamma) \quad \text{(D6)}$$

In the equations, r describes the distance between the spacecraft and center of the planet, V is the velocity, γ is the flight path angle, θ is the longitude, ϕ is the latitude, ξ is the heading, β is the ballistic coefficient, ρ is the atmospheric density, g is the vertical component of gravity, f is the horizontal component of gravity, ω is the rotation of the planet, L/D is the lift-to-drag ratio, and σ is the bank angle. In addition to the equations of motion, several other equations help determine the vehicle requirements that are dependent on the trajectory, but have no impact on the trajectory. For instance, the heat rate, heat load, and deceleration equations are shown below.

$$\frac{dq}{dt} = \dot{q} = C\rho^a R_n^b V^d \quad \text{(D7)}$$

$$Q = \int_{t_i}^{t_f} \dot{q}\, dt \quad \text{(D8)}$$

$$g = \frac{\rho V^2}{2\beta g_e} \quad \text{(D9)}$$

C, a, b, and d are constants that are specific to a gas composition. Both convective and radiative heat rates can be represented this way for simplicity. All of the first order differential equations were propagated using MATLAB's ode45 with maximum tolerances of 1×10^{-13}. Propagation was done until reaching an appropriate end condition (e.g. entry altitude for aerocapture or one bar pressure).

Determining the trajectory of any atmospheric entry required iteration between the mission design team for the entry conditions, the EDL team for the vehicle conditions, and vehicle design team for determining realistic vehicle requirements. The key entry constraints focus on heat flux, heat load and deceleration. The peak heat flux determines which TPS can be used, the heat load determines how much TPS is required,

and the deceleration must be limited below the safety margin for the instruments aboard. The vehicle constraints are defined by the total mass, the base radius and the vehicle properties of the probe. Of these, the mass of the TPS should be minimized in order to reduce the total mass of the vehicle, the base radius must be within the allowable payload faring size as well as fit easily on the orbiter vehicle and the vehicle properties determine the stability and effectiveness of the probe to decelerate in the atmosphere.

Other issues were also considered, such as avoiding the rings of Uranus and Saturn and targeting specific regions of the planets that were scientifically valuable. The science instruments aboard the probe have a limit in the deceleration loads depending on the instrument. Based on research into heritage designs, the decelerations loads should be reduced as much as possible in order to allow for a wider range of instruments to be used aboard the probe. For this purpose, a defined constraint was set to 125 Earth G's to provide the greatest range of instruments while keeping the entry conditions feasible.

Saturn Entry & Descent

Saturn Properties & Constraints

Saturn poses many challenges for atmospheric entry. To start with, Saturn is a super rotator completing a full revolution in just less than 11 Earth hours. This rotational period translates into a rotational speed of 9.83 km/s at the equator of the massive gas giant. This rotation is both the saving grace and most dangerous feature of Saturn depending on the entry vector. In order to take maximum advantage of the rotation, the optimal decision is to approach Saturn in the same direction as its spin and as close to the equator as possible. Generally, this is ill advised due to the presence of Saturn's rings, which must be avoiding by beginning entry before the ring plane is crossed. Note that the "surface" from which altitudes are referenced is defined as the altitude where 1 bar atmospheric pressure can be found.

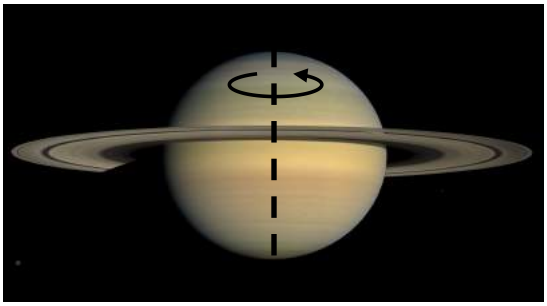

Figure D.2: Saturn's super rotation of 9.83 km/s at 0 km altitude on the Equatorial Plane.

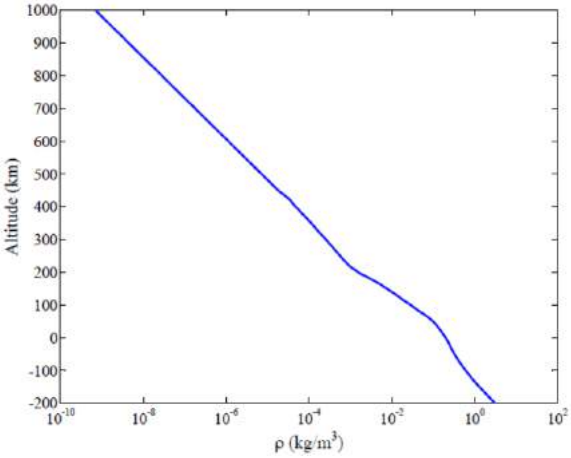

Figure D.3: Saturn atmosphere density model; semilog scale, Schinder model with logarithmic extrapolation at high and low altitudes.

In order to consider the entire atmosphere, an entry altitude was chosen to be 1000 km above the surface as the closest pass by *Cassini* was at 1200 km altitude and there was no significant heating as a result. It is important to give full consideration to the atmosphere at high altitudes, especially for planets like Saturn that have dense atmospheres. However, this can present a challenge as the current scientific model, provided by Paul J. Schinder, for Saturn's atmosphere ends at 457 km above 1 bar (Personal communication, 2016). In order to determine the atmospheric properties at higher altitudes, a logarithmic extrapolation provided by Gary Allen of NASA Ames Research Center was employed (Personal communication, 2016). In addition, it would be optimal to enter Saturn on the equator and aligned with the spin of the planet in order to take maximum advantage of the rotation and reduce the atmospheric relative entry speed, but the rings make this problematic for the OCEANUS orbiter spacecraft. As such, an additional requirement for the mission designer was to ensure the entry began before crossing the ring plane.

Saturn Entry Probe Shell Design

In order to act as an effective decelerator as well as to lower deceleration loads in the Saturnian atmosphere, a 45^o sphere cone was chosen similar to what was used on the *Galileo* probe. A stability concern determines that a 45^o sphere-cone should use a nose to base radius ratio below 0.5 and nominally 0.351. Furthermore, the center of mass should be located on the geometric axis of the probe towards the front and past the base edge of the front shell TPS.

Other constraints to the entry trajectory are provided through the chosen TPS material. For HEEET, a limit of 7000 W/cm^2 was used. While this limit can be reduced, it would severely reduce the acceptable entry corridor for a Saturn probe. The entry corridor is important because it provides the limit between the peak heat flux and skip conditions. The heat flux constraint already limits steeper entry flight path angles, but the skip condition constrains the shallower entry flight path angles. Saturn skip conditions generally limit the entry angle to steeper than -10.5^o, but -12^o was used in order to accommodate a margin of safety.

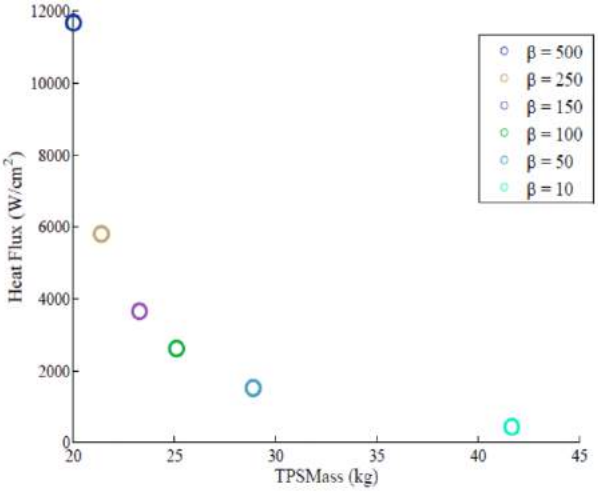

Figure D.4: HEEET TPS mass analysis. Ballistic coefficients range from 10 to 500 kg/m^2.

In order to design a probe which could meet the desired constraints above, the ballistic coefficient was used as the primary design variable in the

trajectory simulation. The total mass was also specified, but all other vehicle parameters were either constants, (coefficient of drag & nose-to-base ratio), or were determined from the ballistic coefficient. Using a range of ballistic coefficients at a midrange entry angle, it was easy to see where the peak stagnation point heat flux was below 7000 W/cm^2 and the point of diminishing returns in terms of TPS mass. Based on this analysis and further trajectory testing, using the entire entry parameter range provided by the mission design team, a ballistic coefficient of 220 kg/m^2 was selected to provide a large entry corridor while reducing TPS mass and satisfying the defined constraints. Using the equation for ballistic coefficient and the nose-to-base radius ratio, the nose radius and base radius of the probe were determined and are detailed in the main body of the report.

With these dimensions, the Saturn probe is slightly smaller in size than the *Galileo* atmospheric probe with a significantly lower mass penalty. The Saturn probe is also designed for a 30% margin of error from initial mass estimates as well as a higher safety margin in TPS material after the nearly full recession of the carbon phenolic on the edges of the *Galileo* probe. An option to further reduce the chance of failure due to recession of the TPS, the nose radius can be increased, thereby decreasing the peak stagnation heat flux. However, with the chaotic atmosphere of Saturn, the lower nose radius was chosen to increase stability at the expense of a higher peak heat flux. This increased stability is incredibly important for the safety of the probe during entry and the peak heat flux is taken into account in the definition of the entry corridor

With the initial probe design completed, the trajectory was iterated between the entry and mission design teams in order to determine on an acceptable range of entry parameters. In terms of EDL, the entry parameters provided by mission design were tested and used to converge on the entry corridor discussed earlier. This set of parameters is given in Table D.1 and was used to determine the TPS thickness and mass as well as the best design values for the probe.

Table D.1: Saturn entry parameters

Inertial Entry Velocity (km/s)	Latitude (deg)	Longitude (deg)	Heading Angle wrt North(deg)	Shallow Entry Flight Path Angle (deg)	Steep Entry Flight Path Angle (deg)
36.14	-0.926°	9.98°	116.33°	-12°	-19°

Using these parameters, the peak stagnation heat fluxes and total heat loads for the entry flight path range were determined through simulation and it was quickly apparent that HEEET would be necessary for such a mission to Saturn. The equation for cold wall convective heat flux at the stagnation point for Saturn entry was provided by Gary Allen of NASA Ames Research Center (Personal communication, 2016) and the radiative heat flux equation is an extrapolation from journal publications on the subject matter of outer planet entry conditions. This combination provides a close estimate to the current best model for stagnation point heat flux used in the NASA proprietary software

TRAJ and was verified using the Saturn HEEET study done by NASA Ames and presented at IPPW 13 (Ellerby et al., 2016).

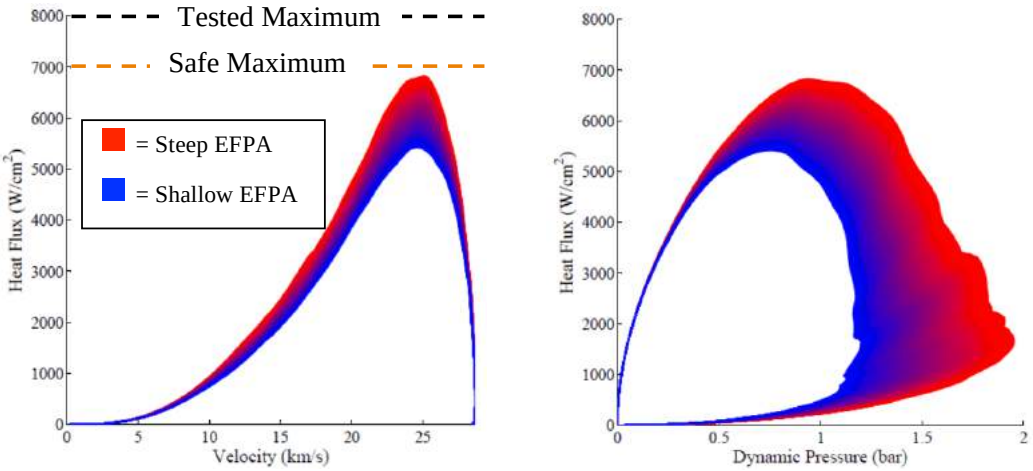

Figure D.5: Stagnation point cold-wall heat flux and dynamic pressure for Saturn entry corridor

$$\dot{q}_c = 1.07 \cdot 10^{-9} \rho^{0.5} R_n^{-0.5} V^{3.2} \quad \text{(D10)}$$

$$\dot{q}_r = 8.6237 \cdot 10^{-41} \rho^{1.763827469} R_n^{-0.17905} V^{10.99385} \quad \text{(D11)}$$

The total heat load at the stagnation point was calculated by integrating the heat flux equations over the course of the trajectory simulation. This heat load was then used to determine the front shell TPS mass by applying a relation between heat load and TPS thickness, then extrapolating the volume of the sphere cone shell with a decaying wall thickness to the edge of the probe. The thickness at the edge was determined using the value of half the total heat load at the stagnation point. By applying analogies to the *Galileo* probe, the TPS structure and back shell TPS were also determined.

Another point of interest during EDL design was the peak deceleration experienced by the probe. This variable is used in part to determine the size of the interior vessel as well as limiting the available science instruments. Due to this limitation, it was important to decrease the deceleration loads, optimally below 125 Earth g's. Being a point of high importance, this was investigated and the chosen corridor discussed earlier has a peak deceleration of just under 100 Earth g's for the steep case and decreases below 50 Earth g's as the shallow angle is approached.

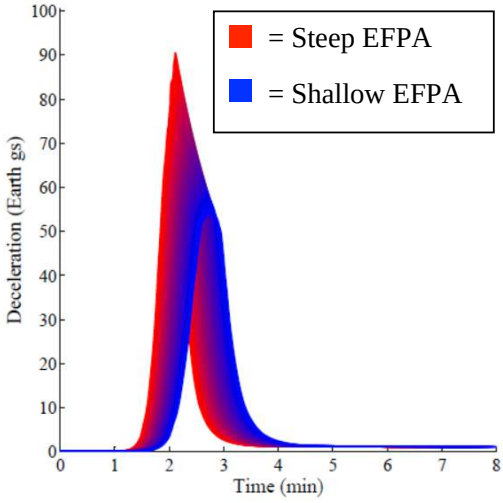

Figure D.6: Saturn Entry Deceleration Corridor

Uranus Entry and Descent

Uranus Properties & Constraints

One of the unique properties of Uranus is the highly tilted spin axis. In the launch date range considered, the spin axis would be pointed closely towards the Sun upon arrival. Thus, any approaches on the orbital plane would be oriented normal to the rotation of the planet. The approximately 2.6 km/s rotation would contribute a small factor to the total freestream velocity, especially due to the almost 90° approach angle relative to the rotation. However, one of the things to consider when performing any sort of maneuver close to Uranus and its rings. Due to the risk in damage to the spacecraft from materials in the ring, the probe must avoid the rings entirely, which invalidate many possible entry trajectories.

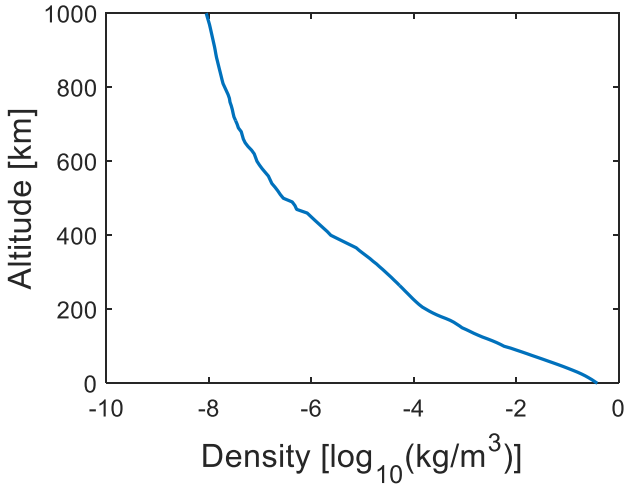

Figure D.7: Atmospheric density profile of Uranus. Note the log scale on the x-axis.

For Uranus atmospheric entry, the entry altitude was chosen to be 1000 km above the surface (defined as the radius as which the pressure is 1 bar). The model used is the Ames engineering model for Uranus (Agrawal et al., 2014). One of the biggest challenges with using this model is that there are large errors associated with it. Currently, there are no *in situ* measurements of the atmosphere – the only measurements have been by occultations. As Uranus is similar to Neptune, an assumption was made that the errors associated with the Neptune global atmosphere reference model would be similar to those errors for Uranus. Thus, the errors are approximately +750% to -90% density in the higher altitudes, to +240% to -70% in the lower altitudes.

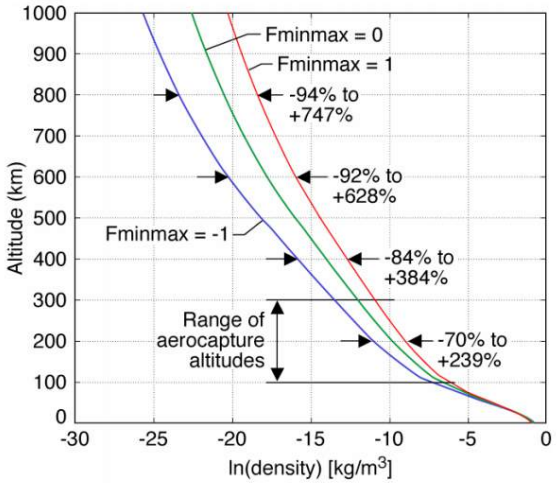

Figure D.8: Neptune atmospheric error (Lockwood et al., 2006).

Uranus Entry Probe Shell Design

A 45° sphere cone was chosen as the basic shape for the Uranus entry probe. Stability concerns, as well as *Galileo* leveraging the shape, determined that 45° would be necessary for the probe. The nose to base radius was 0.351, with the center of mass located in the fore section. For TPS material, HEEET was chosen due to the high heat rate values during entry, as well as the unavailability of carbon phenolic. Decreasing heat load, and thus decreasing TPS mass, became a goal for entry probe design. Using the limit of 7000 W/cm^2 for HEEET, the entry corridor with thermal constraints was determined.

The ballistic coefficient was used as a design variable for the trajectory simulation. Assuming a constant nose to base radius and cone angle, the ballistic coefficient was changed until a satisfactory mass and heat rate was found. Lower masses were found to be optimal, while there was a constraint on the maximum peak stagnation rate. Based on this analysis, the Uranus probe was selected to have a ballistic coefficient of 206 kg/m^2, with entry parameters of 19.8 km/s and -31.5°. A sensitivity analysis of ±3.5° was performed to see how much the heat rate would change due to entry angle error. The heat rate equations for convective and radiative fluxes are shown in Equations D12-D13.

$$\dot{q}_c = 3.638 \cdot 10^{-9} \rho^{0.4334341} R_n^{-0.5} V^{2.9978867} \quad \text{(D12)}$$

$$\dot{q}_r = 8.6237 \cdot 10^{-41} \rho^{1.763827469} R_n^{-0.17905} V^{10.993852} \quad \text{(D13)}$$

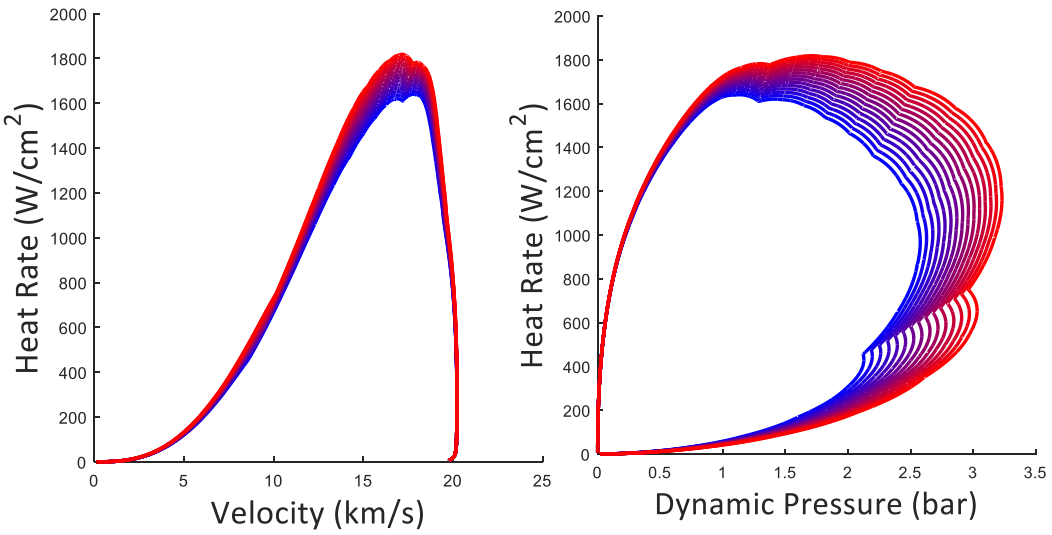

Figure D.9: Stagnation point cold-wall heat rate and dynamic pressure for Uranus entry

The heat load was then calculated by integrating the heat rates with the equations of motion. Heatshield sizing was then done using that heat load, by using a relation with heat load, TPS thickness, and location on the vehicle. The thickness of the TPS at the edges, as well as the backshell TPS and TPS structure were determined using the same methods as for the Saturn probe.

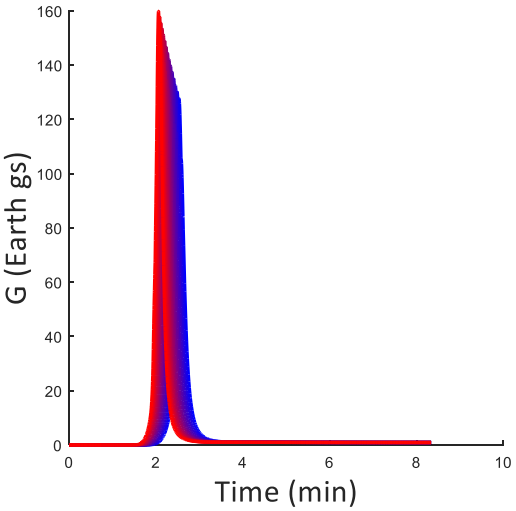

Figure D.10: Uranus entry deceleration corridor.

For peak deceleration, the load corresponds with the entry flight path angle. For shallower flight path angles, the deceleration is less severe. Due to the sensitivity of the instruments, the Earth g's experienced must be below their limit. For Uranus entry, the sensitivity analysis showed that the maximum load was 160 g's, while the minimum was slightly above 130 g's. These could theoretically be reduced with shallower entries, but the rings of Uranus become a major obstacle.

Instrument Protection Shell Design

In order to protect the science instruments after releasing the aeroshell, a spherical shell was designed to alleviate pressure and deceleration loads from the instruments. A spherical shell was chosen based on heritage systems used on *Pioneer Venus* as well as the inherent strength-to-mass efficiency of a sphere. To analyze different materials, a tool was built which determines the necessary thickness and mass of a particularly sized shell based on the maximum pressure and deceleration loads as well as material properties. The tool determines thickness using a model for thickness based on the material properties and allowable load defined by the pressure and deceleration. This model involves using equations for a pressure vessel as well as those for buckling of a hemispherical dome structure. Based on the analysis using this model, the optimal shell that can also house all of the science instruments is approximately 6 mm of titanium with an inner diameter of 46 cm. There are also small spin vanes attached to the outside of the probe for stability during descent after detaching from the TPS. This design provides protection for up to 30 bars of allowable external pressure and three times that for critical pressure and

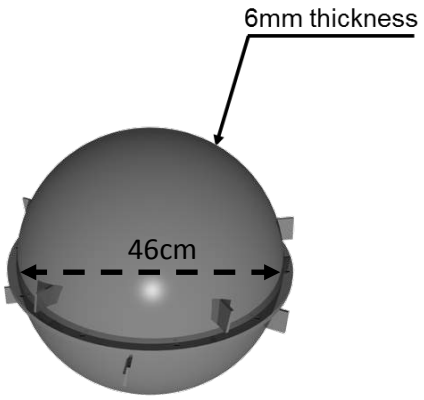

Figure D.11: Instrument protection shell.

deceleration loads of up to 200 Earth Gs. Based on the analysis for Saturn and Uranus EDL, this should provide protection for all expected circumstances.

TPS Design

For vehicles entering into atmospheres with orbital energies, a TPS system is required to prevent the vehicle from disintegrating. At the hypervelocity speeds the probes and aerocapture vehicle enter at, an ablative TPS material with a high resistant to heat is essential. For Saturn and Uranus entry, peak heat rates in the range of 2 to 8 kW/cm^2 and heat loads in the hundreds of kJ/cm^2 are observed. The only missions that have experienced aerothermal loads as high as that have been Venus missions and the *Galileo* probe. These missions used carbon phenolic as their TPS material. However, due to manufacturing issues, carbon phenolic is not an option for future missions. Current state-of-the-art technology uses phenolic impregnated carbon ablators (PICA), as seen on *Stardust* and the *Mars Science Laboratory*. However, PICA only can withstand peak heat rate of approximately 1 kW/cm^2. Thus, for these vehicles, the OCEANUS team considered the use of Heatshield for Extreme Environment Entry Technology (HEEET), a woven rigid TPS material impregnated with phenolic being developed at NASA Ames (Ellerby et al., 2016).

To calculate the mass of the heat shield, a first-order approximation was used to calculate the thickness required for HEEET. Assuming that the heat rate is high enough to cause the material to recess, the thickness required per unit heat load is calculated. Equations D14-D15 show the empirical correlation.

$$t_{required} = C\, Q_{actual} \tag{D14}$$

$$C = \frac{\rho_{a,exp}}{Q_{exp}} \tag{D15}$$

For HEEET, the coefficient C is approximately 1.2×10^{-5} cm^3/J. It quickly became clear that for Saturn and Uranus, HEEET would be the only option due to the high heat flux values experienced during entry and the unavailability of carbon phenolic. In the case of entry, the goal is to minimize the total heat load and thereby minimize the TPS mass requirement while also satisfying the peak heat flux constraint of HEEET. Based on the IPPW13 *Heatshield for Extreme Entry Environment Technology (HEEET) Development Status* presentation by Don Ellerby of NASA Ames Research Center (2016), the maximum tested value of stagnation point heat flux was 8000 W/cm^2 and their simulation for Saturn entry was limited to a stagnation point heat flux of 7000 W/cm^2. For consistency and validation, this same limit of 7000 W/cm^2 was also used for this analysis of entry and aerocapture trajectories.

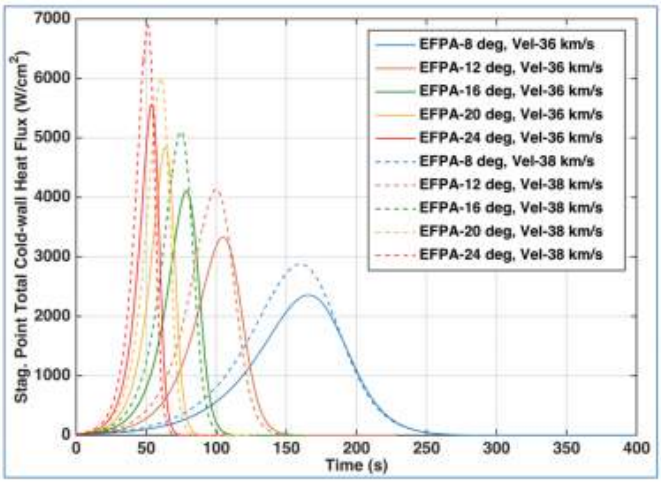

Figure D.12: NASA Ames Saturn entry stagnation point cold-wall heat flux analysis for HEEET TPS (Ellerby et al, 2016).

Terminal Descent Design

A trade study between the descent duration, maximum g load with parachute deployment altitude, and parachute size was done, as shown in Figure D.13. This trade study only assumes a single parachute for descent. Generally, increasing the deployment altitude increases the peak G load, and increases the parachute size increases the g load and descent duration. With a sequence of two parachutes, a maximum g load of an order of magnitude lower can be achieved. A sequence of two parachutes can ensure the separations of front shell and back cover from the pressure vessel. The pilot chute is sized at a reference diameter of 1.95 m to ensure the back cover can be removed reliability and the main parachute is sized at a reference diameter of 3.1 m to ensure the descent duration for science phase.

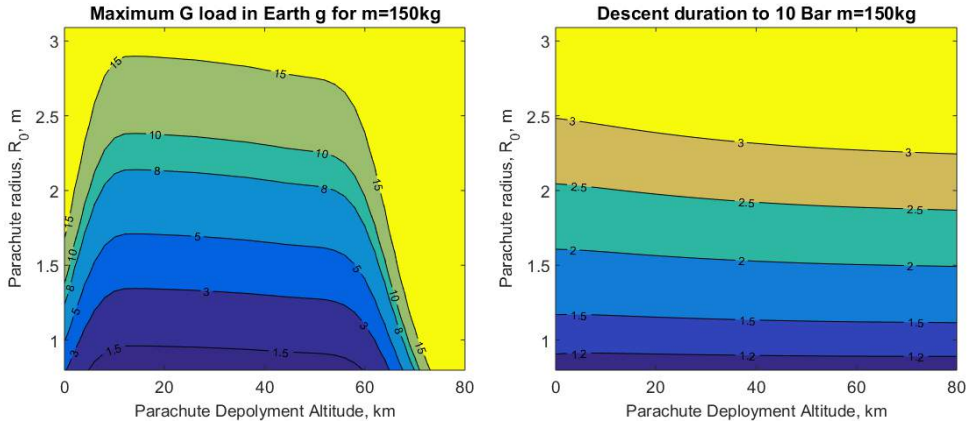

Figure D.13: Maximum G load experienced by the probe and descent duration to 10 bar with a nominal mass of 150kg at a range of pilot chute deployment altitudes and parachute reference radius.

Appendix E – Trajectory Trade Studies

Ballistic and Impulsive Trajectories

At the beginning of the concept study, the entire solution space from 1/1/2023-12/31/2037 was investigated in JPL-Purdue's STOUR software. This software performs a grid search for given gravity assist paths. This grid search is exhaustive for ballistic trajectories and also provides chemical impulsive trajectories that do not exceed a user-specified ΔV constraint. Under certain rules (e.g. after performing a gravity assist at an outer planet the spacecraft does not return to an inner planet) an exhaustive search was conducted for up to three flyby bodies and an array of four and five flyby body combinations were chosen based on previous results, publications, and flown missions.

This grid search yields a fairly comprehensive view of the solution space for a mission to Uranus over the given launch date range which greatly informed the point design conducted in this study. The data from STOUR is analyzed using software called STOUR Utility, developed at Purdue. This software allows for the comparison of every gravity assist path on the same plot; an ability which greatly aids the mission design process. The output from STOUR Utility is shown below in Figure E.1.

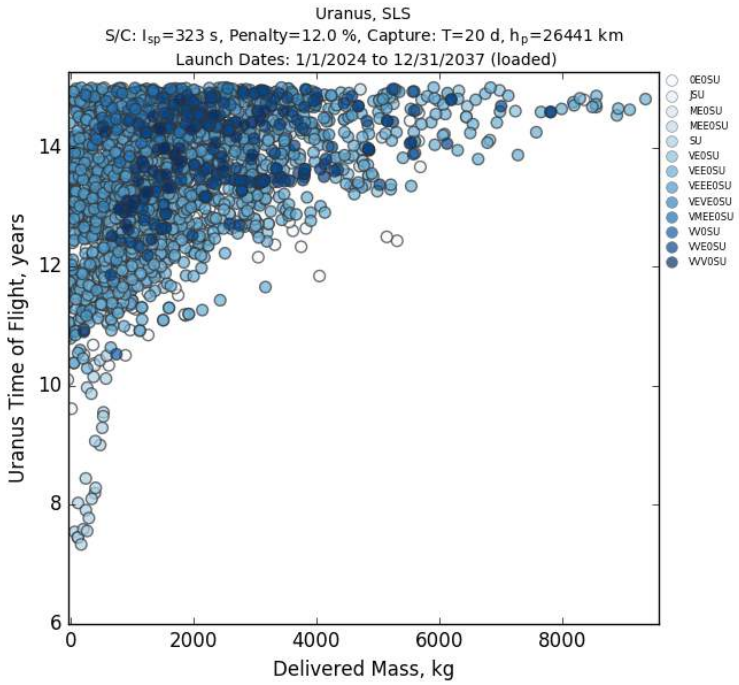

Figure E.1: Plot of time of flight as a function of the delivered payload. This data is for the SLS Block 1B launch vehicle and shows every trajectory reported by STOUR which travels to Uranus and includes a Saturn flyby.

Each point in Figure E.1 is an individual trajectory. This figure shows the entire solution space for trajectories using the SLS Block 1B launch vehicle. For all chemical maneuvers, a specific impulse of 323 seconds is assumed along with a 12% mass penalty to account for tanks and other structures. These assumptions create the delivered mass estimates, post-capture, shown in E.1.

For this study, two trajectories were selected out of this database of trajectories. They are summarized in Table E.1 below.

Table E.1: Selected trajectories for this dual planet flagship mission opportunity.

Path	Launch Vehicle	Launch Date	Launch V_∞ (km/s)	Launch Mass (Mg)	Time of Flight (yrs)	Uranus Arrival V_∞ (km/s)	Delivered Payload (Mg)
0E0SU	SLS Block 1B	9/13/2028	7.01	16.6	10.5	8.90	2.2
SU	SLS Block 1B w/Star 48B	7/3/2028	11.00	3.8	11.6	5.01	2.6

Each 0 in the 0E0SU path represents an impulsive maneuver and this case makes use of a 3:1 Earth-Earth resonance orbit for a ΔV-EGA maneuver. The 0E0SU case was initially the case of interest for this study, but was proven infeasible for the Saturn flyby. The flyby distance at Saturn for this case is over 5 million kilometers, which posed a great challenge for communicating with the probe as well as requiring an excessive amount of fuel for the deflection maneuver after releasing the probe. Lastly, this trajectory passes ahead of Saturn and a line of sight between the orbiter and the probe cannot be maintained. This is illustrated in Figure E.2.

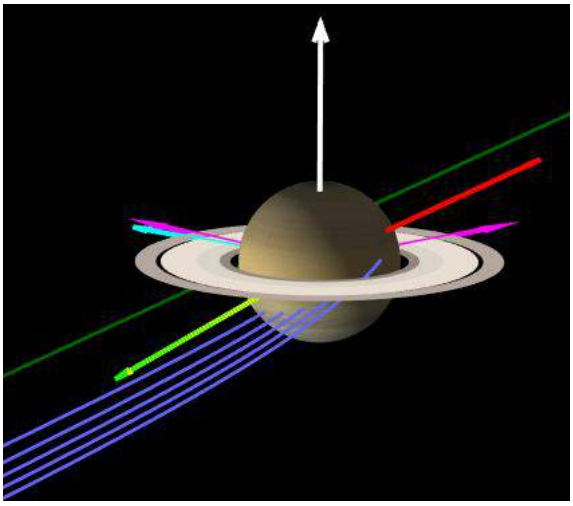

Figure E.2: Possible probe trajectories (blue) and the orbiter trajectory (green) for the 0E0SU case.

Figure E.2 clearly shows the orbiter passing on the other side of the planet as the probe enters. Even if the communications distance and deflection maneuver were not problematic, the failure to maintain a line of sight between the probe and the orbiter made this trajectory infeasible to fly. For this reason, the ballistic SU case was chosen as the chemical impulsive trajectory option for this study. Along with chemical trajectories, low thrust trajectories were also investigated.

Low Thrust Trajectories

While the OCEANUS mission uses the SLS with a STAR 48 booster, there is no guarantee the SLS will be ready by the designed launch date. Since the SLS is still in development—and faces the possibility of cancellation for a variety of reasons—it makes sense to have a secondary option available for use in the event the SLS is unavailable. The Atlas V 551 launch vehicle can deliver a reduced-mass mission to Uranus orbit; however, a Solar Electric Propulsion (SEP) system is required as chemically-propelled ballistic trajectories cannot deliver more than a few hundred kilograms in the best cases. Our analysis determined 10 cases which would be viable, and of those only 3 met all the requirements for the mission.

The search for Atlas V 551 SEP trajectories was carried out with the help of JPL's Mission Analysis Low-Thrust Optimizer (MALTO) tool. MALTO allows users to input spacecraft mass, power, and thrust properties as well as constraints on trajectory variables, such as fly-by altitudes, bodies, and times. The following presents a summary of the range of user inputs given to MALTO for this study.

Two power options were investigated for the Atlas V 551: one option assumed a 28 kW power supply with 4 NEXT engines, and the other a 40 kW power supply with 6 NEXT engines. The SEP system for the 28 kW option is assumed to be 1,056 kg, which accounts for solar panels, NEXT engines, and fuel tanks. For the 40 kW option, the SEP system is assumed as 1400 kg. Both options are assumed to have a $1/r^2$ power decrease where r is the distance from the Sun.

The release of two probes—one at Saturn and one at Uranus—is a priority for the Atlas V 551 missions; therefore, only trajectories which flew by Saturn on the way to Uranus were considered. The investigation assumed a 300 kg probe and a 1056 kg SEP system dropped at Saturn, as well as a 300 kg probe is dropped 130 days before Uranus arrival.

While hundreds of trajectories were investigated for SEP cases, only 10 solutions converged with enough confidence to report. Though the number of solutions was not large, it provided a baseline knowledge of available SEP trajectories using the Atlas V 551. Table E.2 shows 8 of the most promising solutions.

Table E.2: Candidate low-thrust trajectories using a combination of the Atlas V551 launch vehicle and an SEP stage.

Path	Launch Date	Arrival Date	Launch Mass (Mg)	Arrival Mass (Mg)	Time of Flight (yrs)
ESU	3/31/2024	4/2/2037	4.8	1.9	13.0
ESU*	4/4/2024	5/22/2034	5.2	1.2	10.1
ESU*	4/7/2024	6/29/2035	5.2	1.5	11.2
ESU	4/8/2024	5/26/2034	4.8	1.2	10.1
ESU	4/9/2024	3/23/2035	4.8	1.5	11.0
VEESU	1/19/2025	9/8/2036	5.4	0.95	11.6
VSU*	5/10/2027	10/28/2038	5.4	1.3	11.5
ESU	5/27/2027	12/10/2037	4.7	1.6	10.6

Of these 8 cases, only a few could provide the requisite mass for OCEANUS, and as exemplified by the ESU case launching on 3/31/2024, the time of flight is increased as arrival mass is increased. Additionally, given a maximum RTG lifetime of 15 years (including 3 years of pre-launch storage) the time of flight cannot be greater than 13 years when allowing for a 2-year science mission. In conclusion, OCEANUS must be moderately to severely descoped if an Atlas V 551 or similar launch vehicle is required.

Aerocapture Trajectories

For aerocapture, this study considered both chemical and low thrust trajectories. From the paper “Broad Search and Optimization of Solar Electric Propulsion Trajectories to Uranus and Neptune” by Landau, Try, and Strange, this study assumed a 50% TPS mass fraction when selecting interplanetary trajectories for aerocapture. With the delivered masses possible for SEP with an Atlas V 551, it is apparent that such a trajectory would not be sufficient for aerocapture. For this reason, the trajectories considered here are all chemical trajectories with the SLS Block 1B. The chosen trajectory is summarized below in Table E.3

Table E.3: Chosen trajectory for aerocapture architecture.

Path	Launch Date	Launch V_∞ (km/s)	Launch Mass (Mg)	Time of Flight (yrs)	Uranus Arrival V_∞ (km/s)	Delivered Payload (Mg)
VEE0SU	6/24/2026	8.54	15.8	9.11	12.8	2.5

This case was chosen based on a few criteria. The database of trajectories shown in Figure E.1 was searched for cases with high arrival V_∞ at Uranus, short time of flight, and a delivered payload of at least 2 metric tonnes. For this study, this was the only aerocapture trajectory considered due to time constraints. That being said, the entry

conditions at Uranus proved to be sub-optimal for this trajectory and a better case in the database of trajectories likely exists.

Appendix F – Telecommunications

Ground System

The ground system used for the tracking and communication with the OCEANUS spacecraft will be the deep space network (DSN). The DSN is composed of multiple 34-m and 70-m diameter antennas across three sites in Goldstone (USA), Madrid (Spain) and Canberra (Australia). The 70-m diameter antennas are reserved for high-priority missions and emergences and were not considered in this report.

34-m DSN Antenna

The DSN's 34-m diameter antennas are divided into High Efficiency (HEF) and Beam Wave-Guide (BWG) antennas. The HEF are more conventional antennas that do not support Ka-band operations and so they are not studied here (Slobin et al., 2014). The antennas that are studied are the BWG antennas, regrouping DSS-63,65,54,55 in Spain, DSS-24,25,26,14,15 in the USA and DSS-43,45,34,35 and soon to be DSS-36 (end of 2016) in Australia (Slobin et al., 2015). Only some of the antennas at the three DSN sites are able to support the reception of frequencies in the Ka-band: DSS-54, DSS-55 in the USA, DSS-25 and DSS-26 in the USA and DSS-34 and DSS-35 in Australia. Even so, DSS-25 presents some limitations to the reception of the Ka-band, as it is not possible to receive left-circularly polarized Ka-band. This can be a limiting factor and even though DSS-25 will be considered in the study, it might not be a viable DSN antenna for the ground system.

X-band/Ka-band DSN Antennas and their specifications

The DSN antennas' characteristics that allow X and Ka-band communications are presented in Table F.1. The table shows that the attenuation and the operating system noise temperature (T_{op}) are highly variable depending on the antenna selected. As at least one antenna per site will be used, the maximum attenuation and system noise temperatures in the table were used in subsequent analyses. The table also confirms the need to use 7.2 GHz for uplinks to the orbiter, as it is the X-band frequency range coherent with deep space Ka-band.

Table F.1: Specifications of DSN antennas appropriate for OCEANUS communications.

DSN Antenna	X-band freq. range coherent with Ka-band (MHz)	Pointing Loss of Receiver (dB)	Receiving Range (MHz)	Maximum T_{op} for X-band (K)	Wind Gain Reduction (dB)	Atmospheric Attenuation at Zenith (dB)	Maximum T_{op} for Ka-band (K)
Goldstone							
DSS 25	7149.6-7234.6	0.1	31800-32300	49.92	0.8	0.26	46.97
DSS 26	7149.6-7234.6	0.1	31800-32300	21.33	0.8	0.26	35.99
Madrid							
DSS 54	7149.6-7234.6	0.1	31800-32300	23.52	0.8	0.36	38.28
DSS 55	7149.6-7234.6	0.1	31800-32300	23.03	0.8	0.36	35.26
Canberra							
DSS 34	7149.6-7234.6	0.1	31800-32300	20.30	0.8	0.40	37.33
DSS 35	7149.6-7234.6	0.1	31800-32300	22.04	0.8	0.40	31.40
DSS 36	Under Construction						

DSN Coverage

A single DSN antenna alone cannot be used to perform all downlink and uplink operations with OCEANUS. The following figure represents the visibility of the three sites for DSS-26, DSS-34, and DSS-54, using the Spacecraft Visibility Plotter and Horizon Mask Plotter program provided by JPL (Jet Propulsion Laboratory, 2015).

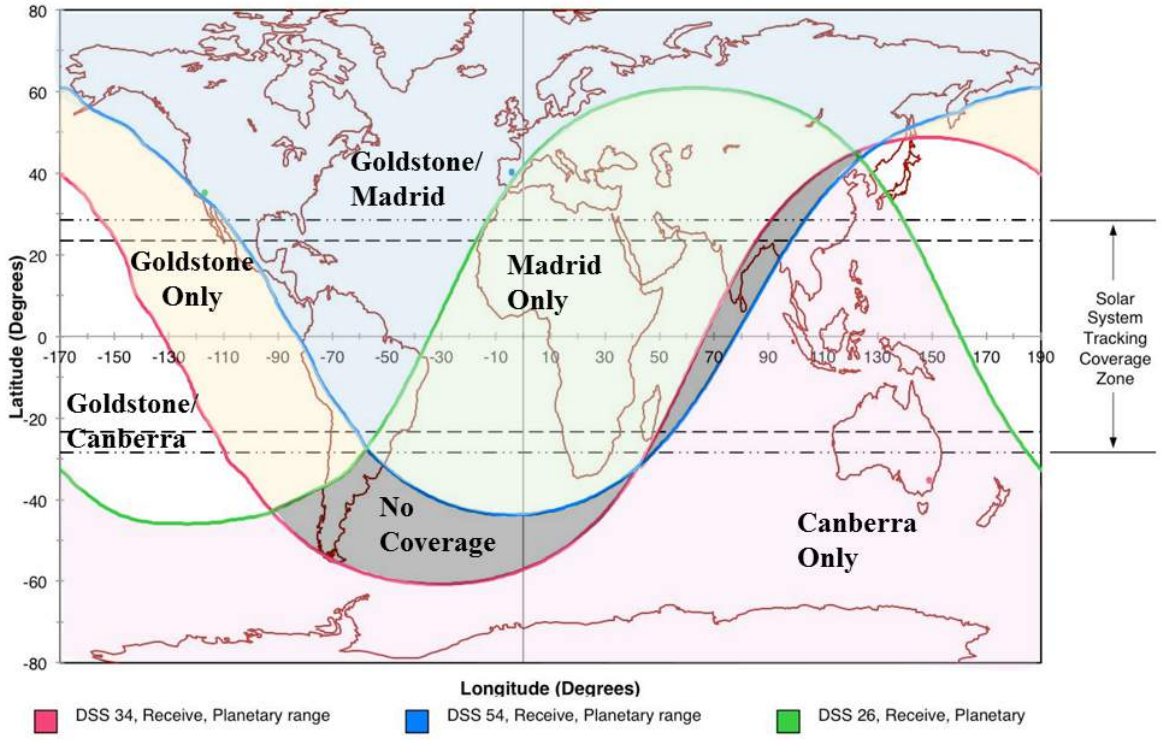

Figure F.1: DSN 34-m BWG antennas transmit coverage to planetary spacecraft using DSS 26, 34, and 54 (Jet Propulsion Laboratory, 2015).

Additional Hardware Details

Small Deep Space Transponder

A deep space transponder is a unit that is able to transmit and receive multiple frequencies and is resistant to radiation, making it ideal for deep space missions. Based on *Juno's* heritage, OCEANUS uses a Small Deep Space Transponder for reliable X-Band and Ka-Band Deep Space Transmission (Mukai et al., 2012; Verderame and Stiller, 2015). The telecommunication system will be able to transmit in the Ka-band, and transmit or emit in the X-band. With a nominal power of 19.5 W when used for both X-band and Ka-band, the Small Deep Space Transponder will weigh only 3.2 kg, for the following volume: 18.1 cm (L) x 16.6 cm (W) x 11.4 cm (H). Figure F.2 illustrates the Small Deep Space Transponder unit.

Figure F.2: Small Deep Space Transponder (Verderame and Stiller, 2015)

TWTA Ka-band

The Traveling Wave Tube Amplifier (TWTA) for X-band is based upon *Lunar Reconnaissance Orbiter* heritage (NASA Glenn, 2008). As part of the telecommunication system, a TWTA is used to amplify the radio frequencies (RF) in the microwave range, enabling OCEANUS' HGA, MGA and LGA to communicate from deep space to Earth.

The TWTA will use 100 W power output to provide 40 W transmitted power for the HGA at the 32 GHz Ka-band frequency. This TWTA will be based on the L3-EIT 999H TWTA Ka-band that only weighs 1.495 kg for a volume of 35.8 cm x 8.9 cm x 6.9 cm and an efficiency of 0.6 at 32 GHz (Robbins et al., 2006; Space LTWTA Products, 2016). Figure F.3 provides an image of the TWTA used for the LRO.

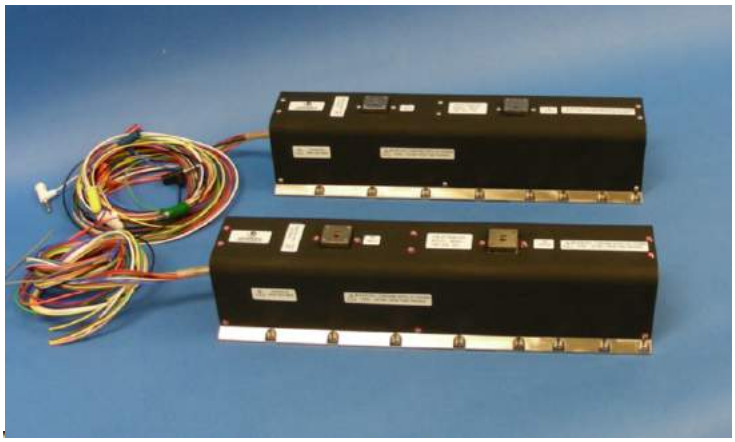

Figure F.3: TWTA used on LRO (NASA Glenn, 2008)

TWTA X-band

The Traveling Wave Tube Amplifier (TWTA) for X-band is based on heritage of the *Solar Terrestrial Relations Observatory* (STEREO) mission (Mukai et al., 2012). With a RF output of 60 W, we might expect up to 120 W of consumption. The

dimensions of the TWTA used in this study are based on L-3 Communications data (LTWTA Products, 2016). Thus, the TWTA will be 37.1 cm x 7.6 cm x 8.1 cm and weighs 0.965 kg. The TWTA for X-band is very similar to the TWTA for Ka-band in terms of appearance.

Waveguide Transfer Switch

A waveguide transfer switch is an electrical switch that changes the path of the electric wave between several sources. Here, the different waveguide depends on the frequency expected of the electric signal. The switch here is directly based on *Juno* heritage (Mukai et al., 2012). The switch weighs only 0.44 kg for dimensions of approximately 5 cm x 5 cm x 10 cm. Figure F.4 illustrates the waveguide transfer switch.

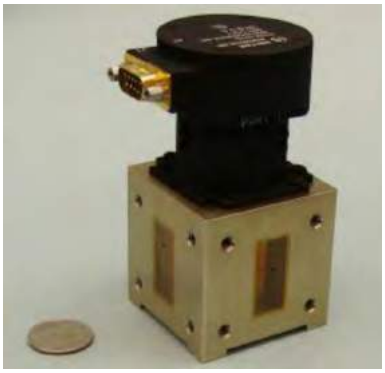

Figure F.4: Waveguide transfer switch used in *Juno's* telecommunication system (Mukai et al., 2012).

Diplexer

A Diplexer is one of the few passive systems in the telecommunication system. It connects the receiver, transmitter, and antenna. Its main objective is to emit from the antenna at one frequency with a strong signal (such as Ka-band), while still receiving weak signal from Earth at a different frequency (such as the X-band). The Diplexer used in this study is directly inherited from *Juno* heritage. The diplexer would need to be able to transmit in the Ka-band and receive in the X-band. The dimensions of the diplexer are similar to the Ka-band waveguide. The diplexer assembly for the *Dawn* mission is pictured in Figure F.5.

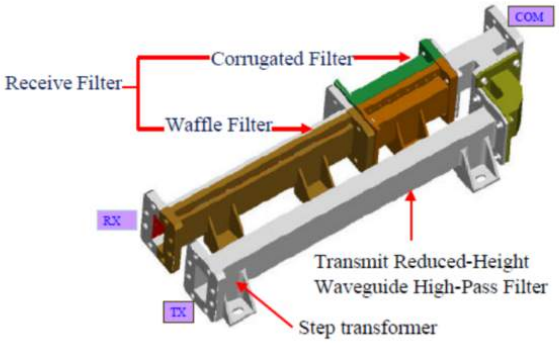

Figure F.5: Diplexer assembly for the *Dawn* spacecraft (Taylor, 2009).

Isolator

An isolator is an electronic component of the telecommunication system made of ferrite that helps limit the signal loss in one direction while providing isolation and protection in the other direction. Here, the isolator selected is a direct heritage from the *Juno* spacecraft (Mukai et al., 2012). Such isolators are small, weighing only 0.55 kg for *Juno*. Several isolators are pictured in Figure F.6 and have volumes of roughly 16 cm^3.

Figure F.6: Isolators for X-band or Ka-band telecommunication systems (DiTom Microwave Inc., 2016).

System Noise Temperature for Probe-Orbiter Relay

The System Noise Temperature of the probe-to-orbiter relay link will depend on the temperature of Uranus and Saturn. It is possible to define the operating System Noise Temperature (SNT) to be (Slobin et al., 2016),

$$T_{op} = T_{Ant} + T_{sky} \tag{F1}$$

where T_{op} is the System operating noise temperature, T_{Ant} is the Antenna noise contribution, and T_{Sky} is the sky noise contribution. The sky noise contribution is composed of the sum of the atmospheric temperature T_{Atm} and the cosmic background noise temperature T_{Cosmic}.

To define T_{Atm}, first define the atmospheric loss factor,

$$L = 10^{A/10} \tag{F2}$$

where A is the atmospheric attenuation in dB. Then, T_{Atm} can be defined as,

$$T_{Atm} = T_p\,[1 - \frac{1}{L}] \tag{F3}$$

where T_p is the physical temperature of the atmosphere. Saturn's mean temperature at 10 bars pressure can be approximated at 220 K (Williams, 2015), and 200 K for Uranus (Williams, 2016). Furthermore, the atmospheric attenuation of Saturn at 10 bars is assumed to be 2.03 dB and 9.48×10^{-3} dB for Uranus (David et al., 2016).

Finally, the contribution of the cosmic microwave background to the noise temperature is,

$$T_{cosmic} = \frac{T_{CMB}}{L} \tag{F4}$$

with T_{CMB} the cosmic microwave background noise temperature, which is 2.725 K (Slobin et al., 2015).

Thus, the following equivalent system noise temperatures for the entry probe data relay at Uranus and Saturn were obtained. Note that the temperature of the probes' MGA antenna is assumed to be 100 K. This assumption is based on an approximation of the physical temperature of the patch array antenna on the probes during descent (Ball et al., 2007).

Table F.2: System noise temperatures of Saturn and Uranus for a probe penetrating to a depth of 10 bars pressure.

T_{atm} Uranus (K)	T_{cosmic} Uranus (K)	T_{atm} Saturn (K)	T_{cosmic} Saturn (K)	T_{ant} (physical temperature) (K)	Total SNT Uranus (K)	Total SNT Saturn (K)
0.43	2.72	82.14	1.71	100	103.15	183.85

Link Budget Optimization Tool

In order to provide an estimation of an optimized configuration for each communication link, an excel tool was developed using the solver GRG Nonlinear

method. The tool was used to optimize antenna size, transmitter power, and the data rate for each potential link from the orbiter to Earth and from the probe to the orbiter.

Presentation of Tool

The Excel program developed in this study was used to optimize either the diameter of the receiving antenna, diameter of the transmitting, the data rate of transmission, or the transmitted power output. There are many mission specific inputs, but the key inputs that affect the system the most are: the antenna efficiencies (affecting the antenna gain), the frequency (affecting antenna gain, space loss, and atmospheric attenuation), the range (affecting space loss), and the system noise temperature (affecting the noise spectral density). By setting maximum constraints on the antenna sizes and transmitted power, and placing minimum constraints on the data rate and E_b/N_o margin, it was possible to quickly optimize the OCEANUS telecom system utilizing Excel solvers' GRG Nonlinear method (minimizing E_b/N_o margin). A screenshot of the tool is shown in Figure F.7.

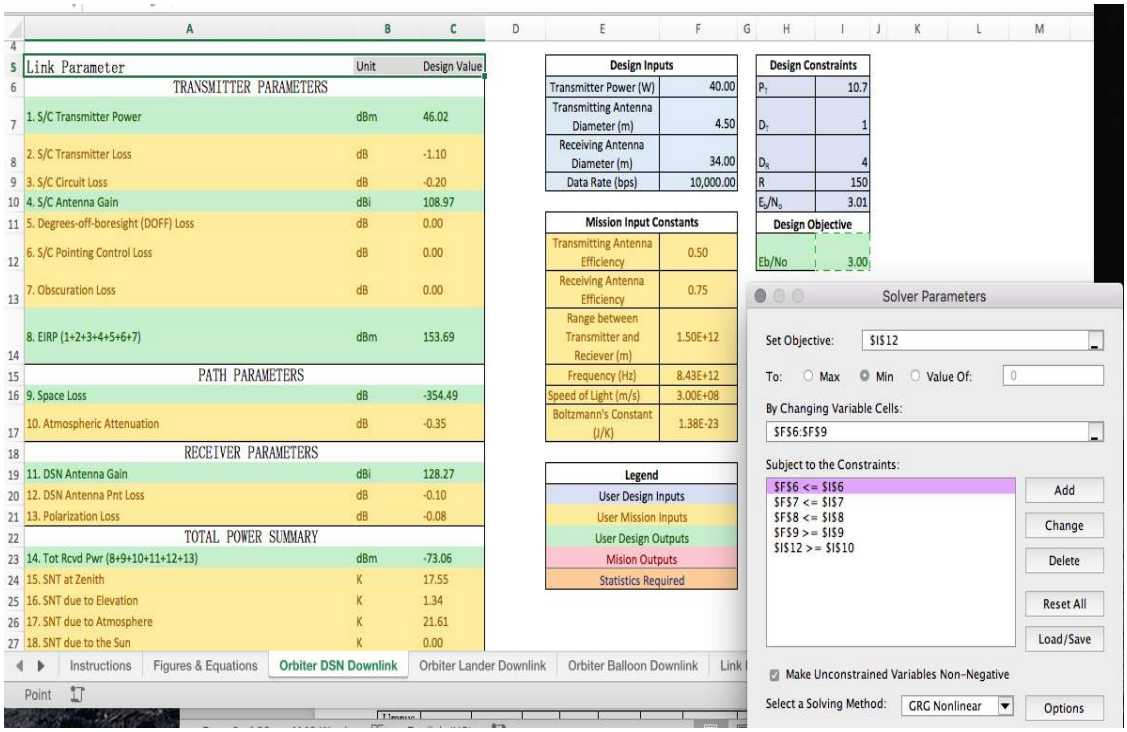

Figure F.7: Screenshot of link budget optimization tool

Application to HGA for Earth-Orbiter communication

The optimization tool for the HGA budget link was used to inform the design of OCEANUS' HGA. The inputs used were a 34-m diameter DSN antenna and a transmitted power of 40 W from the spacecraft for Ka-band at 32GHz (based on heritage). The System Noise Temperature and the different losses came from the *Cassini-Huygens* DESCANSO (Taylor et al., 2002). The range from the DSN antenna used was 3.05 billion km, which is the maximum distance between Uranus and Earth. The efficiency for the DSN antenna was 0.74, while it was 0.6 for the HGA. The minimum data rate used was 34 kbps in order to enable transmission of send several copies of the orbiter data to Earth.

Application to MGA for Earth-Orbiter communication

The MGA is expected to deliver information to the DSN from the orbiter for instrument checkouts and engineering data. Therefore, only a 948 bps of downlink to the DSN antenna of 34-m diameter is expected. The efficiency of the MGA is expected to be 0.6, for a transmitted power of 60 W in the X-band, at a frequency of 8.425 GHz, and at a range of 3.05 billion km.

Application to LGA for Earth-Orbiter communication

The LGAs are used at a distance of up to 1.5 AU for instrument checkouts, and can always be used thereafter that for emergency cases. The efficiency of the LGA is expected to be 0.6, with a data rate of 948 bps at up to 1.5 AU, at a frequency of 8.425 GHz in the X-band.

Application to Saturn Probe Relay Link

A relay-link between the probe and the orbiter using the HGA with a UHF frequency at 405MHz was used to limit the effect of attenuation at Saturn. The patch array MGA on the probe cannot be larger than 0.6 m diameter due to dynamic pressure constraints following the jettison of the aeroshell. The patch array antenna is expected to have an efficiency of 0.5 for a maximum range of 1.62 million km to the orbiter HGA. The output power of the patch array is limited here to 10.7 W, which is the power output of the Electra-lite UHF transceiver. The constraints and system noise temperature were inherited from a relay-link budget study for Venus (Ball et al., 2007). The system noise temperature specific to Saturn has been calculated in Table F.2.

Application to Uranus Probe Relay Link

The relay-link between the probe and the orbiter at Uranus is less restrictive due to the fact that the orbiter is closer to the probe during its entry. The range is only 155,000 km. Moreover, the attenuation due to the Uranus' atmosphere is assumed to be similar to Neptune and thus smaller than on Saturn.

Conclusion for the system design

After running all the cases with the inputs as previously described, a choice was made for the size of the various antennas on OCEANUS. The results of the optimization process are presented in Table F.3. For the HGA, a diameter of 4 m must to be used, as Saturn is the limiting case with the need for a 3.82 m diameter antenna. Additionally, a 0.8 m diameter MGA is required along with 0.06 cm diameter LGAs. Note that a margin of 0.5 dB Eb/No was used for every antenna save for the MGA.

Table F.3: Optimal sizes and characteristics of the OCEANUS communication antennas.

Antenna	Diameter (m)	Receiving Antenna Diameter (m)	Data Rate 9bps)	Range (km)	Frequency [(z)	Efficiency	Trans-mitted Power (W)
HGA	1.91	34	34,000	3.05×10^{9}	3.20×10^{10}	0.6	40
LGA	0.06	34	948	2.25×10^{8}	8.43×10^{9}	0.6	60
MGA	0.8	34	948	3.05×10^{9}	8.43×10^{9}	0.6	60
Saturn Probe	0.6	3.82	200	1.62×10^{6}	4.05×10^{8}	0.5	10.7
Uranus Probe	0.6	0.2	200	1.55×10^{5}	4.05×10^{8}	0.5	10.7

Link Budget Design Control Tables

Tables F.4-F.8 analyze the signal-to-noise ratio per bit for each of OCEANUS' planned downlink paths. Namely, the HGA, MGA, and LGAs to Earth, and the patch MGA of the probes to the orbiter. The tables are presented in the format of DESCANSO reports.

HGA Downlink from Uranus

Table F.4: Downlink DCT (34-m BWG, HGA, Ka-band (32-GHz), Range 3.05E+9 km)

Link Parameter	Unit	Design Value
TRANSMITTER PARAMETERS		
1. S/C Transmitter Power	dBm	46.02
2. S/C Transmitter Loss	dB	-1.10
3. S/C Circuit Loss	dB	-0.20
4. S/C Antenna Gain	dBi	60.33
5. Degrees-off-boresight (DOFF) Loss	dB	0.00
6. S/C Pointing Control Loss	dB	0.00

7. Obscuration Loss	dB	0.00
8. EIRP (1+2+3+4+5+6+7)	dBm	105.05
PATH PARAMETERS		
9. Space Loss	dB	-312.23
10. Atmospheric Attenuation	dB	-0.40
RECEIVER PARAMETERS		
11. DSN Antenna Gain	dBi	79.83
12. DSN Antenna Pnt Loss	dB	-0.10
13. Polarization Loss	dB	-0.08
TOTAL POWER SUMMARY		
14. Tot Rcvd Pwr (8+9+10+11+12+13)	dBm	-127.94
15. SNT at Zenith	K	46.97
16. SNT due to Elevation	K	0.00
17. SNT due to Atmosphere	K	0.00
18. SNT due to the Sun	K	0.00
19. SNT due to other Hot Bodies	K	0.00
20. System Noise Temperature (15+16+17+18+19)	K	46.97
21. Noise Spectral Density	dBm/Hz	-181.88
22. Received *Pt /N0* (14–21)	dB-Hz	53.94
CARRIER PERFORMANCE		
23. Recovered *Pt /N0* (22+[AGC+BPF])	dB	53.94
24. Telemetry Carrier Suppression	dB	-15.33
25. Ranging Carrier Suppression	dB	-0.16
26. DOR Carrier Suppression	dB	0.00
27. Carrier Power (AGC) (14+24+25+26)	dBm	-143.43
28. Received *Pc /N0* (23+24+25+26)	dB-Hz	38.45
29. Carrier Loop Noise BW	dB-Hz	4.77
30. Carrier Loop SNR (CNR) (28–29)	dB	33.68
31. Recommended CNR	dB	10.00
32. Carrier Loop SNR Margin (30–31)	dB	23.68
TELEMETRY PERFORMANCE		
33. Telemetry Data Suppression	dB	-0.13
34. Ranging Data Suppression	dB	-0.16
35. DOR Data Suppression	dB	0.00
36. DSN System Loss	dB	-0.80
37. Received *Pd/N0* (23+33+34+35+36)	dB-Hz	52.85
38. 2-Sigma *Pd /N0* (37–2*sqrt(37var))	dB-Hz	
39. Data Rate	dB-Hz	45.31

40. Available *Eb /N0* (37–39)	dB	7.54
41. Required *Eb/N0*	dB	0.31
42. *Eb/N0* Margin (40–41)	dB	7.23

MGA Downlink from Uranus

Table F.5: Downlink DCT (34-m BWG, MGA, X-band (8.425-GHz), Range 3.05E+9 km)

Link Parameter	Unit	Design Value
TRANSMITTER PARAMETERS		
1. S/C Transmitter Power	dBm	47.78
2. S/C Transmitter Loss	dB	-1.10
3. S/C Circuit Loss	dB	-0.20
4. S/C Antenna Gain	dBi	34.76
5. Degrees-off-boresight (DOFF) Loss	dB	0.00
6. S/C Pointing Control Loss	dB	
7. Obscuration Loss	dB	0.00
8. EIRP (1+2+3+4+5+6+7)	dBm	81.24
PATH PARAMETERS		
9. Space Loss	dB	-300.64
10. Atmospheric Attenuation	dB	-0.17
RECEIVER PARAMETERS		
11. DSN Antenna Gain	dBi	68.23
12. DSN Antenna Pnt Loss	dB	-0.10
13. Polarization Loss	dB	-0.08
TOTAL POWER SUMMARY		
14. Tot Rcvd Pwr (8+9+10+11+12+13)	dBm	-151.52
15. SNT at Zenith	K	46.97
16. SNT due to Elevation	K	0.00
17. SNT due to Atmosphere	K	0.00
18. SNT due to the Sun	K	0.00
19. SNT due to other Hot Bodies	K	0.00
20. System Noise Temperature (15+16+17+18+19)	K	35.88
21. Noise Spectral Density	dBm/Hz	-183.05
22. Received *Pt /N0* (14–21)	dB-Hz	31.53
CARRIER PERFORMANCE		
23. Recovered *Pt /N0* (22+[AGC+BPF])	dB	31.53
24. Telemetry Carrier Suppression	dB	-15.33
25. Ranging Carrier Suppression	dB	-0.16

26. DOR Carrier Suppression	dB	0.00
27. Carrier Power (AGC) (14+24+25+26)	dBm	-167.01
28. Received *Pc /N0* (23+24+25+26)	dB-Hz	16.04
29. Carrier Loop Noise BW	dB-Hz	4.77
30. Carrier Loop SNR (CNR) (28–29)	dB	11.27
31. Recommended CNR	dB	10.00
32. Carrier Loop SNR Margin (30–31)	dB	1.27
TELEMETRY PERFORMANCE		
33. Telemetry Data Suppression	dB	-0.13
34. Ranging Data Suppression	dB	-0.16
35. DOR Data Suppression	dB	0.00
36. DSN System Loss	dB	-0.80
37. Received *Pd/N0* (23+33+34+35+36)	dB-Hz	30.44
38. 2-Sigma *Pd /N0* (37–2*sqrt(37var))	dB-Hz	
39. Data Rate	dB-Hz	29.77
40. Available *Eb /N0* (37–39)	dB	0.68
41. Required *Eb/N0*	dB	0.31
42. *Eb/N0* Margin (40–41)	dB	0.37

LGA Downlink from Inner Cruise

Table F.6: Downlink DCT (34-m BWG, LGA, X-band (8.425-GHz), Range 2.25E+8 km)

Link Parameter	Unit	Design Value
TRANSMITTER PARAMETERS		
1. S/C Transmitter Power	dBm	47.78
2. S/C Transmitter Loss	dB	-1.10
3. S/C Circuit Loss	dB	-0.20
4. S/C Antenna Gain	dBi	12.26
5. Degrees-off-boresight (DOFF) Loss	dB	0.00
6. S/C Pointing Control Loss	dB	0.00
7. Obscuration Loss	dB	0.00
8. EIRP (1+2+3+4+5+6+7)	dBm	58.74
PATH PARAMETERS		
9. Space Loss	dB	-278.00
10. Atmospheric Attenuation	dB	-0.17
RECEIVER PARAMETERS		
11. DSN Antenna Gain	dBi	68.23

12. DSN Antenna Pnt Loss	dB	-0.10
13. Polarization Loss	dB	-0.05
TOTAL POWER SUMMARY		
14. Tot Rcvd Pwr (8+9+10+11+12+13)	dBm	-151.34
15. SNT at Zenith	K	46.97
16. SNT due to Elevation	K	0.00
17. SNT due to Atmosphere	K	0.00
18. SNT due to the Sun	K	0.00
19. SNT due to other Hot Bodies	K	0.00
20. System Noise Temperature (15+16+17+18+19)	K	35.88
21. Noise Spectral Density	dBm/Hz	-183.05
22. Received *Pt /N0* (14–21)	dB-Hz	31.71
CARRIER PERFORMANCE		
23. Recovered *Pt /N0* (22+[AGC+BPF])	dB	31.71
24. Telemetry Carrier Suppression	dB	-15.33
25. Ranging Carrier Suppression	dB	-0.16
26. DOR Carrier Suppression	dB	0.00
27. Carrier Power (AGC) (14+24+25+26)	dBm	-166.83
28. Received *Pc /N0* (23+24+25+26)	dB-Hz	16.22
29. Carrier Loop Noise BW	dB-Hz	4.77
30. Carrier Loop SNR (CNR) (28–29)	dB	11.45
31. Recommended CNR	dB	10.00
32. Carrier Loop SNR Margin (30–31)	dB	1.45
TELEMETRY PERFORMANCE		
33. Telemetry Data Suppression	dB	-0.13
34. Ranging Data Suppression	dB	-0.16
35. DOR Data Suppression	dB	0.00
36. DSN System Loss	dB	-0.50
37. Received *Pd/N0* (23+33+34+35+36)	dB-Hz	30.92
38. 2-Sigma *Pd /N0* (37–2*sqrt(37var))	dB-Hz	
39. Data Rate	dB-Hz	29.77
40. Available *Eb /N0* (37–39)	dB	1.15
41. Required *Eb/N0*	dB	0.31
42. *Eb/N0* Margin (40–41)	dB	0.84

Probe Relay Link at Saturn

Table F.7: Downlink DCT (4-m HGA, 0.6-m MGA, UHF (405-MHz), Range 1.62E+6 km)

Link Parameter	Unit	Design Value
TRANSMITTER PARAMETERS		
1. S/C Transmitter Power	dBm	40.29
2. S/C Transmitter Loss	dB	-0.30
3. S/C Circuit Loss	dB	0.00
4. S/C Antenna Gain	dBi	5.10
5. Degrees-off-boresight (DOFF) Loss	dB	0.00
6. S/C Pointing Control Loss	dB	0.00
7. Obscuration Loss	dB	0.00
8. EIRP (1+2+3+4+5+6+7)	dBm	45.10
PATH PARAMETERS		
9. Space Loss	dB	-208.78
10. Atmospheric Attenuation	dB	-2.03
RECEIVER PARAMETERS		
11. DSN Antenna Gain	dBi	22.37
12. DSN Antenna Pnt Loss	dB	-0.30
13. Polarization Loss	dB	-0.20
TOTAL POWER SUMMARY		
14. Tot Rcvd Pwr (8+9+10+11+12+13)	dBm	-143.84
15. SNT at Zenith	K	17.55
16. SNT due to Elevation	K	1.34
17. SNT due to Atmosphere	K	16.99
18. SNT due to the Sun	K	0.00
19. SNT due to other Hot Bodies	K	0.00
20. System Noise Temperature (15+16+17+18+19)	K	183.85
21. Noise Spectral Density	dBm/Hz	-175.96
22. Received *Pt /N0* (14–21)	dB-Hz	32.11
CARRIER PERFORMANCE		
23. Recovered *Pt /N0* (22+[AGC+BPF])	dB	32.11
24. Telemetry Carrier Suppression	dB	-6.00
25. Ranging Carrier Suppression	dB	0.00
26. DOR Carrier Suppression	dB	0.00
27. Carrier Power (AGC) (14+24+25+26)	dBm	-149.84
28. Received *Pc /N0* (23+24+25+26)	dB-Hz	26.11
29. Carrier Loop Noise BW	dB-Hz	200.00

30. Carrier Loop SNR (CNR) (28–29)	dB	-173.89
31. Recommended CNR	dB	10.00
32. Carrier Loop SNR Margin (30–31)	dB	-183.89
TELEMETRY PERFORMANCE		
33. Telemetry Data Suppression	dB	-1.20
34. Ranging Data Suppression	dB	0.00
35. DOR Data Suppression	dB	0.00
36. DSN System Loss	dB	-2.00
37. Received *Pd/N0* (23+33+34+35+36)	dB-Hz	28.91
38. 2-Sigma *Pd /N0* (37–2*sqrt(37var))	dB-Hz	
39. Data Rate	dB-Hz	23.01
40. Available *Eb /N0* (37–39)	dB	5.90
41. Required *Eb/N0*	dB	5.00
42. *Eb/N0* Margin (40–41)	dB	0.90

Probe Relay Link at Uranus

Table F.8: Downlink DCT (4-m HGA, 0.6-m MGA, UHF (405-MHz), Range 1.55E+5 km)

Link Parameter	Unit	Design Value
TRANSMITTER PARAMETERS		
1. S/C Transmitter Power	dBm	40.29
2. S/C Transmitter Loss	dB	-0.30
3. S/C Circuit Loss	dB	0.00
4. S/C Antenna Gain	dBi	5.89
5. Degrees-off-boresight (DOFF) Loss	dB	0.00
6. S/C Pointing Control Loss	dB	0.00
7. Obscuration Loss	dB	0.00
8. EIRP (1+2+3+4+5+6+7)	dBm	45.89
PATH PARAMETERS		
9. Space Loss	dB	-188.40
10. Atmospheric Attenuation	dB	9.48E-03
RECEIVER PARAMETERS		
11. DSN Antenna Gain	dBi	22.37
12. DSN Antenna Pnt Loss	dB	-0.30
13. Polarization Loss	dB	-0.20
TOTAL POWER SUMMARY		
14. Tot Rcvd Pwr (8+9+10+11+12+13)	dBm	-120.63

15. SNT at Zenith	K	17.55
16. SNT due to Elevation	K	1.34
17. SNT due to Atmosphere	K	16.99
18. SNT due to the Sun	K	0.00
19. SNT due to other Hot Bodies	K	0.00
20. System Noise Temperature (15+16+17+18+19)	K	103.15
21. Noise Spectral Density	dBm/Hz	-178.47
22. Received *Pt /N0* (14–21)	dB-Hz	57.84
CARRIER PERFORMANCE		
23. Recovered *Pt /N0* (22+[AGC+BPF])	dB	57.84
24. Telemetry Carrier Suppression	dB	-6.00
25. Ranging Carrier Suppression	dB	0.00
26. DOR Carrier Suppression	dB	0.00
27. Carrier Power (AGC) (14+24+25+26)	dBm	-126.63
28. Received *Pc /N0* (23+24+25+26)	dB-Hz	51.84
29. Carrier Loop Noise BW	dB-Hz	200.00
30. Carrier Loop SNR (CNR) (28–29)	dB	-148.16
31. Recommended CNR	dB	10.00
32. Carrier Loop SNR Margin (30–31)	dB	-158.16
TELEMETRY PERFORMANCE		
33. Telemetry Data Suppression	dB	-1.20
34. Ranging Data Suppression	dB	0.00
35. DOR Data Suppression	dB	0.00
36. DSN System Loss	dB	-2.00
37. Received *Pd/N0* (23+33+34+35+36)	dB-Hz	54.64
38. 2-Sigma *Pd /N0* (37–2*sqrt(37var))	dB-Hz	
39. Data Rate	dB-Hz	23.01
40. Available *Eb /N0* (37–39)	dB	31.62
41. Required *Eb/N0*	dB	5.00
42. *Eb/N0* Margin (40–41)	dB	26.63

Appendix G – Risk Analysis

Initial Assessment

In order to determine the major risks involved with the OCEANUS mission concept, each sub-team determined the most consequential risks involved with their respective systems as well as the likelihood of those risks to occur during the mission. These risks were then compared to each other, re-assessed with a ranking system, and organized into logistical and technical risks. Of these risk factors, the major risks were organized into a list of twelve with their category, type, likelihood, and consequences ranking for analysis of mitigation strategies.

Logistical Risks

Starting with logistical risks, the first major risk was cost overruns due to delay. This was assessed as a major risk due to the current state of the NASA budget system as well as previous evidence in the last decade of projects generally being delayed because the initial time estimate was too short. Instrument development as well as development of low TRL systems are the greatest source of this overrun, especially with NASA trying to keep costs as low as possible to accommodate the current budget. This being said, there is also the chance of missing the launch window due to a minor delay if the delay exceeds any expected time overruns. This would be the worst-case scenario but it has a relatively low likelihood in comparison to other factors because of the estimated storage time for most major missions before launch.

The next logistical risk assessed involved increased operational cost due to multiple probes. This means that there will likely be at least one team for each probe during the mission's lifetime and the people in these teams will need to be paid to keep track of the probes logistics before and after the launch until contact is lost with each of the probes. However, this can be taken into account during the initial cost assessment, thereby reducing the consequences of small overruns in operational costs due to the multiple probes.

Similar to the cost overrun problem, another risk is the availability of enabling technologies such as HEEET TPS. Without HEEET, and with no access to heritage carbon phenolic, probe entry at Saturn may be impossible and entry at Uranus will be very limited in initial entry corridor. Enabling technologies are not only crucial to mission success but, as the name suggests, enable the particular mission concept. If HEEET does not attain a high level of technology readiness before implementation of the design, it could prove very costly to accelerate its development.

The final logistical risk from the list of twelve discussed previously is delays in the development of patch antennas. This is similar to the enabling technologies as discussed previously, but is actually closer to an enhancing technology. The reason for this is because the patch antenna allows for a smaller form-factor for the probe antennas.

Under the current trajectory of the spacecraft, the orbiter will be very far away from the probe at Saturn, requiring the probe to not only communicate through the atmosphere, but also over a long distance. Other antennas are capable of this, but in order to achieve the appropriate form-factor, other trade offs must be made in either power or communication distance.

Technical Risks

The risk assessment for OCEANUS also included technical risks. These involve failures or loss of functionality of a particular component or system during the mission. In the case of this concept study, eight of the top twelve risks are technical risks associated with system failures. In order keep things succinct, four of these technical risks will be discussed here, the first of which is losing the probe before 1 bar atmospheric pressure. This could happen in a few ways, but the most likely occurrence would be due to atmospheric error. This error can manifest risk in multiple ways; most prevalent is in the thermal protection system and initial entry. In the case of the thermal protection system, the peak heat flux or heat load may exceed expected values that were used to size the TPS material. This could cause the thermal protection system to fail before the entry is complete. On the other hand, if the density of the atmosphere is significantly less than expected, there is a possibility of not decelerating sufficiently and skipping out of the atmosphere. Either of these situations would be disastrous for the entry probes, but they do not lead to a total failure for OCEANUS because the orbiter survives both scenarios. The severity of this risk decreases as the probe descends through the atmosphere. For example, if the probe fails at some point between 1 and 10 bar, there would still be a significant amount scientific and engineering data from the rest of the entry and descent.

Another significant technical risk, also involving the probes, is a probe deployment failure. Besides the main consequence of the probe not gathering data in the atmosphere, which is one of the main objectives of the mission, there is also the effect of the mass of the probe still being attached to the orbiter. This becomes very important when determining the required mass for propulsive maneuvers as there is now more mass to move than expected, resulting in a deficiency of propellant for the required maneuvers.

The last technical risk discussed in this section is main engine failure. This means that at some point during the flight, one or both of the main engines fail to fire or stop functioning. Depending on what point in the flight this occurs, the consequences could range from a slight decrease in mission lifetime to total mission failure before the mission achieves any objectives. While the consequences range from benign to critical, the likelihood of failure is relatively low, especially for a case where the failure occurs near the beginning of the mission.

Using this initial assessment and a statistical event risk assessment equation (Eqn. G1), the percentage chance of success was calculated to be 91%.

Table G.1: Top Risks alongside the respective category

No.	Risk Source	Category
1	Cost overruns due to delay	*Cost - Design & Evaluation*
2	Probe lost before 1 bar	*Technical - Entry, Descent & Landing*
3	Probe communication lost before H20 clouds	*Technical - Telecommunications*
4	Probe deployment failure	*Technical - Mechanical Systems*
5	Engine Cover Mechanism Failure	*Technical - Mechanical Systems*
6	Increased operational risk due to multiple probes	*Cost - Mission Design*
7	Availability of HEEET for the probe	*Cost - Entry, Descent & Landing*
8	Probe lost before 10 bars	*Technical - Telecommunications*
9	Parachute failure during final descent	*Technical - Entry, Descent & Landing*
10	Main Engine Failure	*Technical - Propulsion*
11	Patch Antenna development delays	*Cost - Telecommunications*
12	HGA Failure	*Technical - Telecommunications*

Table G.2: Initial risk assessment matrix of top risks, 91% success percentage

Likelihood						
	5	3				
	4			1		
	3		6		2	
	2			7,8	3,5	
	1			4,9	10	11,12
		1	2	3	4	5
		Consequences				

$$*R = \sum_{n=1}^{\infty} (\Pr(e)\Pr(o \mid e)V(e,o)) \quad \text{Statistical Event Risk Assessment} \quad \text{(G1)}$$

Risk Mitigation

In order to decrease the likelihood and consequences of the major risks, mitigation strategies were used in determination of the final mission concept design. For each of the twelve major risks, mitigation strategies to decrease either the likelihood or consequences of each risk were brainstormed. These strategies were listed alongside the respective risk for organizational purposes. Many of these strategies involve extra testing, use of heritage systems with proven success, and increasing development of enabling technologies. With these mitigation strategies included, the mission success percentage increases to 96% using the same statistical event risk assessment as the previous assessment. Using these mitigation strategies, the mission success percentage increased 5% and removed any risks currently "in the red" in terms of risk assessment.

Table G.3: Mitigation strategies for top mission risks

No.	Risk Source	Mitigation Strategy
1	Cost overruns due to delay	Descope updated instruments in favor of heritage instruments when necessary
2	Probe lost before 1 bar	Monte-carlo simulation of different entry conditions & atmospheric conditions

3	Probe communication lost before H20 clouds	Complimentary imaging from orbiter
4	Probe deployment failure	Extensive testing Cassini-Huygens heritage
5	Engine Cover Mechanism Failure	Make cover detachable in the case of retraction failure
6	Increased operational risk due to multiple probes	Pioneer Venus heritage Pre Mission Cost Estimation
7	Availability of HEEET for the probe	Increase funding and continue research and development of HEEET
8	Probe lost before 10 bars	Complimentary imaging from orbiter
9	Parachute failure during final descent	Extensive testing Heritage stowing and deployment
10	Main Engine Failure	Contingency engine
11	Patch Antenna development delays	Increase development efforts into patch antennas
12	HGA Failure	Radiation hardened electronics and thermal testing. MGA as back-up

Table G.4: Post mitigation risk assessment matrix of the top risks, 96% success percentage

Likelihood						
	5	3				
	4					
	3			1		
	2		6	8	2	
	1			4,7, 9,10	5,12	11
		1	2	3	4	5
		Consequences				

Complete Risk Table

Table G.5: OCEANUS detailed risk compilation

Risk Sub-System List	1 = lowest	10 = highest
Attitude Control		
Risk	Severity (1-10)	Likelihood (1-10)
Reaction Wheel - Bearing cage instability	5	3
Reaction Wheel - Motor Failure	5	2
Reaction wheel- lubricant breakdown	5	2
ACS Thruster imbalance - uncontrolled spinning	5	2
Sun sensor Failure	2	4
Star tracker failure	2	4
ACS Thruster imbalance - Catalyst Bed Failure	4	3
ACS Thruster valve fail to open	4	2
ACS Thruster fail to ignite	4	2
ACS Thruster injector erosion -Flow rate unsteady	3	2
Cost & Manufacturing		
Risk	Severity (1-10)	Likelihood (1-10)
Failure to Secure Funds	10	5
Underestimate total cost in early phase	3	7
Cost overruns due to delay	5	7
Budget cut due to space policy change (by new US president)	10	2
SLS launch cost is too high	7	5
Instruments		
Risk	Severity (1-10)	Likelihood (1-10)
Failure of MAG	7	1
Failure of OPI	7	2
Failure of VNIS	6	2
Failure of UVS	3	2
Failure of MIR	3	2
Failure of SPI	4	2
Failure of EPE	4	2
Failure of PWA	3	1
Failure of CDE	3	2
Failure of ASI	7	1
Failure of MS	6	3
Failure of NEP	3	2
Failure of HAD	3	2
Failure of SFR	4	3
Mechanical Systems		

Risk	Severity (1-10)	Likelihood (1-10)
MGA Gimbal Failure	3	3
Probe deployment failure	8	2
Engine Cover Mechanism Failure	7	3
Mission Design and Trajectory		
Risk	Severity (1-10)	Likelihood (1-10)
Missed Thrust at Capture	8	1
Ring Plane Extends Farther than Anticipated	6	1
Power		
Risk	Severity (1-10)	Likelihood (1-10)
eMMRTG thermal stress failure	7	1
eMMRTG reactor burn up	7	1
eMMRTG Ignition Failure	7	1
eMMRTG overheating	4	2
Battery Module - Design flaw	3	1
Battery overheating	3	3
Battery Short Circuit	4	2
Probe EDL		
Risk	Severity (1-10)	Likelihood (1-10)
Availability of HEEET for the probe	5	3
HEEET unable to withstand Uranus and Saturn entry conditions	7	3
Atmospheric uncertainty results in unforeseen trajectory, etc.	3	5
Parachute failure during final descent	6	2
Propulsion		
Risk	Severity (1-10)	Likelihood (1-10)
Discharge Cathode failure - Fail and prevent further ignitions	5	2
Neutralizer Cathode failure - difficulty of ignition	5	2
Orifice (Neutralizer and Discharge Cathode) excessive wear and clogging - flow rate unstable	2	2
Swaged Heater failure - fail to raise the temperature of the impregnated insert to facilitate initial electron emission	2	1
Accelerator Grid failure (structurally fail)- groove penetrates through the accelerator grid resulting in end of life of the thruster	8	1
Accelerator Grid failure (electron back streaming)	4	1
Optic Assembly Electrical Shorting - Caused by debris or spotted material bridging the gap between the grids	1	5

Thermal risk to the permanent Discharge chamber magnets - degrade magnetic strength resulting in thruster performance degradation.	2	2
Excessive temperature, voltage and leakage current on High voltage propellant isolators - increase power loss in thruster system	2	2
Engine cover fails to retract	8	3
Main Engine - Injector erosion, flow rate unstable	5	3
Main Engine - Thruster valve fail to open	5	1
Main Engine - leakage of propellant	3	2
Main Engine fails to ignite	8	2
Science		
Risk	Severity (1-10)	Likelihood (1-10)
Lack of impact or storm events during tour	1	5
Probe descends through unrepresentative portion of atmosphere	2	2
Probe lost before 1 bar	7	5
Probe lost before 10 bars	5	3
Probe lost before H20 clouds	1	9
Lack of satellite flyby opportunities	5	2
Insufficient mission lifetime	4	3
Insufficient context of probe entry sites	4	2
Interesting emissions outside of instrument spectral bands.	4	1
Systems Engineering & Design Risks		
Risk	Severity (1-10)	Likelihood (1-10)
Lack of Funding in Design Phase	7	6
Failure for subsystem design and research to be completed on time	3	7
Increased Operational Risk due to Multiple Probes	4	5
Telecomm & Data Storage		
Risk	Severity (1-10)	Likelihood (1-10)
Atmospheric attenuation is greater than expected.	6	4
MGA failure	3	2
HGA failure	7	1
Patch array technology not ready	9	2
Thermal		
Risk	Severity (1-10)	Likelihood (1-10)
Louvres fail on spacecraft	6	2
Improper reading of temperature within orbiter	5	1
Improper reading of temperature within probe	5	1
MLI degrades sooner than expected	5	1

TPS degrades sooner than expected	5	3
Heat Pipe failure	5	2
Radio-isotope Heating Unit failure	5	2
Optical Solar Reflector over-degradation	4	1
Insulation degradation and breakdown	4	1
Imbalance of spacecraft absorptivity and emissivity	3	1